The Effect of Free stream Turbulence on Separation at Low Reynolds Numbers in a Compressor Cascade

Michael A. Perry Jr.

Thesis submitted to the faculty of the Virginia Polytechnic Institute and State University in partial fulfillment of the requirements for the degree of

Master of Science

In

Mechanical Engineering

Committee:

Dr. Walter O'Brien, Chair
Dr. Clint Dancey
Dr. Al Wicks
Dr. Mark Paul

November 15, 2007

Blacksburg, Virginia

Keywords: Turbulence Grid, Separation, Compressor Cascade, Hotwire Anemometer, Aerodynamic Loss, Boundary Layer Transition, Oil Flow Visualization

The Effect of Free stream Turbulence on Separation at Low Reynolds Numbers in a Compressor Cascade

Michael A. Perry, Jr.

(ABSTRACT)

A parametric study was performed to observe and quantify the effect of varying turbulence intensities on separation and performance in a compressor cascade at low Reynolds numbers. Tests were performed at 25^{o} and 37.5^{o} stagger angle, negative and positive angles of incidence up until the point of full stall, Reynolds numbers from 6×10^{4} to 12.5×10^{4}, and turbulence intensities from approximately 0.7% – 8%. Additionally, oil flow techniques were combined with static tap data to visualize the boundary layer characteristics at various test conditions. The overall performance of the cascade was presented and evaluated through mass-averaged total pressure loss coefficients.

The results of the study showed that the best efficiency (lowest pressure loss coefficient) was determined by separation characteristics for any angle of attack. While adding turbulence generally delayed separation, in some cases, adding turbulence to a separated airfoil resulted in decreased performance. Very similar separation characteristics were observed for the full range of Reynolds numbers and stagger, with the higher stagger setting giving slightly better performance. It was shown that a large percentage of total pressure losses can be recovered by applying the appropriate turbulence intensity at any angle of attack, which is relevant to possibilities for active control of such flows.

Acknowledgements

First and foremost, I would like to thank Dr. O'Brien for his time, patience, knowledge, and also assistance in finding financial support for myself and this research over the past few years. Working with him has been a true privilege. I would also like to thank Dr. Dancey, Dr. Wicks, and Dr. Paul for helping to pull this effort together at the end.

I would like to thank my mother and father for their emotional and financial support over the years. A special thanks must also be given for those who were accommodating in the turmoil that my life transitions to and from academia created. Namely, the guys on Airport Road: Matt Benz, Shaun Cavey, Dave Smith, and of course, Hansel. Also, for the same reason, the gentlemen on DeHart Street: Ben Anderson, Jared Develli, Matt Brubaker, Eric Wiggins, Doug Holt, and Jon Bergen.

Furthermore, I would like to thank fellow graduate students Matt Benz for serving as an example in motivation during the long periods of testing, and Gautham Ramakrishna for designing the turbulence grids. Thanks to Joel, JJ, Brandon, and Cameron of Woody's for helping to provide distractions when the going got rough.

Finally, I would like to thank Richard Dean Anderson ("MacGyver") for inspiring a generation of engineers, of which I am one.

Table of Contents

List of Figures

List of Tables

Notation

u – Stream-wise velocity component of flow

u' - Root-mean-square velocity component

u_i – Instantaneous velocity

u_{mean} – Time-averaged velocity

Tu - Turbulence intensity

x_{turb} - distance downstream

C – rod layout geometry coefficient

c – Chord of compressor blade

d - rod diameter

ν – kinematic viscosity

Re - Chord based Reynolds number

Λ_x - Integral length scale

T - Integral time scale

R_{11} - Autocorrelation

$\Delta\tau$ - Time Step

$E(f)$ - Turbulent energy at specific frequency

κ – Wavenumber

κ_e – Most energetic wavenumber

ν – kinetic viscosity

M - Mesh distance

N – Number of samples

f_s - Sampling frequency

Δf - Frequency resolution

$X(f)$ - FFT of signal at specific frequency

ξ - Stagger angle

i – Angle of incidence

α^* - Angle of attack

α_1' – Inlet blade metal angle

α_2' - Exit blade metal angle

α_1 – Inlet flow angle

α_2- Exit flow angle

δ – Deviation angle

ε – Deviation or turning angle

s – Blade spacing

$\overline{\omega_2}$ – Mass averaged total pressure loss coefficient

$C_{p\ yaw}$ – Dimensionless yaw pressure coefficient

$C_{p\ total}$ – Dimensionless total pressure coefficient

$C_{p\ static}$ - Dimensionless static pressure coefficient

$C_{p\ s,blade}$ - Dimensionless static pressure coefficient, blade surface

Chapter 1

Introduction

In the defense industry recently there has been a steep increase in development of unmanned vehicles, leading to expanding needs to produce smaller gas turbines for power generation and propulsion for unmanned aircraft. As the chord size of compressor blades shrink or at high altitudes, these applications begin to fall into the low Reynolds number regime. Under laminar flow or at operation away from the design point, boundary layer separation leading to stall conditions is a distinct possibility. While active flow control continues to develop, it is advantageous to investigate fundamental and more passive means for preventing or delaying the onset of separation, such as through energizing the boundary layer with increased free stream turbulence.

In the 1970's through the 1990's the Turbomachinery Group of the Virginia Tech Mechanical Engineering Department conducted various low Reynolds numbers cascade tests to investigate compressor phenomenon such as separation, reversed flow, rotating stall, and the effect of varying flow parameters on cascade performance. As an extension of that research and with the rebirth of low Reynolds number interest, this work currently aims to investigate the effect of free stream turbulence on separation at different settings of angle of attack, stagger, and Reynolds number.

1.1 Background and Previous Research

The current research drew from many aspects and practices of aerodynamic testing that have been continuously developed as the gas turbine industry has moved forward. As a parametric study, it uses previous investigations, and will add to the wealth of research already performed.

It is important to review the evolution of such research up to this point, to link past and present developments before building upon them.

1.1.1 Cascade Testing

Linear cascades have been historically important in the testing of axial flow compressors. Parameters can be varied independently of each other to yield performance and efficiency data, or give qualitative clues about conditions for separation, all while testing on a stationary setup. It was through this type of testing that correlations were developed that formed the basis for many current day design procedures [17] as well as the wealth of airfoil data produced and recorded by the NACA. In all of the works presented in the current background investigation cascade testing was the method of data collection. Most currently, cascade results provide reliable data to validate the predictions of Computational Fluid Dynamics (CFD) code.

1.1.2 Effect of Reynolds Number on Flow Separation

Rhoden [19] made an investigation into the effect of Reynolds number on separation at different angles of camber and stagger in a linear cascade in 1952, using the same type of total pressure traverse and static tap measurements used in this study. His study found that there are optimum and critical Reynolds numbers corresponding to camber angles, the critical Reynolds number being the value under which cascade performance is severely affected because of boundary layer separation.

Roberts [20] investigated the diminishing performance of a cascade with increasing laminar separation bubble growth in order to calculate bubble size and predict the cascade performance at low Reynolds number. Up until his 1975 investigation, the correlations used to predict cascade performance did not take into account the effects of low Reynolds numbers, being based on experiments well above their respective critical Reynolds numbers. From his investigation, which included chord based Reynolds numbers from 250,000 down to 40,000, Roberts proposed a modified semi-empirical theory for the growth and bursting of laminar separation bubbles, as well an empirical correlation for axial compressor cascade performance after bursting. These

combined to give calculations of performance over the entire Reynolds number range, from natural transition to complete separation [20].

Stalled, reversed, and unsteady flows in a compressor cascade were investigated experimentally by Yocum as part of Virginia Tech's low Reynolds number research program in 1988. Part of his effort was to match the experimental results with numerical code, which has become more commonplace as CFD has continued to develop. Yocum's experiments covered a vast range of angle of attack at three different settings of stagger in an effort to measure the effect on performance at a Reynolds number of 2×10^5 [2]. Separation was well documented in these tests as the range of angle of attack went from negative incidence angles into full stall. In general, his research is also a good example of a highly parametric cascade flow investigation.

1.1.3 Turbulence

Turbulence has been studied in detail for over a hundred years, beginning with formal definition and investigation, through theoretical derivation and predictions and continuing with empirical experiments, all the way to today's CFD simulations in an effort to fully and accurately quantify its behavior and effect on flows. Early pioneers in the field include Osborne Reynolds, Taylor, Von Kármán, and Kolmogorov, to name a few. These pioneers laid out the governing equations and fundamentals of turbulent flow behavior, ultimately resulting in further understanding and useful application of turbulence in the recent past.

Fundamental experimental investigations of turbulence have been numerous. In areas related to grid generated isotropic turbulence there have been many empirical studies attempting to confirm or refine theoretical models. Most of these models are laid out in the seminal textbook *Turbulence* by Hinze [4], which describes attempts to confirm the Von Kármán relation and Kolmogorov's Spectrum Law for isotropic turbulence, as well as other empirical studies of grid generated turbulence [4]. The influence of low Reynolds numbers on turbulence isotropy has also been studied in detail; inconsistencies with the $-5/3$ slope of the Kolmogorov Spectrum Law

have been observed by Von Kármán, Sato, Gamard and George, and Biroak et al. more recently [7][8][9][10].

While most papers examined the characteristics of grid generated turbulence, Roach published the first comprehensive guidelines for designing grids based on measurement distances and desired turbulence intensities, and providing formulas to predict the corresponding length scale. It was with this methodology that the turbulence generating grids used in this study were designed [3].

1.1.4 Effect of Turbulence on Separation

Early tests introducing turbulence to cascade testing in combination with varying Reynolds numbers, and its application to increasing performance were done by Shaw and Citavy et al. [22][23]. Shaw's work was a fairly broad investigation that included the effect of inlet guide vanes in front of the cascade and comparison with a rotating row, and showed that turbulence intensity and Reynolds numbers both had a strong influence on performance. The work of Citavy et al. was more focused on the conditions around separation and the behavior of the separation bubble at a particular setting of incidence and stagger, and with an eye towards separation hysteresis with Reynolds number [23].

In other early investigations into the effect of turbulence on losses in a cascade, Evans [21] conducted a study at a single Reynolds number of 5×10^5 and constant camber angle of 4º, varying only the free stream turbulence. He concluded that increasing free stream turbulence caused a slight increase, and then a decrease in total pressure loss coefficient, due to turbulence contributing to the thickness of the boundary layer and then delaying the separation, respectively.

The free stream turbulence effects on blade wakes in compressor cascades were analyzed by Sullerey et al. in 1983, at a Reynolds number of 1.31×10^5, three angles of incidence, and three settings of turbulence level [24]. The finding was that although there is a faster wake decay (quicker mixing) with increasing free stream turbulence intensity, there is also a generally larger

wake produced by the higher turbulence intensity. In this study, there was no investigation into the boundary layer conditions at different angles of attack.

In 2000 Schreiber et al. [25] examined the effect of Reynolds number and free stream turbulence on boundary layer transition in a compressor cascade of controlled diffusion airfoils (CDA), using flow visualization to document separation and re-attachment under varying conditions. Also, this technique was used to observe how changes in turbulence level and Reynolds number moved the point of transition at constant incidence. Schreiber's research was a visual investigation, with no data gathered to quantify performance.

Douglas performed an investigation into the effects of free stream turbulence on compressor cascade performance in 2001, with low levels of turbulence and transonic Mach numbers [15]. This research included both performance calculations based on total pressure loss and oil flow visualization to observe the suppression of the laminar separation bubble. While varying the angle of incidence, Douglas found that reductions in loss coefficient due to increased free stream turbulence at the lowest loss cascade angle were 56%, but decreased as the inlet Mach number approached choked flow.

1.2 Summary

There have been many improvements and advances up to the present time in compressor cascade flow research. One of the least explored areas to date is that of the low Reynolds Number regime, which is the focus of this research. Some of the previously mentioned investigations have focused on separation at low Reynolds numbers, and some have even observed the effect of turbulence on separation at low Reynolds numbers. Still, there has not been a parametric study at low Reynolds numbers to investigate and quantify the changing performance due to the effect of turbulence on separation at different angles of attack and stagger. With developments and interest in active control, it is advantageous to investigate these parameters as a roadmap and database for the future.

Chapter 2

Fundamental Cascade Aerodynamics

A linear compressor cascade was used to test the axial flow compressor airfoils in this research, under the assumption of steady, incompressible, two-dimensional flow [26]. This chapter familiarizes the reader with the cascade geometry and its notation, and the theory and equations used to obtain performance parameters.

2.1 Cascade Geometry

The cascade geometry used in this study is typical of compressor cascade test setups, and is shown in Figure 2.1. The chord, *c*, is defined as the straight distance from the leading to trailing edge, while the camber line bisects the pressure and suction side of the airfoil from leading to trailing edge. The path of incoming flow with respect to the tangent to the camber line at the leading edge of the airfoil is the angle of incidence, *i*, and the angle formed between the exit flow and tangent to the camber line at the airfoil trailing edge is the deviation angle δ.

The blade metal angles, α'_1 and α'_2, are the angles between the camber line and the axial plane, and the angle of attack, $\alpha_1{}^*$, lies between the flow and the flat bottom of the airfoil.

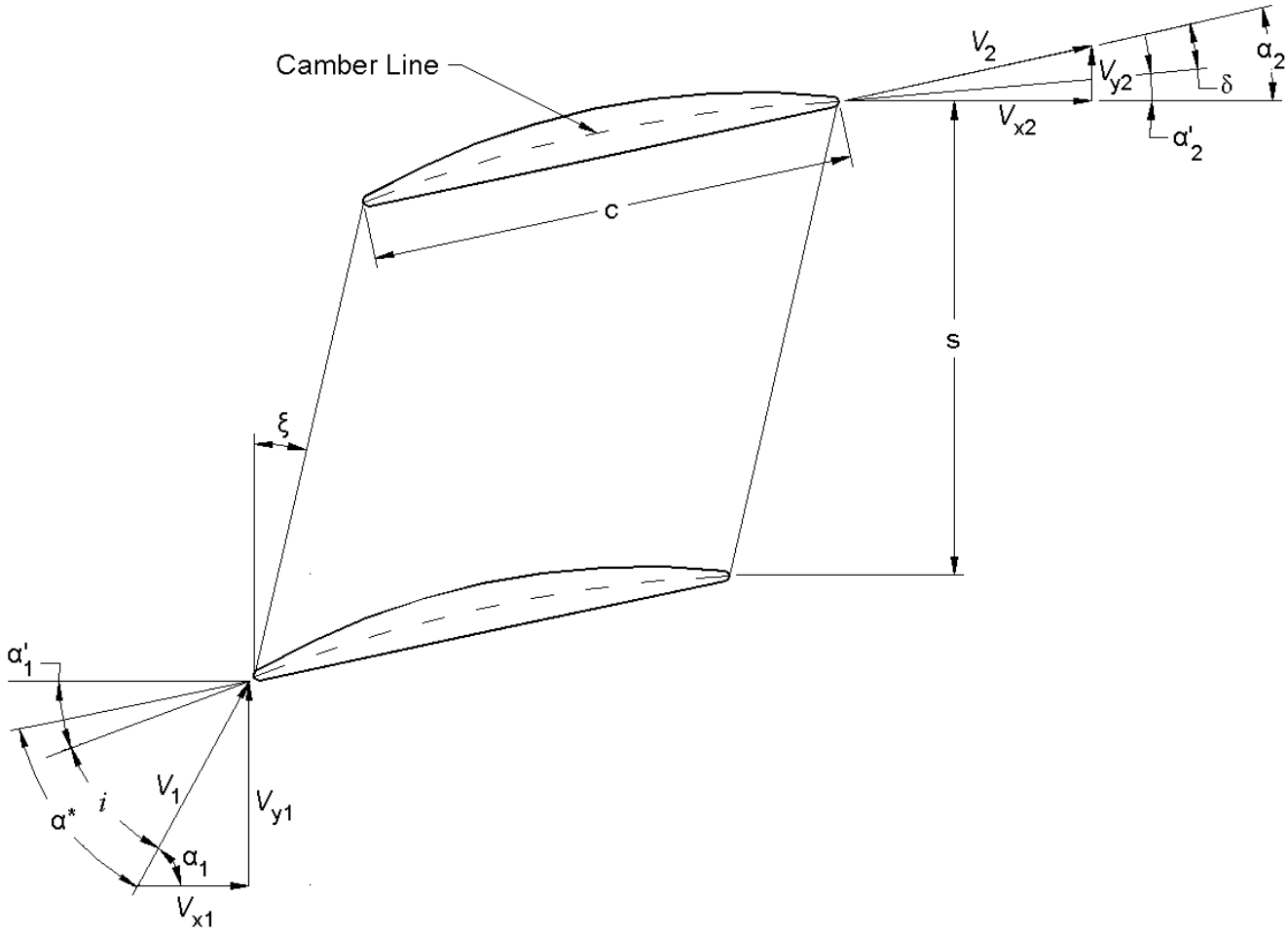

Figure 2.1 The flow vectors and geometric descriptions of the cascade.

The incoming and exit velocities can be broken down into their axial components (x) and their tangential parts (y) to form typical turbomachinery velocity triangles such as in Figure 2.1. The cascade is further defined by the two parameters of stagger, ξ, and blade spacing s, which with chord c form the ratio of solidity (c/s). For this research, the solidity was unity.

2.2 Cascade Theory

There are several ways to quantify the performance of a linear cascade. Often, a total pressure loss coefficient is paired with a flow and force relationship such as a blade force coefficient or moment coefficient. In this research the total pressure coefficient was the sole characteristic of

performance. Two typical definitions of the total pressure loss coefficient also exist, including that using an area averaged approach, and that using a mass averaged approach.

The mass-averaged total pressure loss coefficient is defined as

$$\overline{\omega_2} = \frac{\int_0^s C_{p\,total}(s)(\rho u_2)dy}{\int_0^s \rho u_2 dy} \tag{2.1}$$

where $C_{p\,total}$ is the dimensionless total pressure coefficient defined by

$$C_{p\,total}(s) = \frac{P_{t_1} - P_{t_2}}{P_{t_1} - P_{s_1}} \tag{2.2}$$

and since the flow is assumed incompressible,

$$\overline{\omega_2} = \frac{\int_0^s C_{p\,total}(s)(u_2)dy}{\int_0^s u_2 dy} \tag{2.3}$$

[14]. The-area averaged total pressure loss coefficient is essentially equation 2.1 with no dependence on velocity, and leads to the assumption that the total pressure loss in the slower wakes makes the same contribution to the percentage-wise total loss as do the losses at higher velocities in the passages. Since mass-averaged loss coefficient was used more frequently in previous investigations, it was also used in this investigation.

The static pressure coefficient, calculated from measurements from the blade surface static taps, is defined in a similar manner as the total pressure coefficient, by

$$C_{p\,s,blade} = \frac{P_{s_1} - P_{s_b}}{P_{t_1} - P_{s_1}} \tag{2.4}$$

A frequent concern of cascade testing is the two dimensionality of the flow. If the sidewalls are solid, the boundary layers forming on their surfaces and the associated corner stall will slow the flow locally and cause acceleration in the middle of the test cross section. Thus, the flow blockage will result in a measured downstream velocity slightly higher than the upstream. The

magnitude of this effect, and the departure from two dimensionality is measured by the Axial Velocity Ratio (AVR) defined as

$$AVR = \frac{V_{x_2}}{V_{x_1}} = \frac{\int_0^s u_2 dy}{\int_0^s u_1 dy} \tag{2.5}$$

[2].

Chapter 3

Experimental Setup

The equipment used to run the tests and collect data is described in this chapter. It also covers the calibration of the instruments used to measure turbulence and pressure. Finally, a section on turbulence is presented including grid design, turbulence analysis, and performance.

3.1 Wind Tunnel

The entirety of this research was performed at the Mechanical Engineering Turbomachinery Lab at the Virginia Tech Montgomery Executive Airport, in an instrumented, open wind tunnel, shown in Figure 3.1. The flow to the tunnel was provided by a centrifugal fan with a 15 horsepower electric motor. Guide vanes covered the inlet of the fan to provide a course adjustment of the flow, and a fixture was designed and added between the fan and the tunnel to bleed flow as a fine adjustment. With this new attachment the flow could be reduced reliably to a Reynolds number of around 10,000, and still maintain the capability for the highest Reynolds number of up to 200,000 with no pressure drop due to turbulence generation.

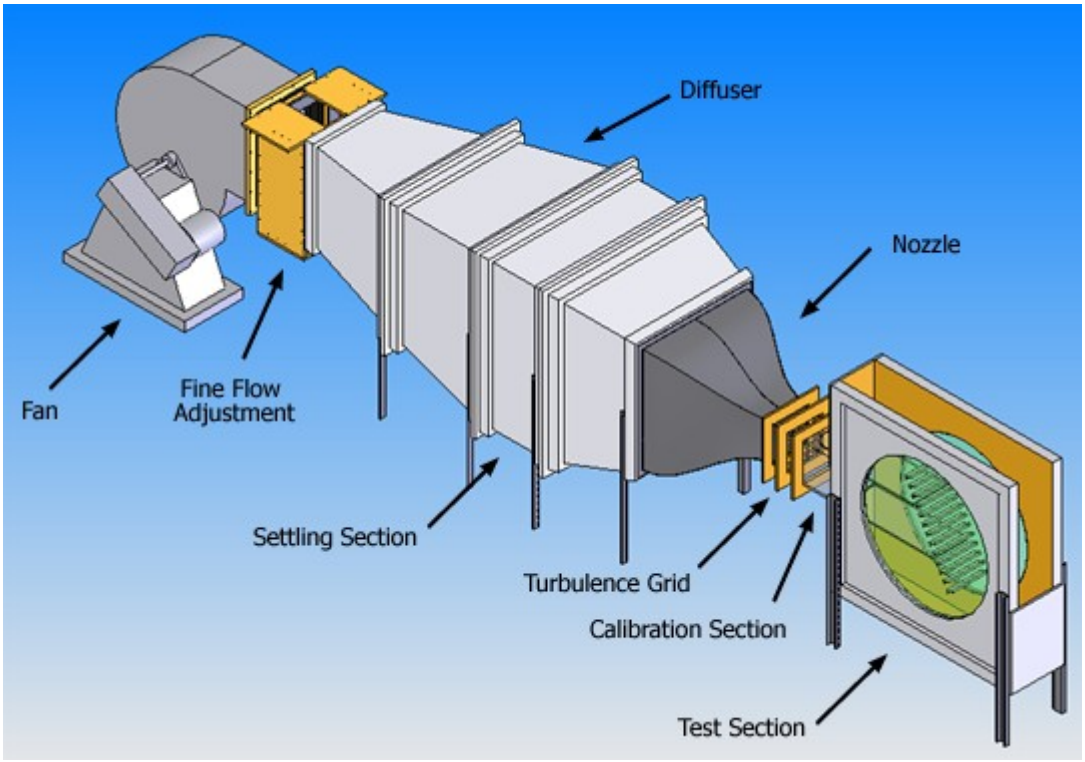

Figure 3.1 Layout of the wind tunnel and test section used in this research.

There are three main parts to the wind tunnel. The first is the diffuser, which is equipped with screens and honeycomb to reduce the free stream turbulence and provide more uniform flow [2]. The settling section is located between the diffuser and nozzle, and has a 48" square cross section. The secondary part of the nozzle is made of sheet metal and provides a 16:1 contraction ratio down to the 12" square cross section where the grids are located [2].

One wooden flange is mounted to the nozzle and another to the calibration section. The different turbulence grids were bolted in between the two flanges to provide a tight a seal. To accommodate changing grids, the test section was made mobile. The calibration section was located between the nozzle and the test section, and had a 12" square cross section as well. This is where the 3-hole probe was calibrated and the Reynolds number measured before each run.

The test section consists of two large (4.5') Plexiglas circles which, when bolted to the blades that separate them, makes one solid rotating row of blades. Head boards were placed after the calibration section to maintain the 12" square test cross section up to the blades. After the blades, the tailboards were placed (at the same angle as the angle of attack of the blades) to continue this cross section out to the open atmosphere. As the sides of the test section were formed by the Plexiglas circles, there was no way to remove the boundary layer from the sidewalls in this test setup, which will be discussed in a later section.

Rotating the blade row to any angle of attack changes the distance between the calibration section and the top (or bottom) blade exposed to the test cross section, requiring the use of headboards of adjustable length, as well as sheet metal extensions to cover any gaps. To make sure there was no exchange between the air inside the post-tunnel flow and the atmosphere, the headboards were equipped with rubber gaskets on the sides, and metal extensions were carefully taped inside the tunnel to preserve the seal. The measurement slot locations up and downstream of the cascade centerline for the probe traverses are shown in Figure 3.1A.

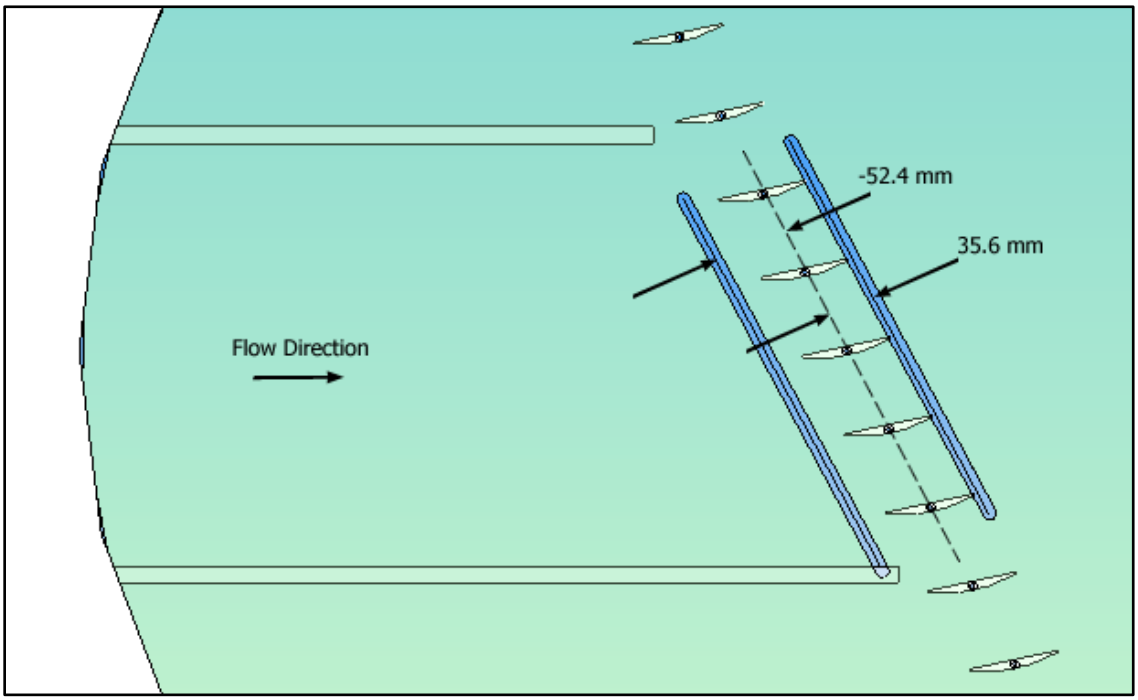

Figure 3.1A The probe traverse locations with respect to the cascade.

3.2 Blades

For testing, the desired stagger was achieved by rotating the blades about the bolts which passed through their centers. After securing the blades at the stagger angle, the angle of attack was achieved by rotating the solid assembly of blades and Plexiglas circles about its center in the plywood test section housing. The geometry of the blades is shows in Figure 3.2.

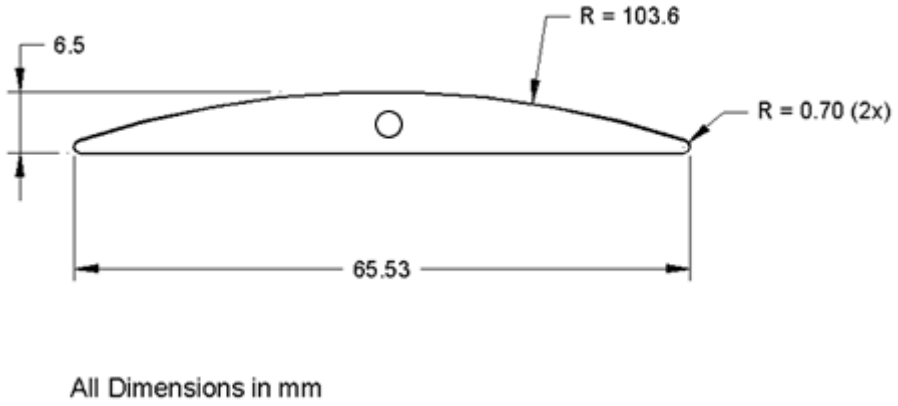

Figure 3.2 The geometric description of the flat bottom airfoil used for testing.

The span of the blades is just shorter than the 12" span of the test cross section to facilitate their removal. Before testing, spacers with the same cross section as the blades were used to fill the resulting gaps. The space, *s*, between the blades was equal to the chord length of 65.53 mm, resulting in a solidity of 1.00. The span of 12" (308 mm) to chord length ratio gave an aspect ratio of 4.70. Based on the geometry, the angle of incidence at zero angle of attack is very close to 8°.

3.3 Static Pressure Taps

The two center blades in the cascade were modified to take static pressure measurements at increments along their chords. Figure 3.3 shows the fractions of chord length that the static taps (0.020 in. dia.) were located. According to boundary layer theory, the static pressure due to the airflow above the blade surface is impressed upon the surface itself, which we can read with the

static taps [27]. Thus, we can get a good idea of whether or not the airflow above a point on the surface is separated based on the static pressure at that point.

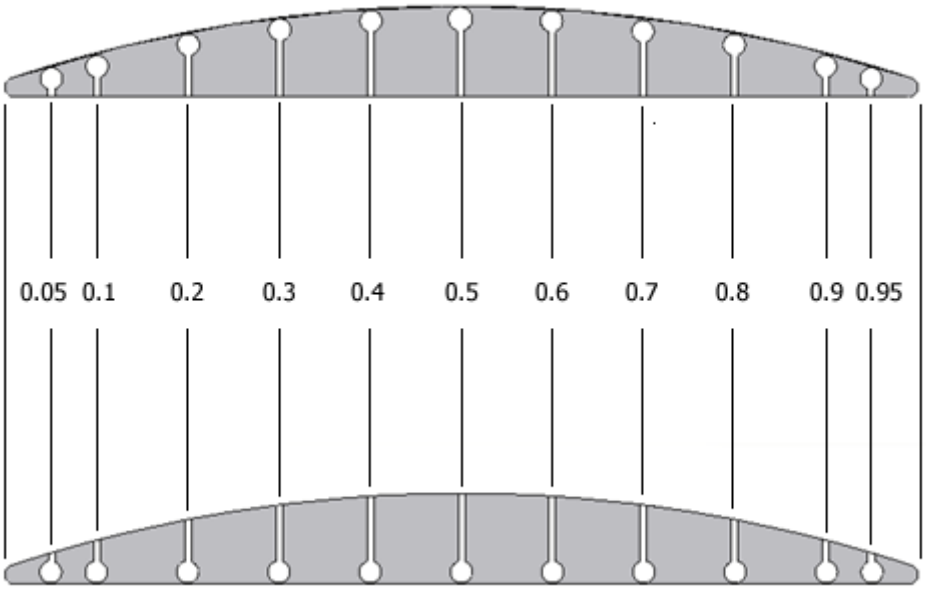

Figure 3.3 Static pressure tap locations by fraction of chord.

3.4 Pressure Probe

A cylindrical 3-hole pneumatic probe was used to take measurements both upstream and downstream of the flow. This requires the assumption that the flow in these areas is purely two dimensional, as discussed in the axial velocity ratio section later in this thesis. The three flow properties that can be directly measured or derived from this type of probe, shown in Figure 3.4, are the total pressure, static pressure, and flow angle. Also, there are two modes in which this probe was used, the nulling and non-nulling modes.

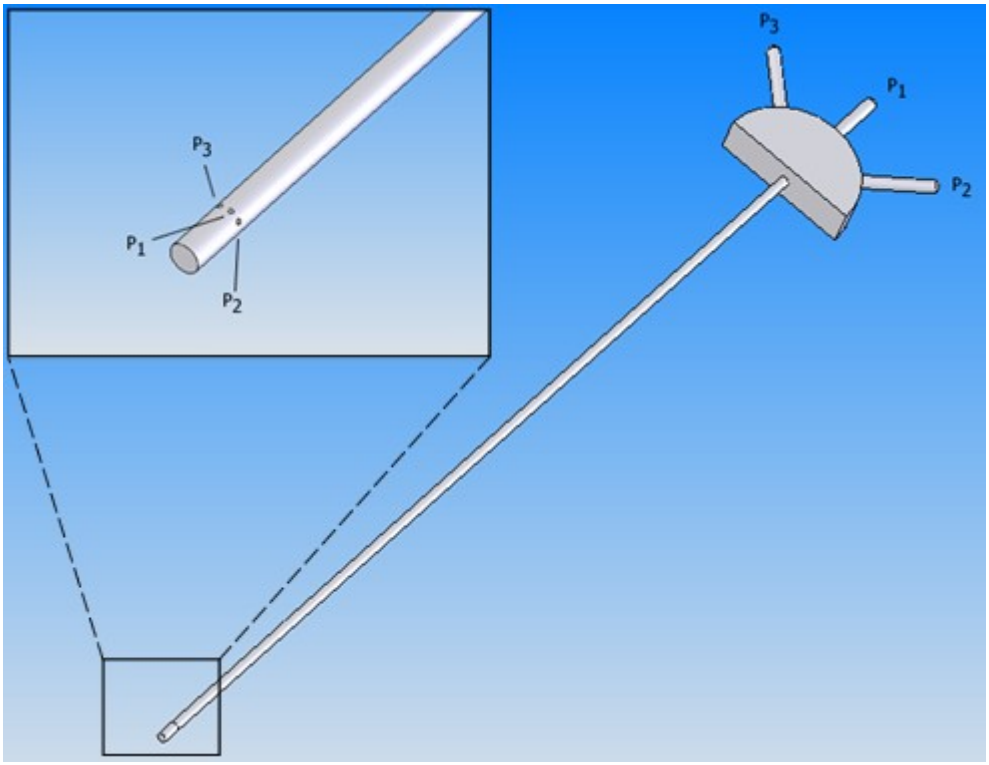

Figure 3.4 3-hole probe geometry.

The nulling mode is where the probe is placed in the flow and nulled so that the pressure readings from ports p_2 and p_3 are equal. Under the assumption that these ports are geometrically equidistant from the center port p_1, then p_1 should read the total pressure. If the probe has been attached to a properly calibrated potentiometer, then the angle of the probe with respect to the horizontal (the flow angle) can be easily calculated. Although equal, the readings from ports p_2 and p_3 at this point will not read the true static pressure, and the probe must be calibrated so that the local static pressure can be derived. The downstream pressure and angle measurements were made using this nulling method.

The probe used in the non-nulling mode is fixed with respect to the flow. The values of total and static pressures and flow angle are all calculated using the probe's calibration curves. While a drawback of this method is that it can only be used accurately for smaller inlet angles, the advantage is that it does not require the time to null the probe at each location, and measurements

can be taken quickly. For the upstream measurements the inlet angles were sufficiently small to utilize this non-nulling method.

3.4.1 Pressure Probe Calibration

The calibration of a 3-hole probe is done by recording the three pressures in a known flow as a function of probe yaw angle, and then checking for dependence on Reynolds number. The approach used by Yocum [2] in similar research was to view the 3-hole probe as essentially a 5-hole probe that does not use pitch pressure ports, and to use the similar calibration technique of the 5-hole probe.

The goal is to determine the relationships, normally expressed as dimensionless pressure coefficients and a function of yaw angle, between the three pressure ports and the true total and static pressures [11]. These pressure coefficients are defined as:

$$C_{p\,yaw} = \frac{p_3 - p_2}{p_1 - p_{s\,ind}} \tag{3.1}$$

$$C_{p\,total} = \frac{p_1 - p_{t\,true}}{p_1 - p_{s\,ind}} \tag{3.2}$$

$$C_{p\,static} = \frac{p_{s\,ind} - p_{s\,true}}{p_1 - p_{s\,ind}} \tag{3.3}$$

where $p_{s\,ind} = \frac{p_2+p_3}{2}$ [11] [2]. After collecting data to generate C_p curves at different flow angles, values can be interpolated from these curves to solve the previous three equations for $p_{s\,true}$ and $p_{t\,true}$. Data were collected for the three different setting of Reynolds numbers, and the resulting C_p curves are shown in Figures 3.4.1A, 3.4.1B, and 3.4.1C.

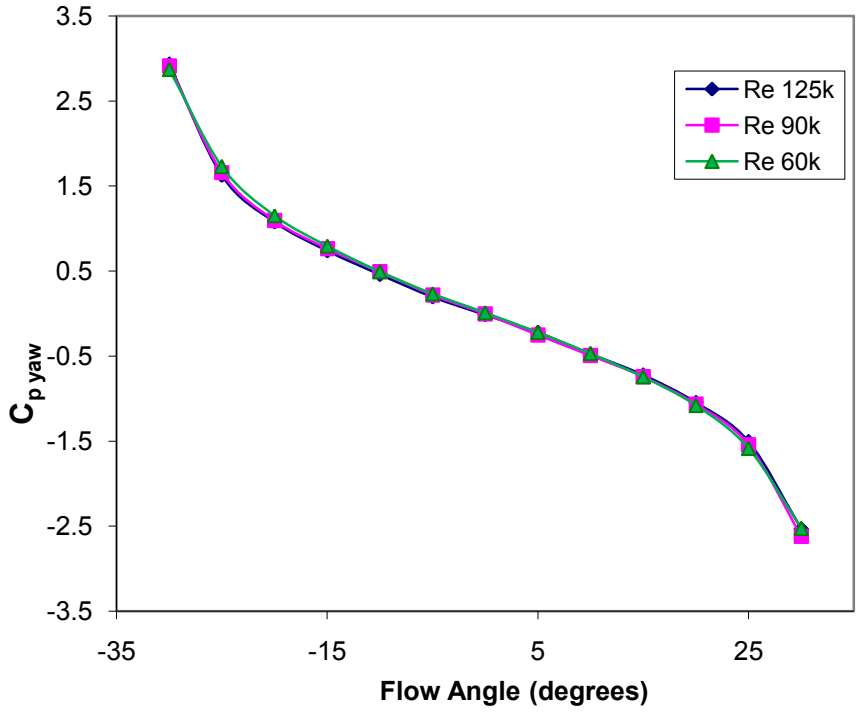

Figure 3.4.1A The $C_{p\ yaw}$ calibration curve for all three Reynolds numbers.

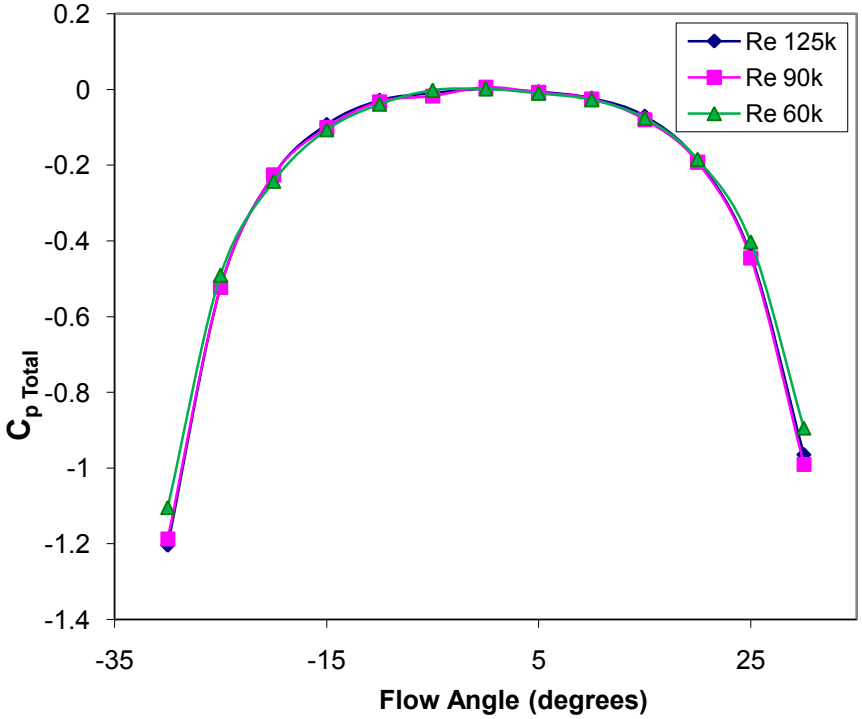

Figure 3.4.1B The $C_{p\ total}$ calibration curve for all three Reynolds numbers.

To back out the total and static pressures at a point, the three known values for the port pressures of the 3-hole probe are used in equation 3.1 to yield a value of $C_{p\,yaw}$. From the proper $C_{p\,yaw}$ calibration curve, the flow angle can be found and translated onto the other two calibration curves ($C_{p\,yaw}$ and $C_{p\,yaw}$) to find their respective values [11]. Everything is then known to solve equations 3.2 and 3.3 for the total and static pressures.

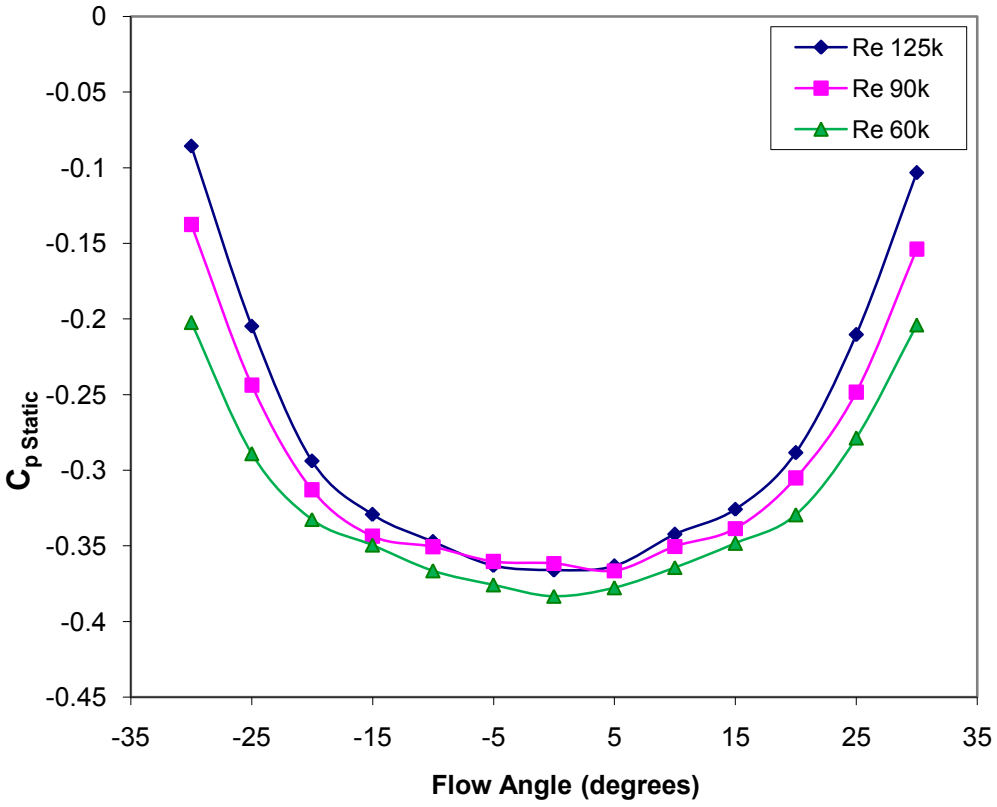

Figure 3.4.1C The $C_{p\,static}$ calibration curve for all three Reynolds numbers.

Notice that the calibration curves show very little dependence on Reynolds number, except those of the static pressure coefficient. If using one calibration for all Reynolds numbers tested, the expected error of measured static pressure would be around or less than 5%, but best accuracy is obtained by using calibration curves obtained at the different Reynolds numbers tested [11]. This was the approach used in this research.

3.5 Pressure Measurements

Pneumatic measurements were key to this research both in quantifying performance and providing flow and separation visualization from static tap data. The accuracy of these measurements was of paramount importance, so the most accurate transducers available in the project budget were purchased along with an extremely accurate means of calibration.

3.5.1 Calibration Point Detector

A Dwyer Model 1430 Microtector Electronic Point Detector was purchased to calibrate the Serta pressure transducers. This instrument has an accuracy of ±0.00025" H_20 over a range from 0 to 2" H_20, and came certified as traceable to a master at NIST. This microtector basically works as a manometer with a small current passing through it, with one of the legs containing a probe attached to a micrometer that is lowered until it touches the water level and completes a circuit. The pressure is then read off the micrometer.

3.5.2 Pressure Transducers

All pressure measurements reported in this research were measured with Setra Model 264 Very Low Differential Pressure Transducers. The three ranges used were 2.5" H_20, 0.5" H_20, and 0.1" H_20, with calibration certified accuracies of ±0.25% of full scale (FS). The effect of this is calculated in the error analysis of Appendix A.1. These transducers were repeatedly calibrated against the microtector during testing and were determined to fall within the manufacturer-certified errors during the entire range of tests.

3.6 Hotwire Anemometer

Upstream measurements were conducted with hotwire anemometry to obtain accurate levels of turbulence intensity for each test. A TSI IFA 100 Intelligent Flow Analyzer was used according to the instruction manual along with a TSI model 1201 anemometer to produce a stable output with good frequency response. Several different anemometers were used, each with a different

operating resistance. Because of changing testing temperatures, the hotwire system was calibrated before running each test.

3.6.1 Hotwire Calibration

Since the hotwire sensor measures the rate of heat transfer from the wire to the air, a calibration needs to be performed relating the recorded bridge voltage to the velocity of the airflow. Thus, a routine was created wherein the velocity was varied from zero up to the maximum Reynolds number setting. The velocities were measured by a Pitot tube and pressure transducers, and plotted against the average measured voltage from the hotwire. This plot has been shown in previous literature to follow a fourth-order polynomial fit, as shown in Figure 3.6.1 [12].

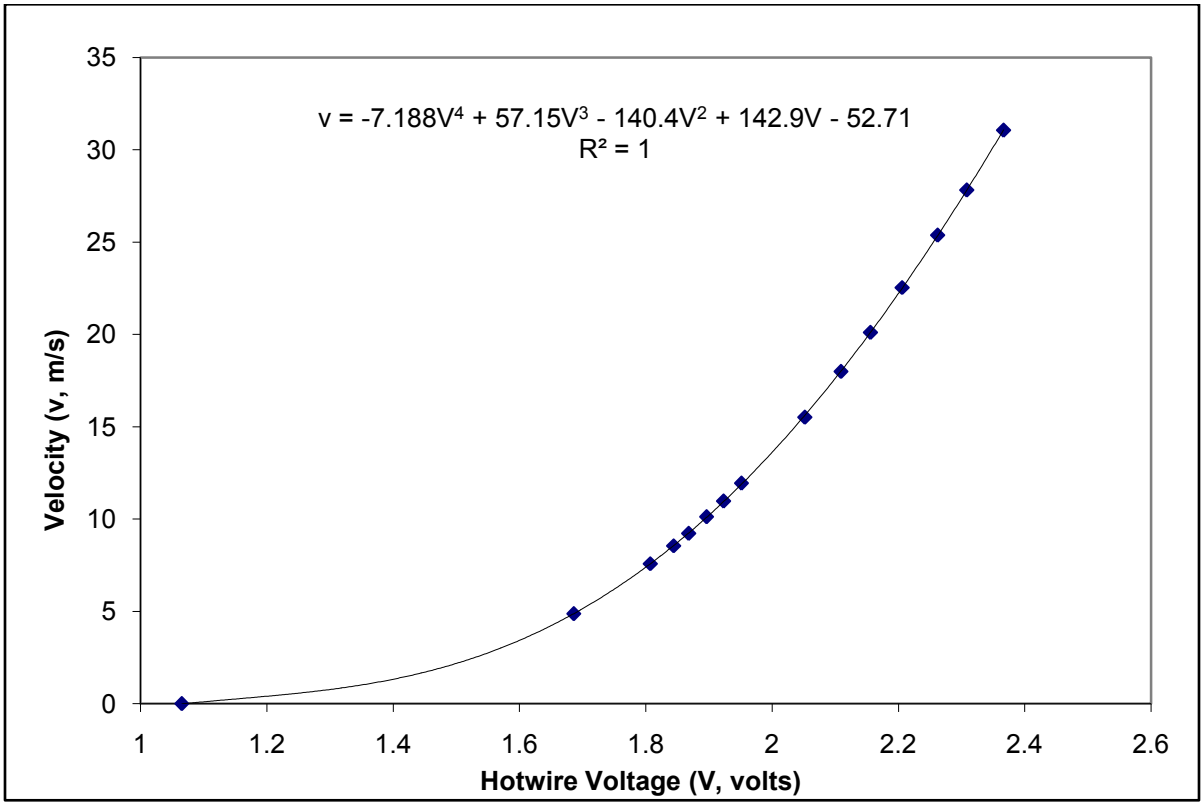

Figure 3.6.1 Typical hotwire calibration curve obtained in every test case.

3.7 Data Acquisition

All electronics were wired to a terminal block for data acquisition through a National Instruments DAQCard-6062E PCMCIA card. All inputs used were analog, with a 12 bit resolution and 500 kS/s sampling rate. The analog inputs, according to the National Instruments specification sheet, have an absolute accuracy of ± 17.945 mV, which was factored into the error analysis in Appendix A.1.

3.8 Turbulence

"…We have spoken about turbulent motion, which can be assumed to consist of the superposition of eddies of various sizes and vorticities with distinguishable upper and lower limits. The upper size limit of the eddies is determined mainly by the size of the apparatus, whereas the lower limit is determined by viscosity effects and decreases with increasing velocity of the average flow, other conditions remaining the same. Within these smallest eddies the flow is of a strong viscous nature, where molecular effects are dominant." -Hinze

It makes sense from Hinze's definition of turbulence that the physical sizes and intensities of the eddies composing the turbulence should be known in order to fully describe them. The physical size of the eddies are defined by one of several length scales, while the intensity of the turbulence can be calculated from the mean and fluctuating components of the stream-wise flow velocity. In this investigation the eddy integral length scale (Λ_x) will be used instead of either the dissipation- or micro-scales, as it is readily determined and used frequently in related literature.

3.8.1 Turbulence Generation

Turbulence was generated through the use of grids, as grids produce nearly isotropic turbulence and are easy to manufacture. Two different types of grid layout were used: square-mesh arrays of round rods (SMR), and parallel arrays of round rods (PR). The mesh geometries were

designed by fellow graduate student Gautham Ramakrishna using the design methodology detailed by Roach [3].

While efforts can be made to design a grid system for desired levels of turbulence, there are still elements of variability that are hard to control, such as background turbulence levels, grid surface roughness, and boundary layer contributions to name a few [3]. So while turbulence levels can be the aim of design, empirical test data is ultimately needed to quantify the actual results.

3.8.1.1 Grid Design

The original intent of the grid design was to make four grids producing increments of 2% turbulence intensity up to 8%, using readily available bar stock for construction. With known rod diameters d, desired turbulence intensities Tu, and geometry layout C, the equation

$$Tu = C\left(\frac{x_{turb}}{d}\right)^{-\frac{5}{7}} \tag{3.4}$$

yields the distance downstream, x_{turb}, necessary to produce the desired turbulence [3]. The value of the coefficient C set forth by Roach was 0.80 for both grid types (PR and SMR) used in this research, and was suggested to be possibly dependent on Reynolds number. The design details for the grids are shown in Table 3.8.1.1, noting that FS is representative of the background turbulence found in the tunnel without any grid. The grids are shown visually in Figure 3.8.1.1, with a summary of their performance outlined in a following subchapter.

Table 3.8.1.1 Grid design summary.

Grid #	Rod Ø (in)	Spacing M (in)	Type
FS	-	-	-
A	0.1875	1.25	SMR
B	0.5	2.5	SMR
C	1	3.5	SMR
D	1.5	3.5	PR

Although this optimal distance downstream was determined, the calibration section was added between the grids and the test location after the grids were already manufactured, increasing the distance and dropping the value of turbulence below the desired value for each grid. The main goal of the research was to evaluate separation, reattachment, and performance at different turbulence intensities, not necessarily integer values, so the more arbitrary turbulence intensities were judged to be satisfactory for use, as redesign would have required non-standard bar stock and valuable time to produce.

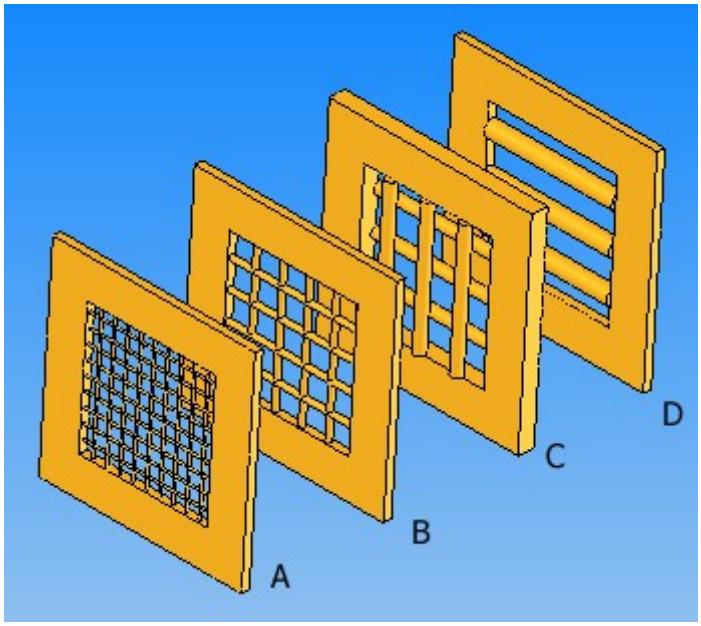

Figure 3.8.1.1 Different grid geometries used for turbulence generation.

3.8.2 Turbulence Intensity

The intensity of the velocity fluctuations used to find the turbulence is found from the root mean squared method defined by

$$u' = \sqrt{(\overline{u^2})} = \sqrt{\frac{1}{n}\sum_{i=1}^{n}(u_i - u_{mean})^2} \tag{3.5}$$

The turbulence level is then

$$Tu = 100 \cdot \frac{u'}{u_{mean}} \tag{3.6}$$

and reported as a percentage.

3.8.3 Turbulence Length Scale

The integral length scale corresponds to the maximum eddy size (or maximum distance between velocities that can be correlated in a flow) for which it and all smaller eddies contain the total distinguishable turbulent energy in a turbulent flow. With respect to grid generated turbulence, although length scales are independent of grid type and velocity, they scale with rod/bar dimensions and increase with distance behind the grid [3][9]. Also, though turbulences with larger integral length scales have been shown to cause earlier onset of transition [29] and provide more favorable heat transfer when the eddies are large enough to penetrate the post-transition boundary layer [6], there is little information on the effect of integral length scale on separation. Finding the integral length scale for a given data set is a multistep process, outlined in this section.

By taking the autocorrelation of the fluctuating part of the velocity from a data set and normalizing it to a value of one at zero lag, a single curve can be generated that is related to the virtually identical time and spatial correlations [4][5][6]. Referring to Figure 3.8.3, the area under the curve can be numerically integrated until the curve hits zero, because at this point useful data is indistinguishable from noise. Ideally the integration would be the infinite sum of area under the curve, but the integrity of this data is uncertain. This integration results in an integral time scale, *T*, such that

$$T = \int_{t=0}^{\infty} R_{11}(\tau) d\tau \cong \sum_{i=1}^{N_o} R_{11} \cdot \Delta\tau \tag{3.7}$$

where R_{11} corresponds to the autocorrelation curve, $\Delta\tau$ is the time step, and N_o is the sample at which the autocorrelation curve crosses zero.

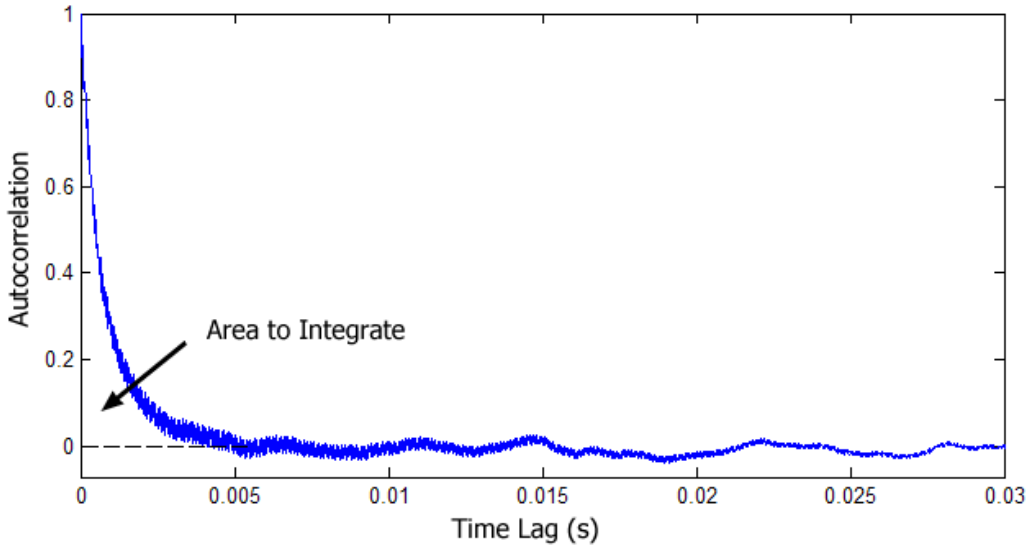

Figure 3.8.3 The integrated area up until the first zero is the integral time scale.

This time scale can be converted directly into an integral lengthscale using Taylor's hypothesis of frozen turbulence,

$$\Lambda_x = u_{mean} \cdot T \tag{3.8}$$

and the integral length scale, Λ_x, can be determined [5][6].

3.8.4 Turbulence Isotropy

The aim of grid design is to create homogeneous and isotropic turbulence in the flow field at varying levels of intensity for the even transfer of the turbulent energy into the boundary layer of the separated airfoils. Energizing the boundary layer, after all, is the mechanism by which to delay or reattach separation on the airfoil surface.

An initial estimate of the downstream distance required to create homogeneous flow from grid generated turbulence is ten mesh lengths [3]. Since the length from the grid to the center of the test section is well over 40 inches and the maximum mesh length used was 3.5 inches, it could be

assumed that the flow was homogenous. Still, it is standard practice to look at the distribution of turbulent energy in the frequency domain (the power spectral density) to prove that the turbulence is, in fact, uniform.

By finding the Fast Fourier Transform (FFT) of the fluctuating portion of the velocity signal

$$X(f) = FFT\ (u_i - u_{mean}) \tag{3.9}$$

and the frequency resolution,

$$\Delta f = \frac{f_s}{N} \tag{3.10}$$

the power spectral density (PSD) of the signal can be found using the equation

$$E(f) = \frac{2 \cdot X(f) \cdot X(f)^*}{\Delta f} \tag{3.11}$$

where $X(f)^*$ is the complex conjugate of the FFT of the fluctuating part of the velocity signal. Each velocity sample was initially broken into equal subsamples of size 2^n so that the FFT and PSD could be found for each sample and then averaged to get cleaner and more accurate plots. This technique is called frequency averaging.

The PSD was plotted for each case of Reynolds number and turbulence to see the energy distribution in the frequency domain. This type of plot can confirm the lengthscale, and show the level of isotropy relative to the Von Kármán relation for one dimensional spectra,

$$\frac{E(f) \cdot u_{mean}}{u'^2 \cdot \Lambda_x} = 4 \cdot \left(1 + \left(\frac{\kappa}{\kappa_e}\right)^2\right)^{-\frac{5}{6}} \tag{3.12}$$

Where the wavenumber is $\kappa = \frac{2\pi f}{u_{mean}}$, and the most energetic wavenumber is $\kappa_e = \frac{3}{4\Lambda_x}$ [4][5][6][7]. The most energetic eddies occur at the largest wavenumber where the energy spectrum begins to decrease, which is related to the integral length scale through the definition of

κ_e. By plotting the PSD with the correct integral length scale as shown in Figure 3.8.4, it can be seen that the energy spectrum begins to decrease around $\kappa_e \cdot \Lambda_x = {}^3/_4$ [6].

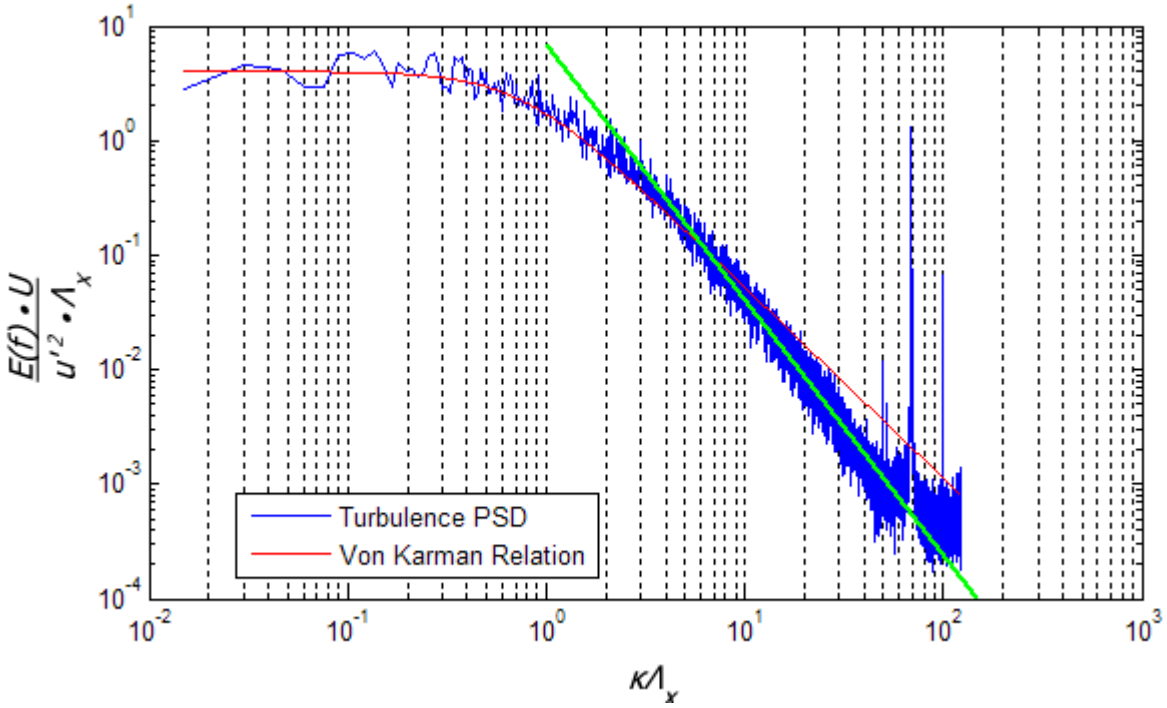

Figure 3.8.4 Typical power spectral density (PSD) graph used for isotropic analysis - data shown for Re = 125k subjected to turbulence grid B.

One of the characteristics of isotropic turbulence is a slope of ${}^{-5}/_3$ of decreasing energy with frequency according to the Von Kármán relation and Kolmogoroff Spectrum Law [4][7]. The green line in Figure 3.8.4 shows that the energy in the typical PSD plot dissipates with frequency at a slightly faster rate than predicted by the Von Kármán relation. But, one of the underlying assumptions of these functions is that they are used for sufficiently high Reynolds numbers with a large enough inertial subrange, and steeper slopes than predicted by Kolmogoroff have been shown to occur at lower values of mesh Reynolds number in the papers of Von Kármán, Sato, Gamard and George, and Biroak et al. to name but a few. The mesh Reynolds number, R_M , is found by the equation

$$R_M = \frac{u_{mean} \cdot M}{\nu} \tag{3.13}$$

where M is the mesh distance found in Table 3.8.1.1, and ν is the kinematic viscosity.

Three spikes can be seen at the high frequency end of Figure 3.8.4, implying that there are concentrations of energies (such as wakes) at these specific frequencies. These spikes are also present at the same frequencies at every level of turbulence and changed frequency when a different hotwire probe was used, so it can be safely assumed that they are vibrational natural frequencies of the hotwire and supports subjected to the flow.

3.8.5 Turbulence Performance Characteristics

Table 3.8.5 was generated from the averaged test data taken over the various angles of attack and stagger settings, Reynolds numbers, and turbulence intensities. Several things are apparent. The turbulence intensities were lower than the designed values of integer percentages of 2%, 4%, 6%, and 8% as discussed earlier. The lengthscale has a general trend of increasing, as expected, with increasing turbulence.

Table 3.8.5 Turbulence Performance Summary: Intensity, Integral Length Scale, and Mesh Reynolds Number.

Grid #	Tu (%)			Λ_x (m)			R_M		
	60k	90k	125k	60k	90k	125k	60k	90k	125k
FS	0.86	0.82	1.13	-	-	-	-	-	-
A	1.79	1.81	1.82	0.0115	0.0123	0.0202	29057.3	43617.1	60572.4
B	3.48	3.56	3.37	0.0275	0.0227	0.0223	58114.6	87234.2	121145
C	4.68	4.78	4.70	0.0273	0.0284	0.026	81360.4	122128	169603
D	7.26	7.70	7.15	0.066	0.0566	0.0382	81360.4	122128	169603

3.8.6 Turbulence Summary

Generating turbulence with grids is an inexpensive, easy, and reliable way to generate nearly isotropic turbulence. Although the originally desired integer levels of turbulence intensity were substituted with lower and more arbitrary levels, these are still satisfactory in a testing schema.

The quantities that must be known for experiments with turbulence are the turbulence intensities and lengthscales, and a qualification of isotropy. These, along with the mesh Reynolds number, have been specified for each test case performed.

Chapter 4

Experimental Design and Procedure

The goal of this research was to observe the influence of turbulence intensity on separation at different low Reynolds numbers and settings of angle of attack and stagger. A test matrix (shown in Table 4.0) was created to test all of these variables, and to quantify changes in performance and observe the effect on separation. The maximum angle of attack chosen was 17.5 degrees because between this angle and 20 degrees, at a slightly higher Reynolds number, gross separation and reversed flow have been recorded for similar setups [1][2]. The current instrumentation was not capable of measuring reversed flow, so it has been designated beyond the scope of this research. The stagger angles of 25 degrees and 37.5 degrees were chosen so as to match and compare results with previous literature.

Table 4.0 Experiment design parameters

Stagger Angle, ξ	Angle of Attack,	Reynolds Number	Turbulence Intensities
25	0	125k	FS, A, B, C, D
		90k	FS, A, B, C, D
		60k	FS, A, B, C, D
	6	125k	FS, A, B, C, D
		90k	FS, A, B, C, D
		60k	FS, A, B, C, D
	12	125k	FS, A, B, C, D
		90k	FS, A, B, C, D
		60k	FS, A, B, C, D
	17.5	125k	FS, A, B, C, D
		90k	FS, A, B, C, D
		60k	FS, A, B, C, D
37.5	0	125k	FS, A, B, C, D
		90k	FS, A, B, C, D
		60k	FS, A, B, C, D
	6	125k	FS, A, B, C, D
		90k	FS, A, B, C, D
		60k	FS, A, B, C, D
	12	125k	FS, A, B, C, D
		90k	FS, A, B, C, D
		60k	FS, A, B, C, D
	17.5	125k	FS, A, B, C, D
		90k	FS, A, B, C, D
		60k	FS, A, B, C, D

Each test followed the same 9 step procedure to calibrate the hotwire and acquire data over two wakes and one passage:

1) Record the Atmospheric Conditions
2) Calibrate and Tune the Hotwire
3) Set the Reynolds Number
4) Traverse Upstream with Hotwire for Turbulence Measurements
5) Traverse Downstream Nulling with 3-hole Probe, find wake locations
6) Traverse Upstream with 3-hole Probe in the Non-Nulling Mode
7) Remove Probes and Record the Static Pressure Taps from the Blade Surfaces
8) Reduce Data, Check for Inconsistencies, Retake any Measurements Necessary

The default measurement increment of the hotwire was 0.25" upstream of the cascade, to confirm local turbulence uniformity. After an initial air test to determine an acceptable measurement increment for the pneumatic sweeps, a grid-adapted approach was utilized as a compromise between measurement accuracy and testing time. The default measurement increment was 0.05" except in the wakes, where it was reduced to 0.025." After an initial downstream search for the wake locations, the downstream sweep locations and measurements were recorded and the upstream locations were placed on matching streamlines to record data.

Finally, oil flow visualization was performed to be verify the separation locations shown in the static tap data. Russ outlined a method for oil flow visualization, painting the blades with a mixture of 40 ml diesel fuel, 10 g of titanium dioxide, and 2 drops of oleic acid [1]. The titanium dioxide (white paint pigment) was left as streaks or lines on the black airfoil surface as the diesel followed the boundary layer airflow and evaporated.

Chapter 5

Experimental Results and Discussion

In this chapter the results of the investigation are presented and discussed. The first two sections tell the details of the test conditions by describing the wind tunnel boundary layer and summarizing the flow and turbulence uniformity at the test cross section. The axial velocity ratios (AVRs) of the test cases are presented to qualify acceptable two dimensionality of the cascade.

The third section presents the qualitative analysis of the effect of turbulence on separation by presenting the static tap data and confirming local boundary layer behavior with flow visualization for several cases. Finally, the effects of Reynolds number and turbulence on separation, and the effect of separation on performance are investigated in depth.

5.1 Tunnel Qualification

Ideal conditions in a wind tunnel are those that support data accuracy and repeatability. Therefore, the initial testing of this research began with the test cross section being checked for boundary layer size, flow uniformity, and turbulence levels to fully investigate the operating conditions and characteristics. Special attention was also given to searching these variables for gradients, patterns, and abnormalities, as these are typical indicators of non-repeatable test conditions.

5.1.1 Boundary Layer

It is important to measure the size of the wall boundary layers in wind tunnel research, both as a quantified characteristic of the specific tunnel used, and a limitation of useable cross sectional area within the tunnel. The tunnel was scanned pitch-wise with a hotwire anemometer at the

maximum and minimum Reynolds numbers from a distance of 0.1” off the top and bottom of the test cross section. Figure 5.1.1 shows that the boundary layer extends approximately 1.75” into the flow in the pitch-wise direction. As the location and size of the measured passage and wakes fell well away from the edges of these boundary layers, it is safe to assume that their effect is minimal in this study. Additionally, since the test cross section is square, any assumptions lent to the pitch-wise direction can also be lent to the span-wise direction.

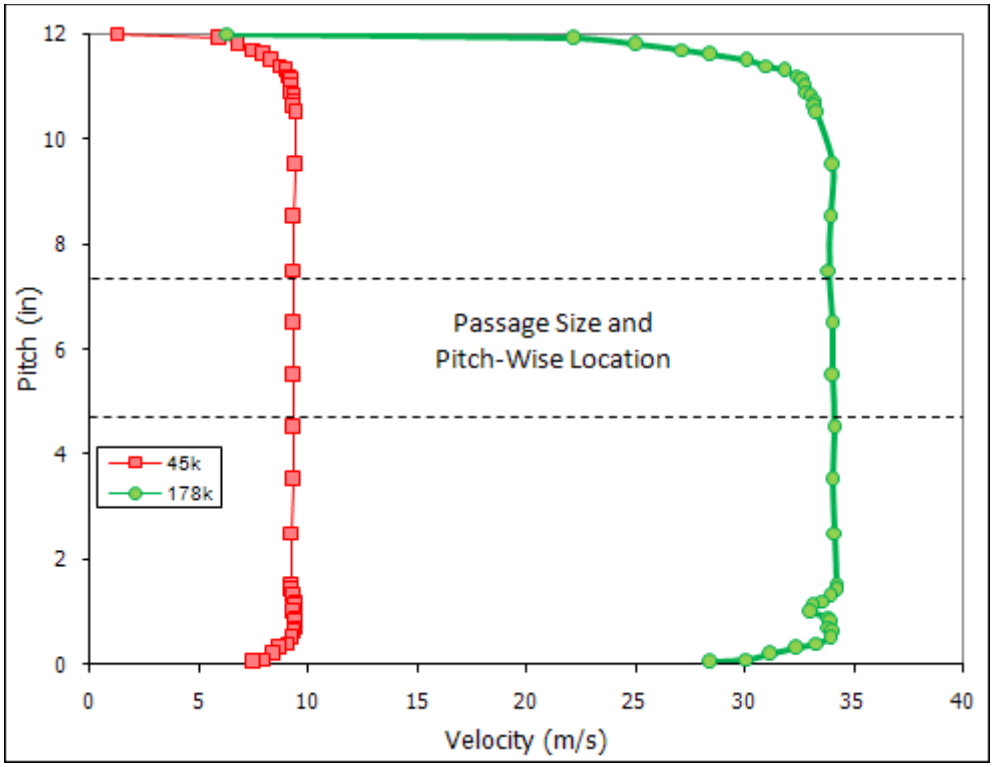

Figure 5.1.1 A graph of the boundary layer at minimum and maximum Reynolds numbers.

5.1.2 Flow Uniformity

In order to get repeatable and meaningful results in cascade testing, the flow uniformity must be characterized over the range to be tested. The useable cross sectional area of the wind tunnel was divided into increments in both the x and y directions, creating a grid test pattern as shown in Figure 5.1.2A. The outer test points were kept two inches from the walls so as not to collect data in the boundary layer. This testing schema was used at all three Reynolds numbers and at

each turbulence level (including the free stream level) to collect data for both the flow and turbulence uniformity.

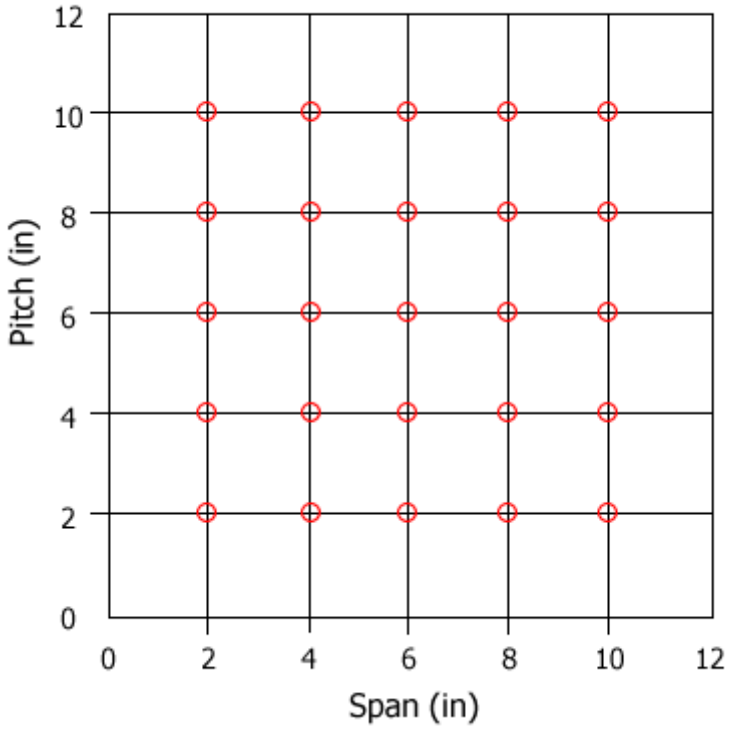

Figure 5.1.2A The map of test points used for tunnel qualification, looking into the flow.

The main indications of an abnormality in regards to uniform flow velocity are values either much higher or much lower than the statistical average for a particular Reynolds number, regardless of the turbulence intensity. Table 5.1.2 is a summary of this data, including the average velocity and the highest and lowest deviations from the average occurring in the specified data set.

Table 5.1.2 Summary of qualification velocity data for all turbulence and Reynolds Numbers

		Velocity (m/s)		
Re	*Tu Grid*	Avg.	Low Dev.	High Dev.
125k	FS	29.948	0.384	0.296
	A	29.510	0.447	0.626
	B	29.637	1.034	1.111
	C	29.796	1.063	0.946
	D	29.119	1.975	1.803
90k	FS	21.056	0.199	0.173
	A	20.884	0.302	0.482
	B	21.392	0.753	0.918
	C	21.302	1.215	0.941
	D	20.660	1.219	1.133
60k	FS	14.801	0.080	0.082
	A	14.493	0.284	0.354
	B	14.780	0.456	0.378
	C	14.675	0.663	0.476
	D	14.117	0.838	0.665

With only several exceptions, the high and low deviations from the statistically averaged velocity at each Reynolds number become larger with higher turbulence. This is not very surprising as turbulence intensity depends directly on variations in velocity, but still, the maximum deviation from the average velocity at every point, for all cases, is less than 7%.

Ideally, deviations from the average velocity would be distributed randomly within the test cross section, eliminating the possibility of a velocity gradient. This can be verified visually by plotting the velocity values against a spatial representation of their location in the test cross section, and allowing an interpolation function between points to see trends more clearly. Figure 5.1.2B shows a typical velocity distribution of the flow during the qualification of the tunnel. There are no apparent large trends across the test cross section, and the color bar shows a very small velocity range.

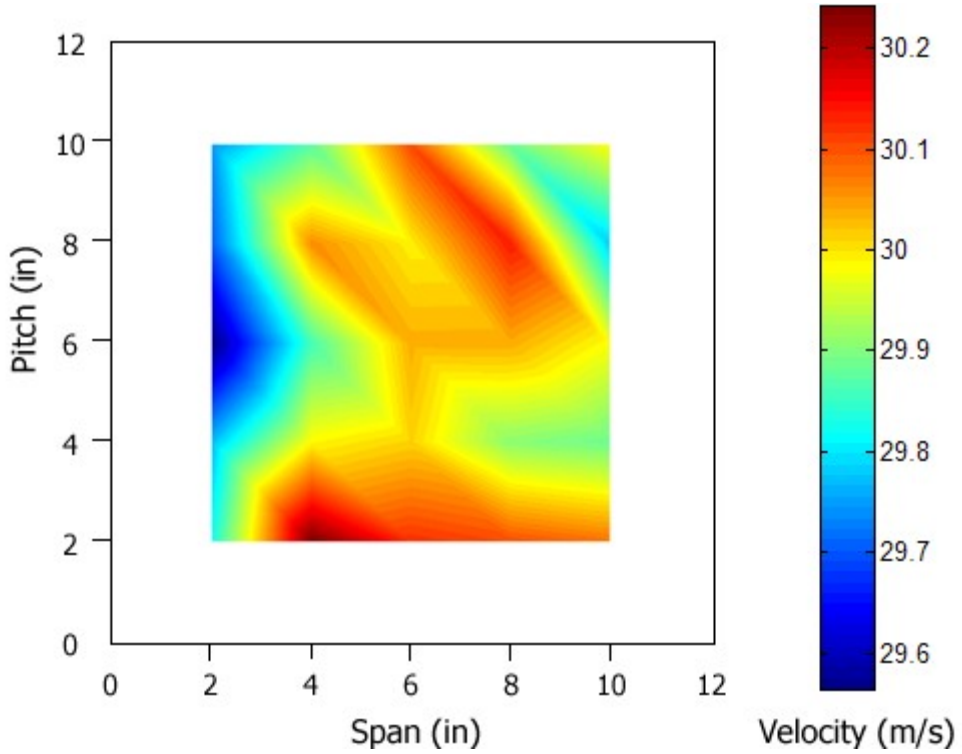

Figure 5.1.2B A spatial graph of the flow velocity in free stream turbulence at Re = 125k.

Exceptions found to the typically random velocity distributions in other cases were the flows subjected to grid C (about 5% turbulence) at all three Reynolds numbers. Figure 5.1.2C shows the velocity distributions at Re = 6 x 10^4, which is typical of the velocity trends at the other two tested Reynolds numbers. Slower flow in the middle of the test cross section can be clearly observed. While obvious, this trend had no contribution to or observable impact on any test results, and the overall velocity deviations were close to those typical of all other uniformity tests.

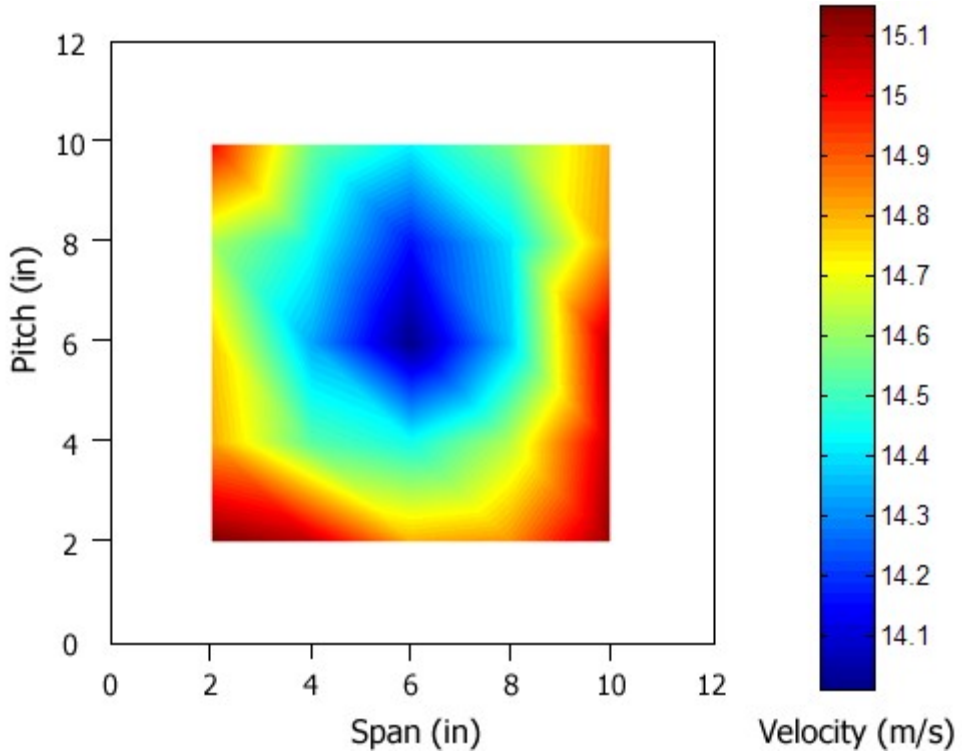

Figure 5.1.2C The velocities subjected to grid C at all Reynolds numbers show a spatial velocity trend.

5.1.3 Turbulence Uniformity

Producing uniform turbulence was equally important to test repeatability. The turbulence intensities were found from the same measurements used to find the velocities in the previous subsection, with increases in turbulence intensity deviation with increasing intensity level, similar to the velocities. The average turbulence level of each test case is shown in Table 5.1.3, as well as the highest and lowest deviation from this average.

Table 5.1.3 Summary of qualification turbulence data for all turbulence and Reynolds numbers.

		Turbulence Intensity (%)		
Re	*Tu Grid*	Avg	Low Dev.	High Dev.
125k	FS	0.74	0.12	0.14
	A	1.82	0.11	0.10
	B	3.80	0.24	0.38
	C	4.97	0.27	0.43
	D	7.65	0.79	0.57
90k	FS	0.66	0.14	0.17
	A	1.88	0.16	0.15
	B	3.82	0.27	0.38
	C	5.20	0.38	0.30
	D	8.32	0.84	0.89
60k	FS	0.65	0.13	0.09
	A	1.63	0.18	0.10
	B	3.44	0.30	0.66
	C	4.77	0.37	0.44
	D	7.34	0.61	0.65

The deviation of turbulence from the average is typically low, and only around 10% in a few cases. Considering the proximity of the outer test points in the schema to the measured boundary layer, (and knowing that it can certainly have a contribution to turbulence levels) these turbulence deviations are considered acceptably low.

It is important for background turbulence characteristics in the flow field to be identified, especially when producing turbulence in an experiment. Turbulence generation in an already turbulent flow-field can cause both larger and less predictable generation than would be expected with prescribed grids, as the overall level is a combination of different flow fields instead of just simple generation [3]. While efforts can be made to reduce the background turbulence level, its identification is the only requirement for future testing repeatability. From the three settings of free stream Reynolds numbers, this level was found to be between 0.74% and 0.65%, depending on Reynolds number.

The differences between turbulence intensities for a given grid (or free stream) at different Reynolds numbers are around the same magnitude as the deviations of turbulence with Reynolds number previously mentioned, but certainly still higher than the averages found during the actual testing shown in Table 5.1.3. Also, there could an explanation for some of the small variation of Tu with Reynolds number by considering the grid design. Realizing that at the set distance x_{turb} the turbulence intensity depends on the grid design constant C from Equation 3.4**,** which was suggested to possibly vary with Reynolds number, then the turbulence intensity would also vary with Reynolds number.

The turbulence uniformity tests showed no apparent large spatial trends. A plot typical of all turbulence deviation data is shown in Figure 5.1.3.

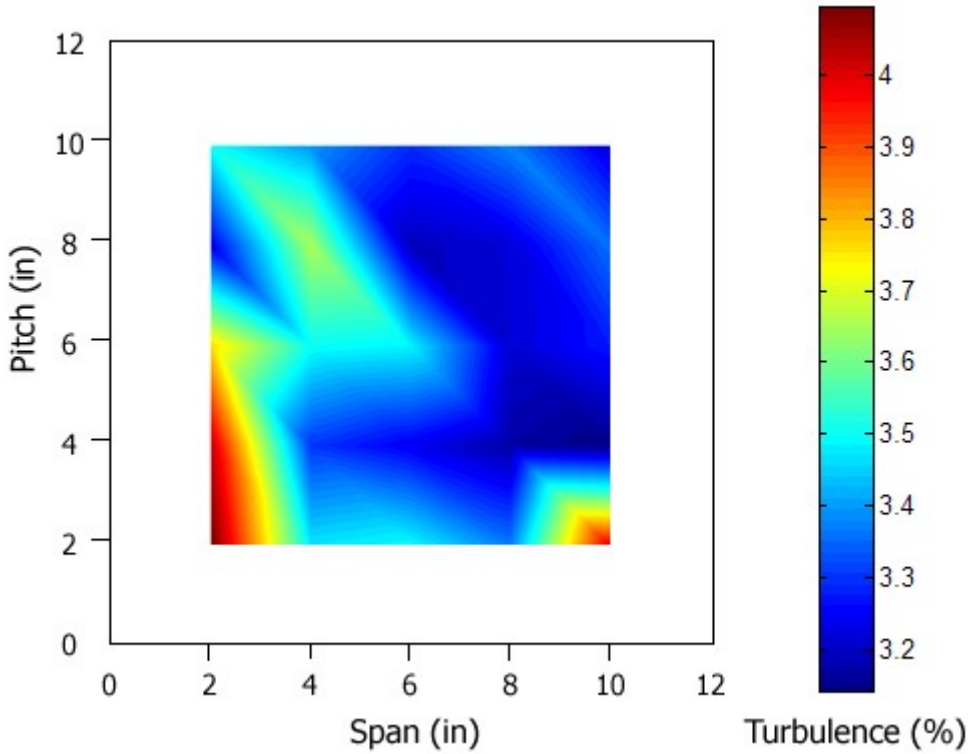

Figure 5.1.3 A spatial graph of Re = 60k and turbulence from Grid C is representative of all data, lacking trends in turbulence intensity.

5.1.4 Tunnel Qualification Summary

For reliable measurements in airflow, that flow must be checked for several different characteristics and uniformities. Those checked in this study were velocity and turbulence uniformity, as well as a measurement of the boundary layer, and flow isotropy in the previous section. Having found the flow and turbulence to be satisfactorily uniform and without observable trends, and given that measurements were made well out of the boundary layer, the experimental setup for this research was considered satisfactory.

5.2 Axial Velocity Ratio

The flow within any cascade used for airfoil testing must be investigated for two dimensionality by calculating the axial velocity ratio (AVR) as one of the tunnel characteristics, and especially in tunnels with solid sidewalls [26]. Corner stall at the junction of the blades and sidewall will grow from the boundary layer and begin to block the flow at the sides of the cross section, causing it to accelerate across the blades at mid-span, and raising the AVR above unity. This ratio, defined in equation 2.5, is derived from the conservation of mass.

One of the ways to combat this problem is with blades of higher aspect ratio, such as those used in this study. For solid walled cascades an aspect ratio of at least 3.0 is recommended to preclude secondary flow effects in mid-span measurements [17]. Also, an accepted limit for two dimensionality in a cascade is an AVR under a value of 1.1 [2]. As mentioned in section 3.2, the aspect ratio of the blades used in this study was 4.70.

Figure 5.2A shows the results for AVR calculation at various angles of attack at different Reynolds numbers and at two staggers. It can be seen that the AVR stays around a value of unity, and in most cases is actually less. This can be attributed to different degrees of boundary layer separation occurring on the blade surface as the flow approaches full separation. A similar trend was observed by Yocum for his single Reynolds number, and he attributed it to the nonlinear separation line (or 3D separation) in the transitional angles of attack between boundary

layer separation and full stall [2]. There was no attempt to modify this ratio because of the complexity that would be required to modify the tunnel for side wall boundary layer removal.

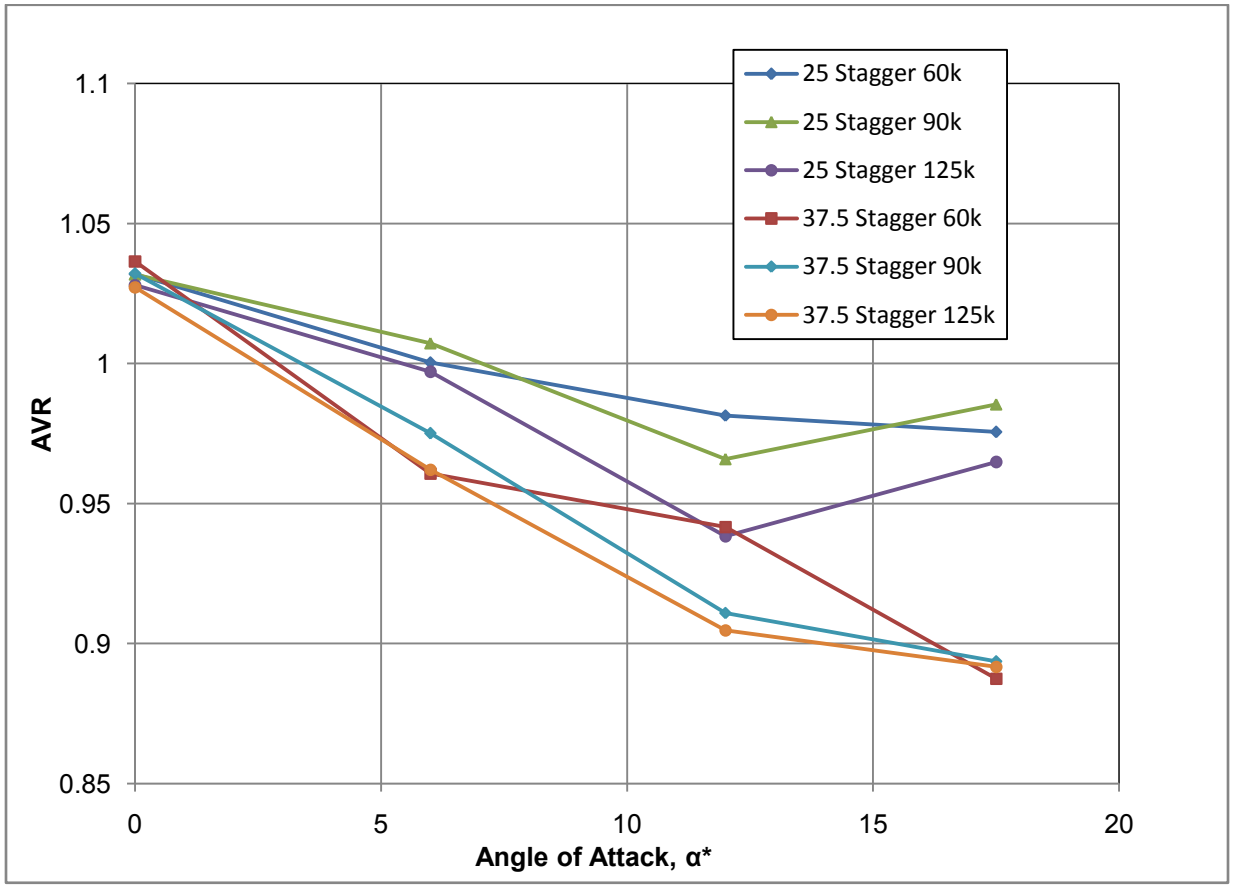

Figure 5.2A The axial velocity at different values of stagger, Reynolds number, and AOA.

There are trends that can be seen in Figure 5.2A, most notably the general decrease of AVR with increasing angle of attack as also noticed by Yocum. Besides this, the 37.5 stagger also results in a decrease in AVR more rapidly than for the 25 degree stagger, and lower Reynolds numbers in either stagger have a generally higher AVR than high Reynolds numbers.

Using the axial velocity ratio to estimate the two dimensionality of the flow is an option. By using surface oil flow visualization the existence and effect of non steam-wise flow was apparent. Figure 5.2B shows the surface oil flow pattern on a blade from mid span out towards

the side wall, with a straight separation line perpendicular to the flow except in the boundary layer region. For all intensive purposes of the present experiment, the flow in this cascade was considered two dimensional.

Figure 5.2B Two dimensionality from oil flow visualization

5.3 Qualitative Analysis of Separation

Although changes in Reynolds number and increased free stream turbulence certainly affect separation, the effect of their variations are small compared to the effect of varying the angle of attack. Thus, a good starting point to familiarize the reader with the results is to hold the other parameters constant and look at the progression of separation over the range of angle of attack, and then to describe the effect of the other variables separately. Through this method the types of separation can also be investigated concurrently.

5.3.1 Preliminary Separation Investigation

There were certain consistent boundary layer separation characteristics seen throughout this research at set angles of attack. Given a nominal 25 degree stagger angle and a Reynolds number of 12.5×10^4, Figure 5.3.1A shows the natural progression of separation with increasing angle of attack. The top lines (red) are the static pressures of the suction sides of the blades, and

the bottom lines (blue) are the static pressure coefficients of the pressure sides. The difference between the suction and pressure sides of static tap graphs is the lift per unit area produced by the blade.

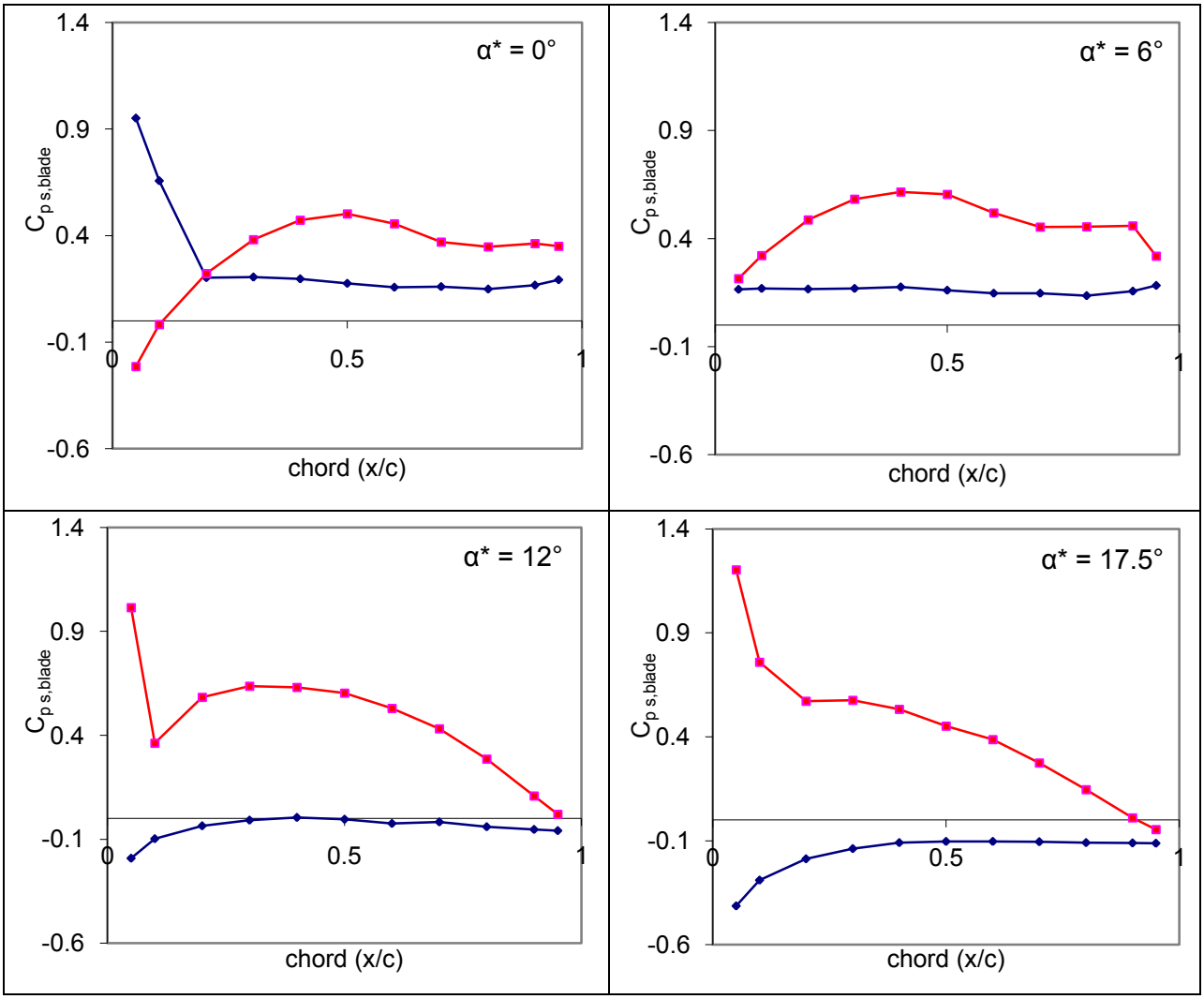

Figure 5.3.1A Progression of separation at Re = 12.5 x 10^4, and ξ = 25º, with free stream *Tu*.

The similar separation characteristics of the static pressure profiles at the four angles of attack make each of them easily identifiable when varying the other parameters. Since the blades have a camber line angle of incidence of about 8°, they are actually at -8° incidence at zero angle of attack (AOA). The negative incidence angle explains why there is leading edge separation on

the pressure side in addition to trailing edge separation over the last 20% of the suction side blade chord.

At 6° AOA, the pressure side separation is gone, and the suction side has a laminar separation bubble after mid chord. With further increase in angle of attack, there is no further pressure side separation, and the suction side trailing edge separation progresses to leading edge separation until the maximum angle of attack. Figure 5.3.1B shows a comparison between static tap measurements and oil flow visualization for the suction side surface of the blades at 0° and 6° angle of attack.

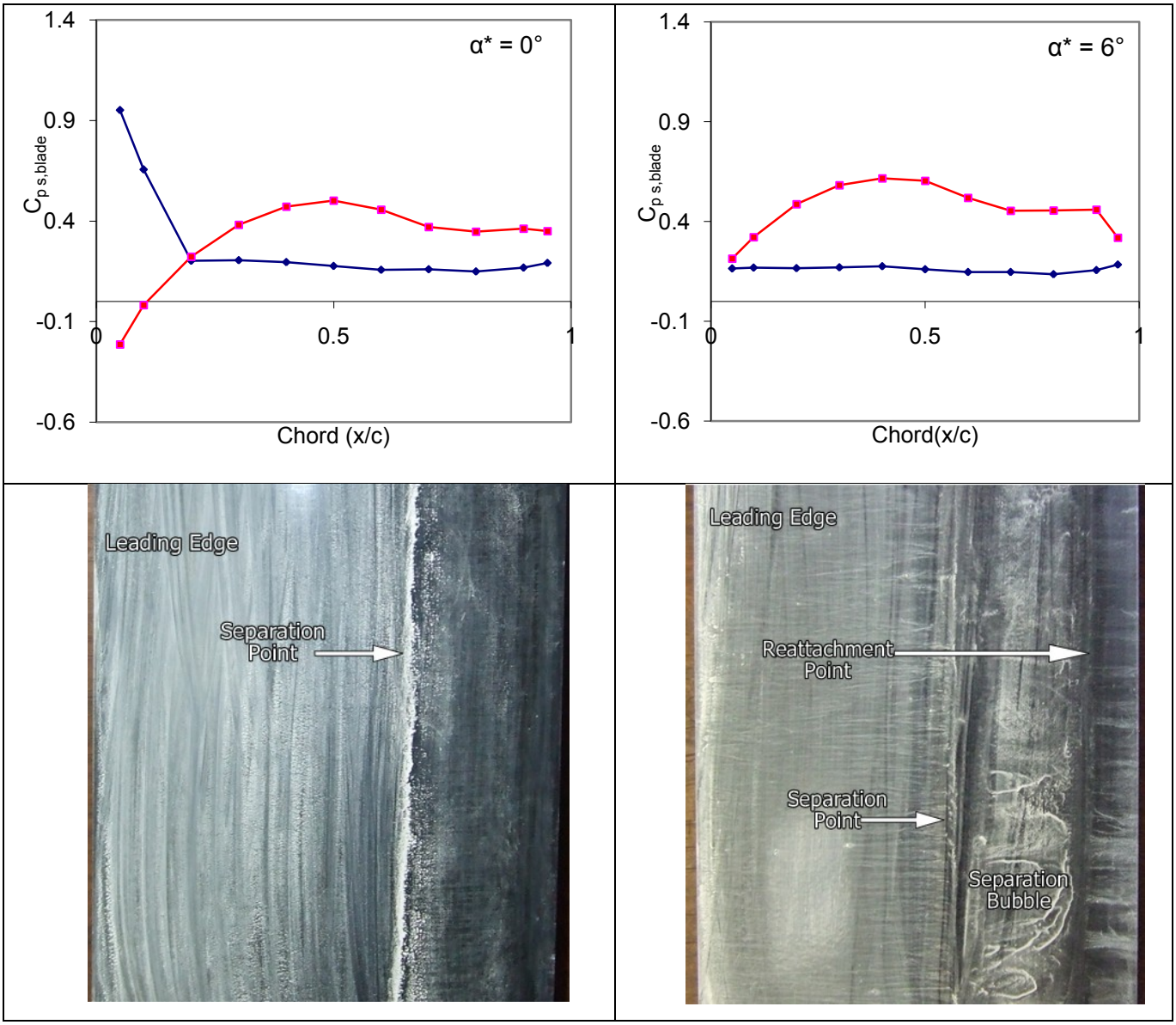

Figure 5.3.1B Static tap data matched with oil flow visualization for the blade suction sides for α* = 0° and α* = 6°.

The increased suction side pressure coefficient near the trailing edge (seen as a flat line in the static pressure graphs) is due to the increased airspeed (and thus static pressure drop) above the blade surface as the flow is diverted by the separated regions. In the case of 6° AOA, the suction

side static taps clearly show that the trailing edge flow has turned back towards the blade surface, progressing toward reattachment.

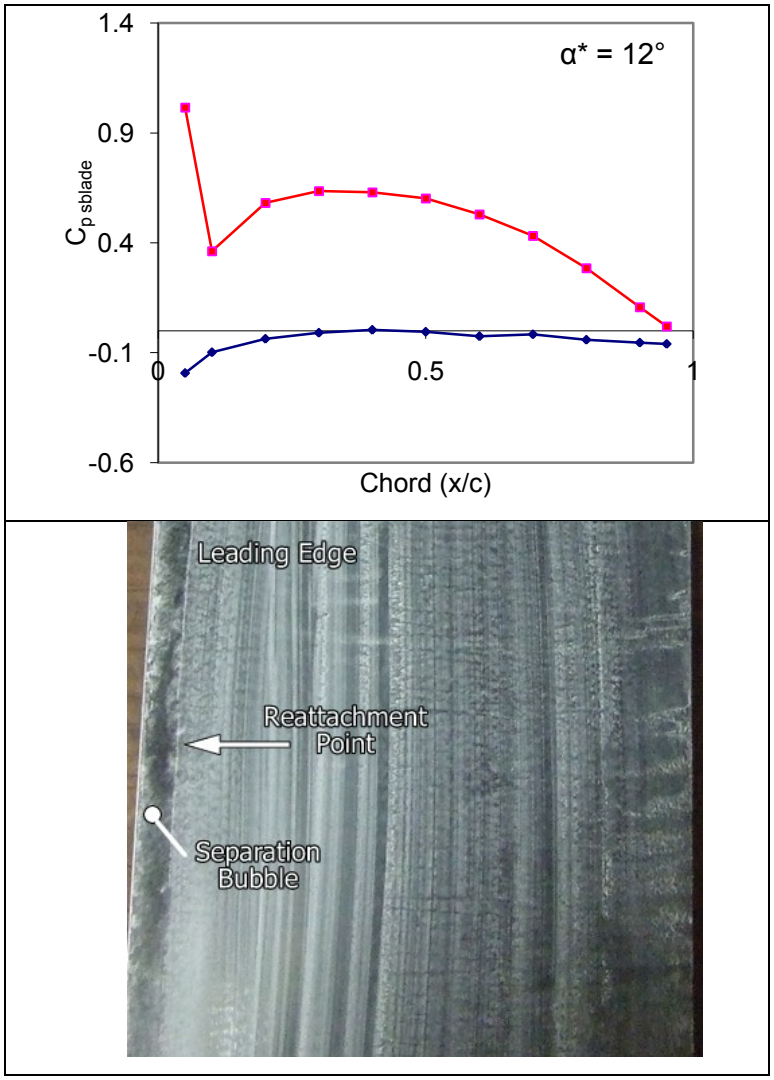

Figure 5.3.1C Static tap data matched with oil flow visualization for the blade suction side.

Figure 5.3.1C shows a similar matching, this time with leading edge separation and reattachment on the suction side surface, produced by high values of angle of attack. It is representative of the flow for both the 12º and 17.5° angles of attack.

It is imperative to visualize and understand the boundary layer separation behavior to enable key assumptions later in the research. By matching the oil flow visualization with the static tap data we can make confident predictions of the flow behavior, which will be important in performance analysis.

5.3.2 Separation effects based on turbulence

This section discusses the effect of turbulence on separation at constant angles of attack and Reynolds numbers. With respect to this study, this section is by far the most valuable in terms of the qualitative behavior analysis of turbulence. Visual evidence of the ability of turbulence to delay separation and promote reattachment is presented throughout.

With three settings of Reynolds number and four settings of angle of attack, there are twelve cases at both stagger settings to demonstrate the effects of turbulence on boundary layer behavior. The most illustrated cases will be discussed in this text while the entire data set is documented in Appendix B.

One of the most apparent trends visible in the 0º AOA setting in Figure 5.3.2A is the reattachment of the flow at the trailing edge of the suction side. At the minimum free stream turbulence level, the flow is detached just past the midpoint as in 5.3.1A. With increasing turbulence it reattaches, forms a separation bubble, and finally appears to be fully attached when subjected to the high turbulence level produced by grid D.

For the pressure side, the leading edge separation looks similar to previous figures with only slight change (reduction) with increasing turbulence. Of note though, is that towards the trailing edge of the pressure side with low free stream turbulence, it appears as though the separation from the suction side of the neighboring blade is causing the air above the pressure side of the blade above to flow faster, resulting in reduced static pressure coefficients. Thus, at the minimum free stream turbulence level the pressure and suction lines of the pressure coefficient curves are closest together, producing the least pressure integral and indicating the lowest lift.

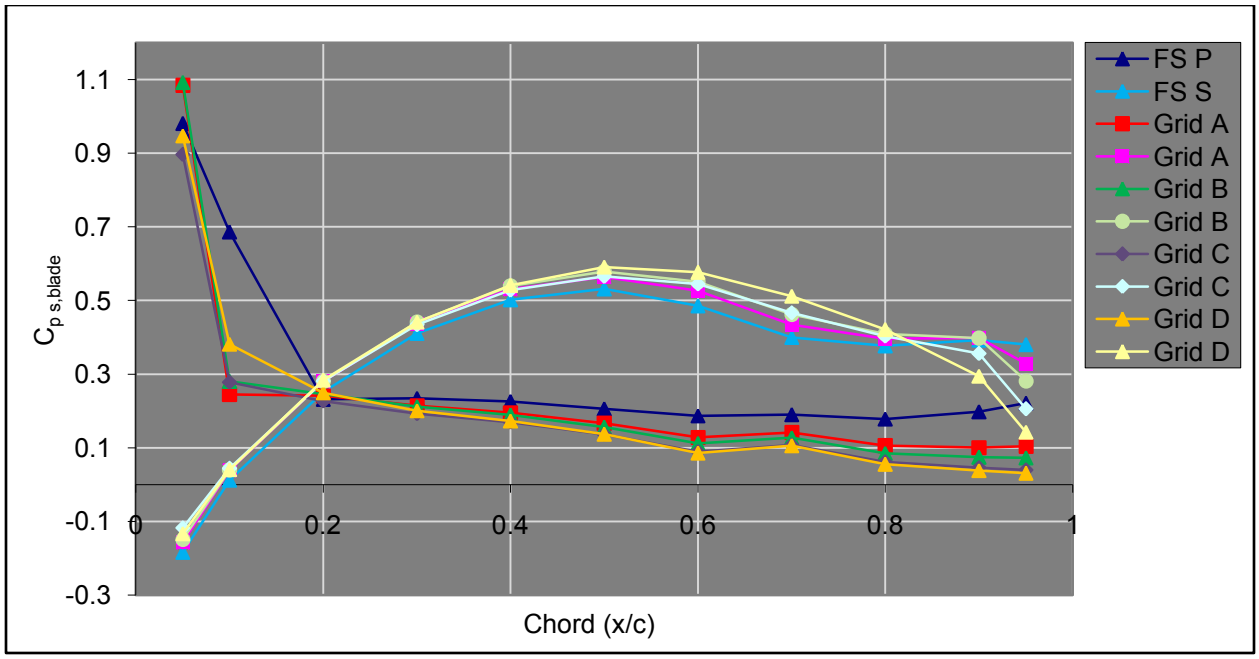

Figure 5.3.2A Static tap graphs for $\xi = 25°$, $\alpha^* = 0°$, Re =12.5 x 10^4, for all turbulence levels.

This same trend is shown more clearly at the lower Reynolds number in Figure 5.3.2B, with the entire range of separation to full reattachment on the suction side at 6º AOA.

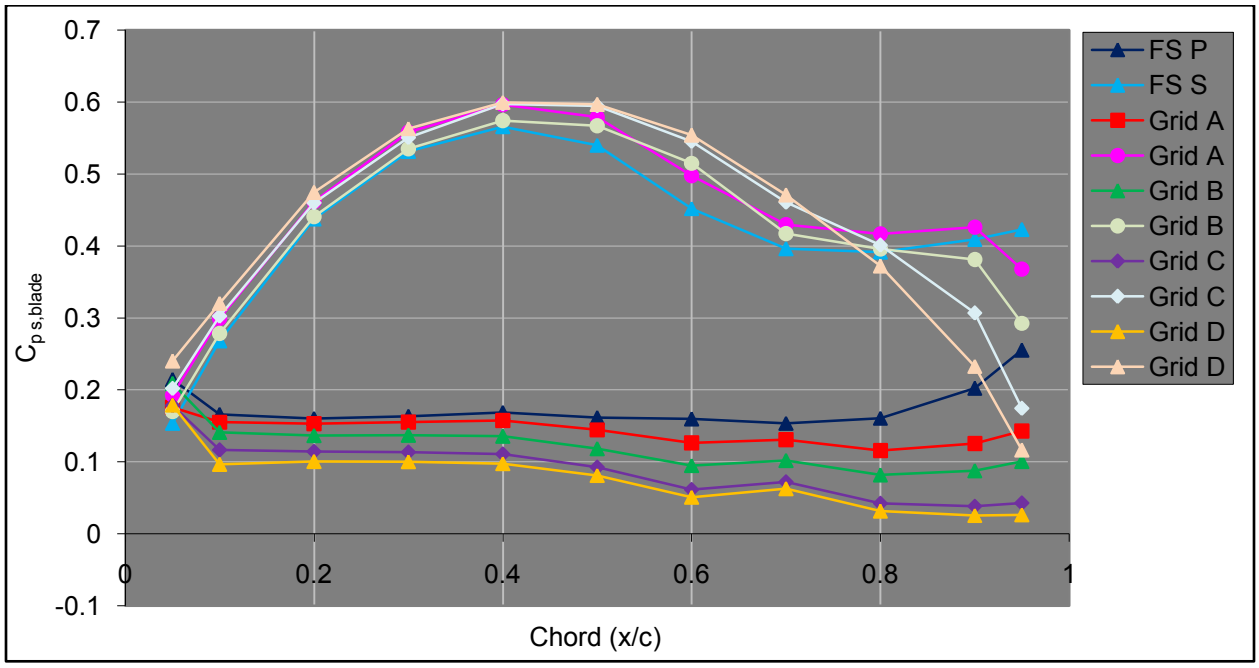

Figure 5.3.2B Static tap graphs for $\xi = 25°$, $\alpha^* = 6°$, Re = 9 x 10^4, for all turbulence levels.

For the leading edge separation of 12° AOA in Figure 5.3.2C, the flow never becomes fully attached at the leading edge, but there is obviously a contribution from the turbulence to trailing edge reattachment and the size of the separation bubble. At even larger angles of attack, Figure 5.3.2D shows the same trend but with much more severe leading edge separation because of the lower Reynolds number. One thing to note for both Figures 5.3.2C and 5.3.2 D is that although there is severe leading edge separation with higher angles of attack, the flow is attached for 90% of the blade chord, including most importantly the trailing edge of the suction side, and the entire pressure side.

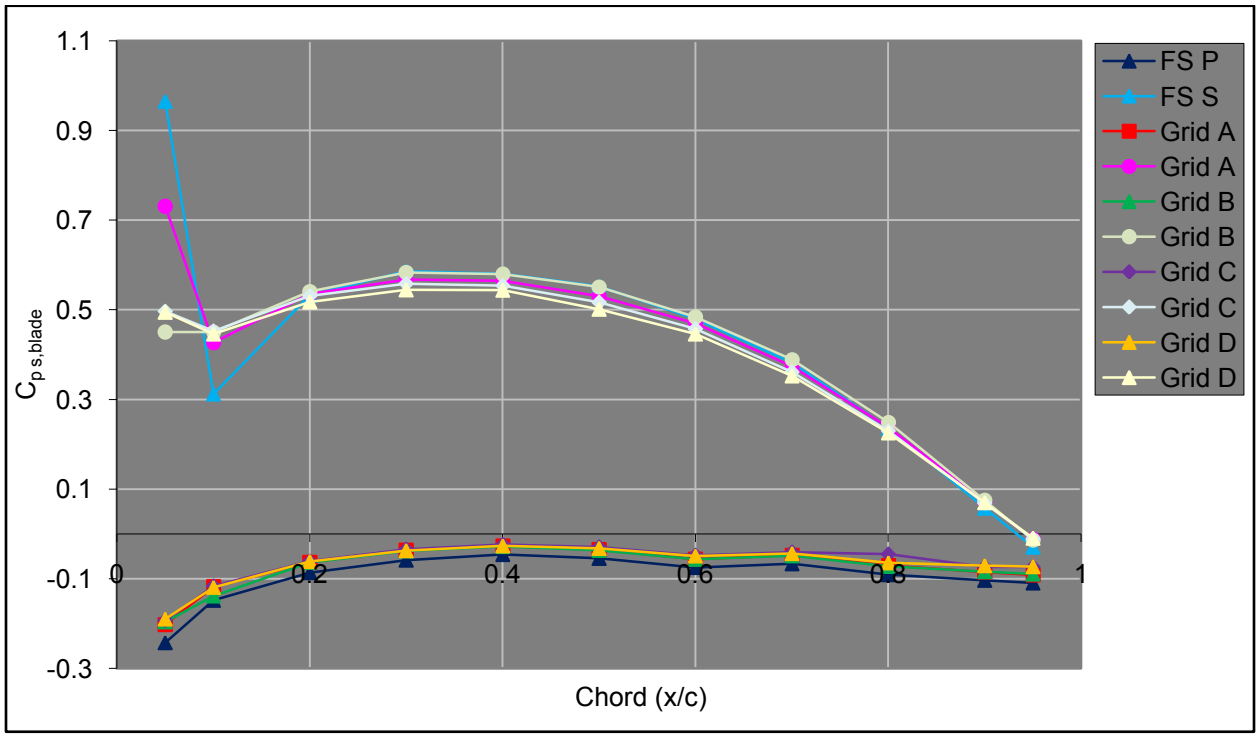

Figure 5.3.2C Static tap graphs for $\xi = 25°$, $\alpha^* = 12°$, $Re = 12.5 \times 10^4$, for all turbulence levels.

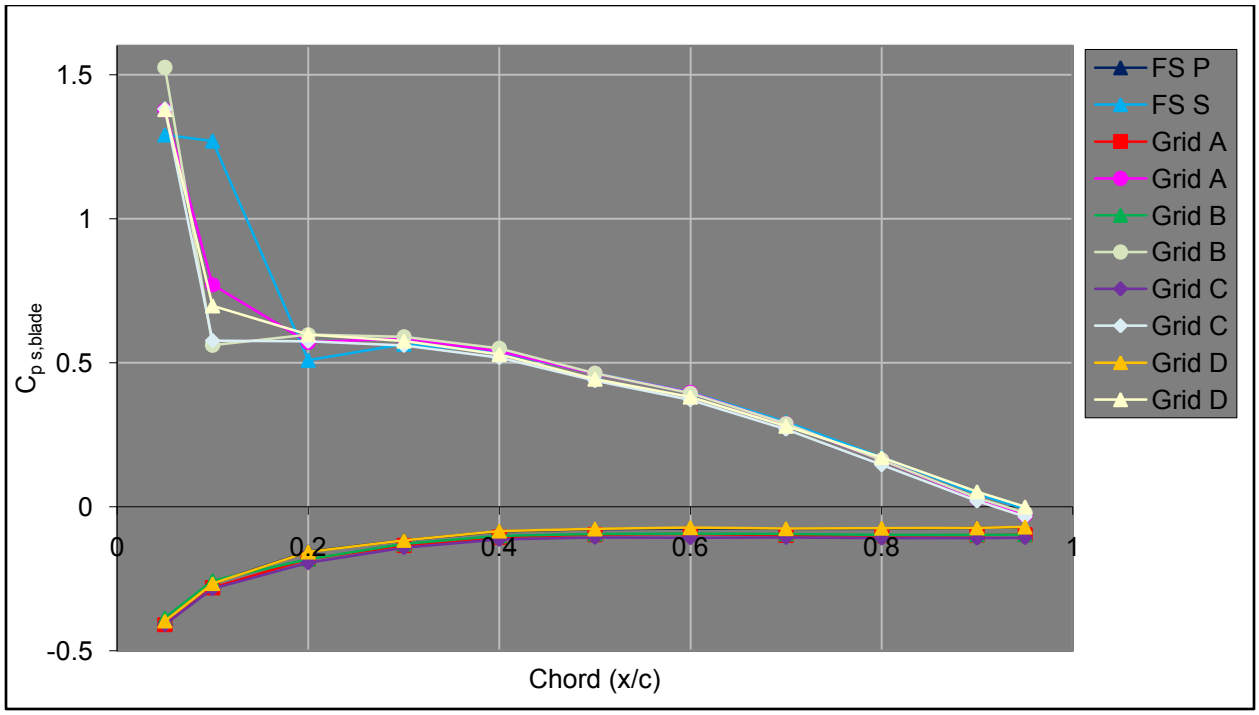

Figure 5.3.2D Static tap graphs for $\xi = 25°$, $\alpha^* = 17.5°$, Re = 6 x 10^4, for all turbulence levels.

5.3.3 Separation effects based on Reynolds numbers

As it turns out from the results of this experiment, it is shown that increases in Reynolds number, on a strictly percentage increase basis, have a greater impact on separation than an equivalent percentage increase of free stream turbulence, if all other variables are held constant. However, large percentage increases in turbulence intensity are relatively easy to produce, and are relevant to typical turbomachine operating conditions. Within the range of Reynolds number and turbulence intensity available in this experiment, we were able to produce more robust reattachment with increases in turbulence intensity.

Figure 5.3.3 shows that for a set stagger, angle of attack, and turbulence levels, the effect of increasing Reynolds number delays separation. When comparing Reynolds number and turbulence intensity in Figure 5.3.3, it is important to keep in mind the magnitudes of turbulence intensity based on grid size from Table 3.8.5. While the Reynolds number doubles over the

experiment range, the turbulence intensity increases by almost tenfold. Thus, full reattachment can be seen at the higher increases in turbulence, and not necessarily Reynolds number.

One thing that is noticeable is that the distance (and therefore the integral) has increased between the pressure and suction side curves in general, showing that with increased Reynolds number, for these parameters, there is more lift. These trends in Reynolds numbers can be checked with the data in Appendix B.

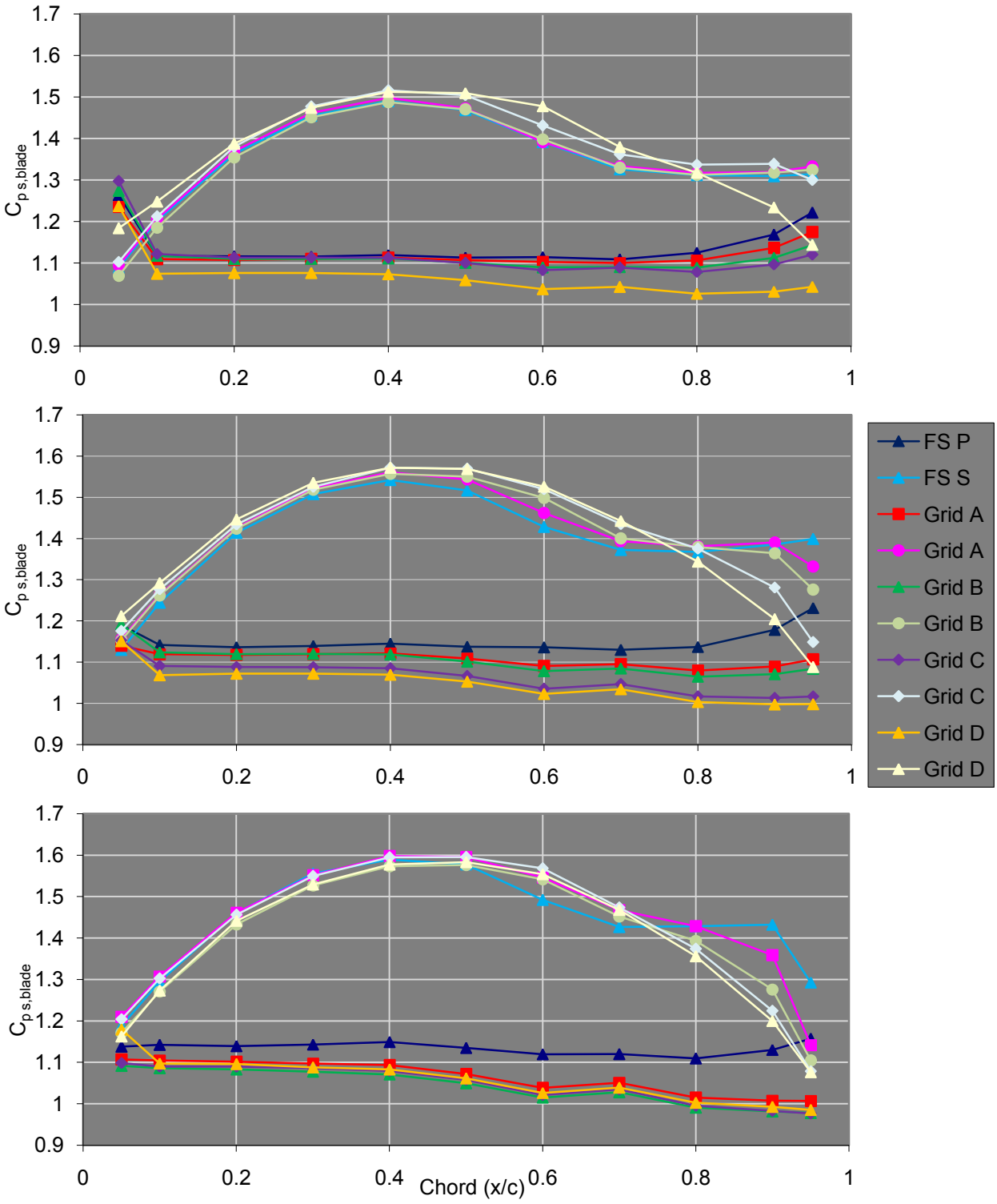

Figure 5.3.3 Static tap graphs for $\xi = 37.5°$, $\alpha^* = 6°$, Re = 6 x 10^4 (top) Re = 9 x 10^4 (middle) and Re = 12.5 x 10^4 (bottom).

5.3.4 The Effect of Turbulence on Performance

The performance of the compressor cascade is based on the total pressure loss coefficient in this study. The anticipated result was that by increasing free stream turbulence to delay or reattach separation, the loss coefficient would remain low at Reynolds numbers and angles of incidence where there normally would have been substantial losses. The caveat though, is that turbulence itself is a lossy mechanism for energy transfer to the boundary layer, and can have a negative effect on performance itself.

One problem encountered in this study was that as turbulence increased, expectedly, so did the fluctuations in total pressure measurements in the passages. The mass-averaged loss coefficient yields lower losses because of its implication that the losses in the wakes contribute less overall because of the reduced mass flow rate in the wake. The other side of this implication is that any losses in the passage at higher flows are greatly magnified. Combining the uncertainty of the total pressure measurements due to turbulence intensity with their magnified effect on the loss coefficient, the result is that even the slightest averaged total pressure loss increase due to turbulence within a passage eclipses any changes of losses in the blades wakes from separation with varying turbulence levels.

Thus, with the assumption that the turbulence is isotropic so that there should not be any bias (and that losses in the passage are naturally low), the coefficient of total pressure was normalized over the passages to remove any random bias, and the cascade loss coefficient was found to be dependent on both the wakes and the free stream turbulence level, but with different magnitude, with changes in angle of attack. The results of these measurements and calculations for loss coefficient are shown in Figure 5.3.4A, with a following discussion of the interesting implications.

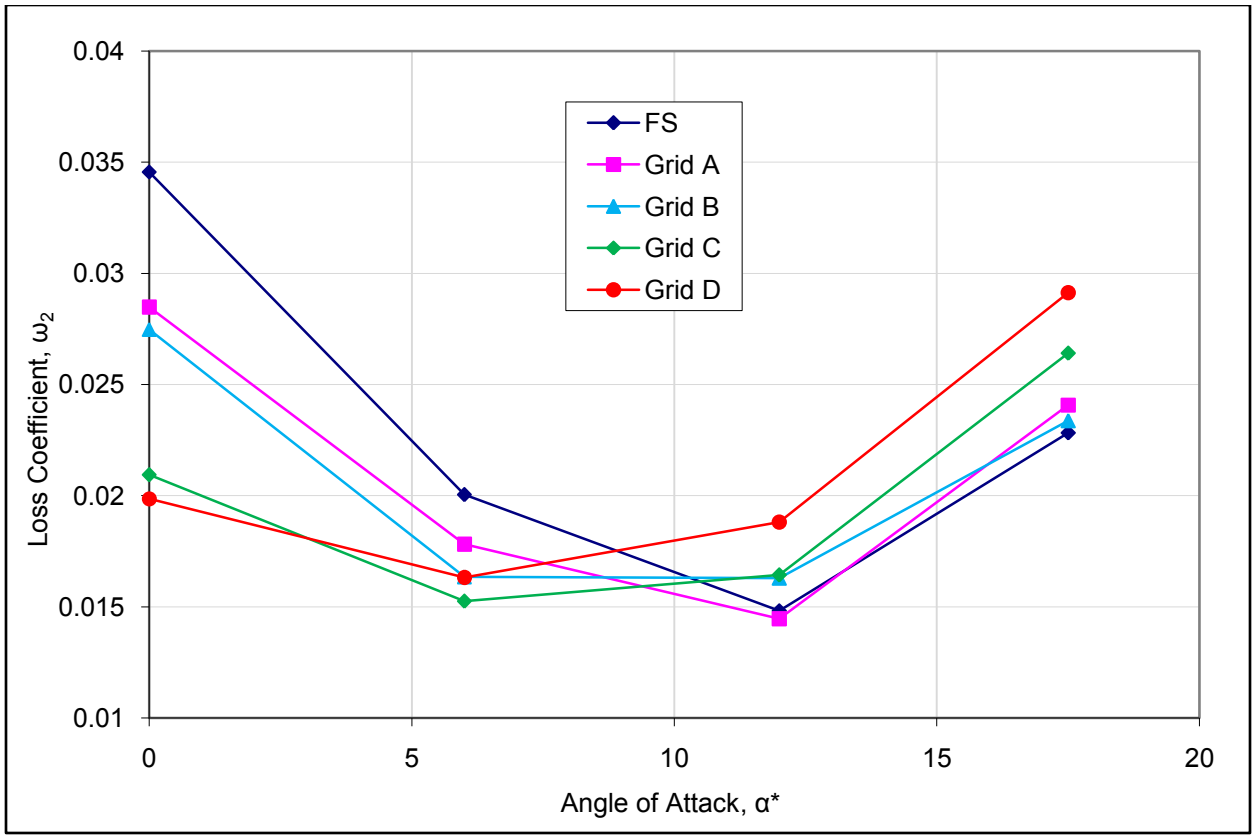

Figure 5.3.4A The loss coefficients at $\xi = 25^{o}$ and Re = 12.5 x 10^4 plotted with angle of attack for the various turbulence levels.

Looking first at the left hand side of Figure 5.3.4A at 0º AOA, it is clear that by increasing turbulence, the overall loss coefficient decreases. On the right hand side, at 17.5° AOA, the effect of turbulence is almost exactly opposite. At this point increasing turbulence has a *decreasing* effect on loss coefficient, which may seem surprising at first. In general, what can be said about the figure as a whole, is that all of the turbulence-influenced loss coefficients come to a minimum in the vicinity of the angle of the zero camber line angle of incidence (AOA = 8°), which is reasonable and expected. Another observation is that by controlling (increasing or decreasing) the level of turbulence at a given angle of attack, a high percentage of losses can be recovered.

In order to explain the apparent role-reversal of turbulence from decreasing to increasing loss coefficient in Figure 5.3.4A, it is important to recall the separation regimes that could have an

influence on the wakes, and therefore their contribution to overall cascade losses, at the different angles of attack. Referring back to Figures 5.3.2A- D, at 0º AOA there was full trailing edge separation which can be viewed as the turbulent energy being expended in reattaching the flow and reducing the wakes and losses. At 6º AOA, the result was very similar, requiring less turbulence for the flow to become fully reattached.

Once past zero angle of incidence, though, the blade flow began to exhibit suction side, leading edge separation. Flow reattachment directly after the leading edge does not benefit much from turbulence in the way of decreased loss coefficient, and at this point increasing turbulence becomes detrimental to performance because of increased free stream losses. This can be explained by noting that at a place where there is no trailing edge separation to beneficially absorb the turbulent energy, turbulence adds momentum to the boundary layer at the trailing edge, causing a larger pressure drop in the wake. Similar results supporting this explanation were obtained for velocity and turbulence by Sullery [24] as shown in Figure 5.3.4B.

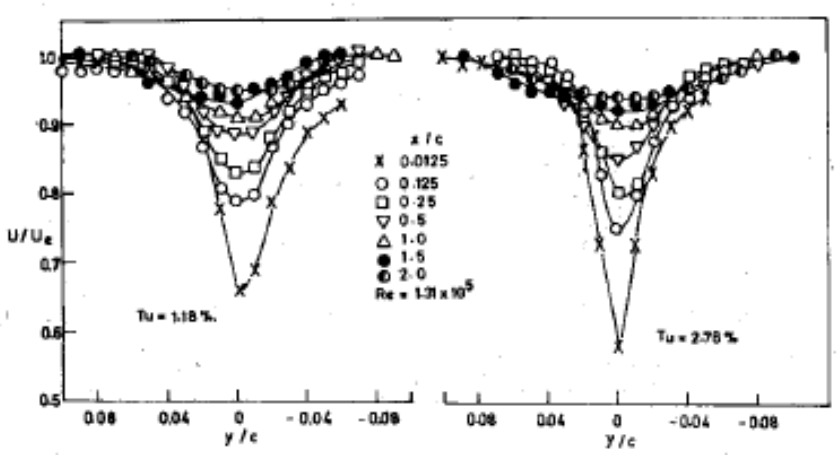

Figure 5.3.4B Sullery's results show that increasing turbulence decreases the velocity for set measurement locations behind a compressor cascade wake. (From [24]; reprinted by permission of the American Institute of Aeronautics and Astronautics, Inc.)

The total pressure loss contributions from the wakes are easily calculated from the data, and are shown visually in Figure 5.3.4C. It is important to note that although these figures show the

pitch location (denoting the spatial width of the wake), they do not show the spatial length of the wake behind the blade. The plots show *loss ratio* in the wake, *not* velocity profiles. The loss ratio shows the drop in total pressure at the single measurement location behind the blade. Thus, without turbulent energy used to benefit separation, the increased momentum in the boundary layer causes a steeper total pressure loss gradient in the wake, across almost the same width.

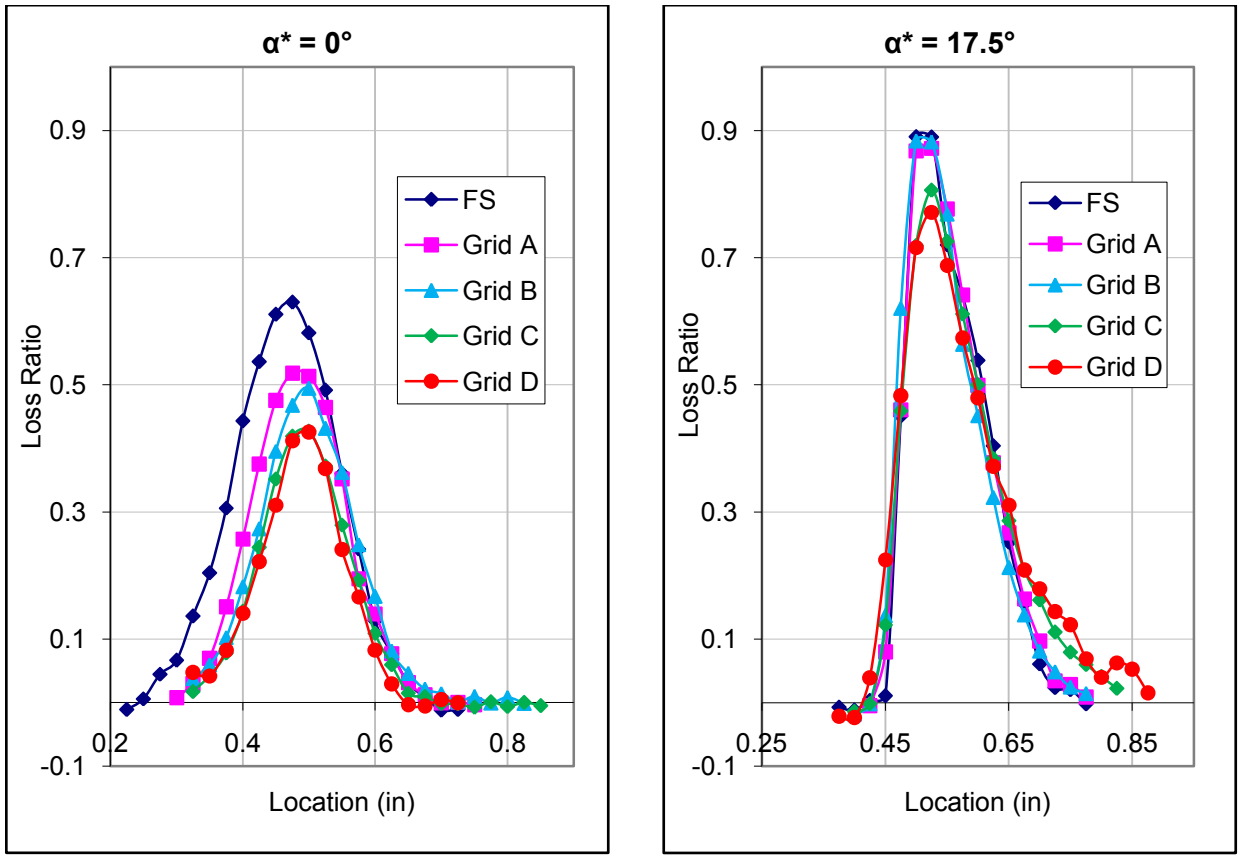

Figure 5.3.4C The loss ratio (total pressure loss in the wake normalized by the free stream total pressure) at two angles of attack for $\xi = 25°$ and $Re = 12.5 \times 10^4$.

Figure 5.3.4D shows that this trend for total pressure losses also exists for the same stagger at $Re = 12.5 \times 10^4$, while the trend is no longer apparent at the lowest Reynolds number of 6×10^4 shown in Figure 5.3.4E.

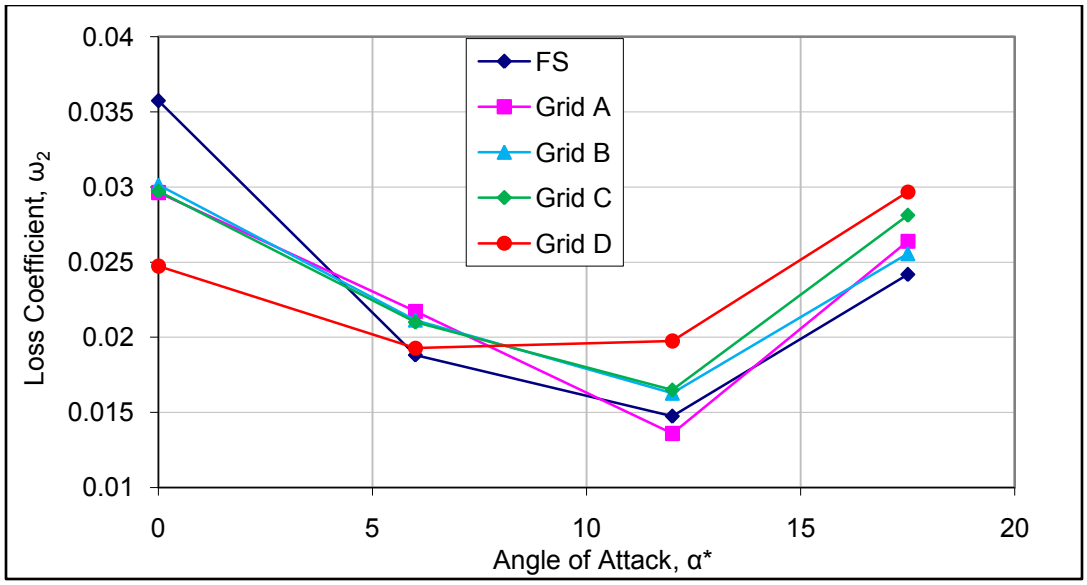

Figure 5.3.4D The loss coefficients at $\xi = 25^{\circ}$ and Re = 9 x 10^4 plotted with angle of attack for the various turbulence levels.

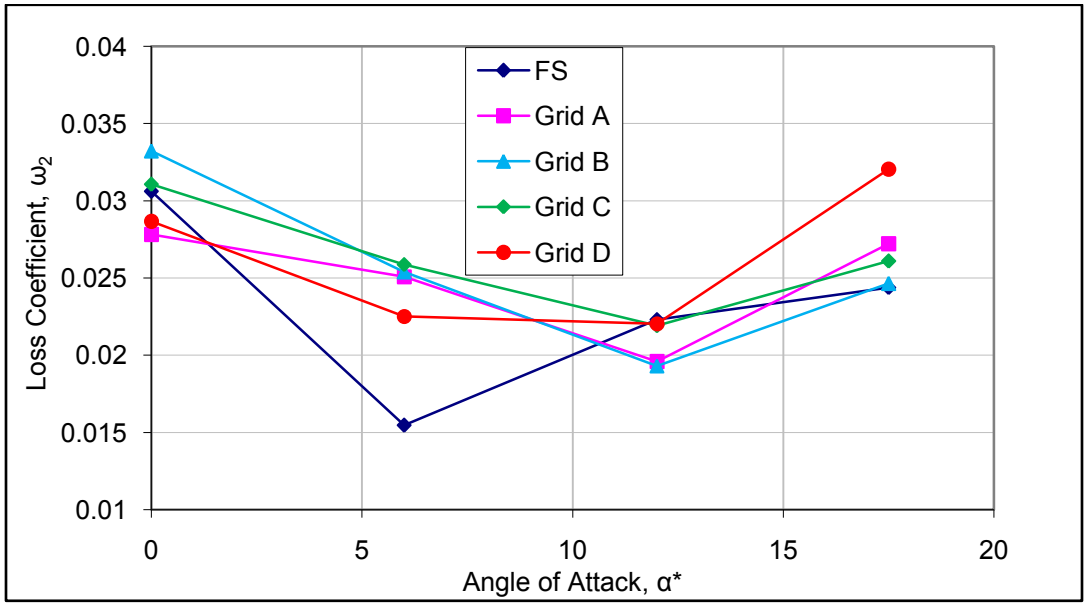

Figure 5.3.4E The loss coefficients at $\xi = 25^{\circ}$ and Re = 6 x 10^4 plotted with angle of attack for the various turbulence levels.

For the stagger angle of 37.5, these same trends by Reynolds number, including the lack of coherence at Re of 6 x 10^4, are apparent. One main difference between the results for the two

settings of stagger is that in general, even though the minimum loss coefficient is about the same, the loss coefficient at lower angles of attack is higher. These are shown in Figures 5.3.4 F-H.

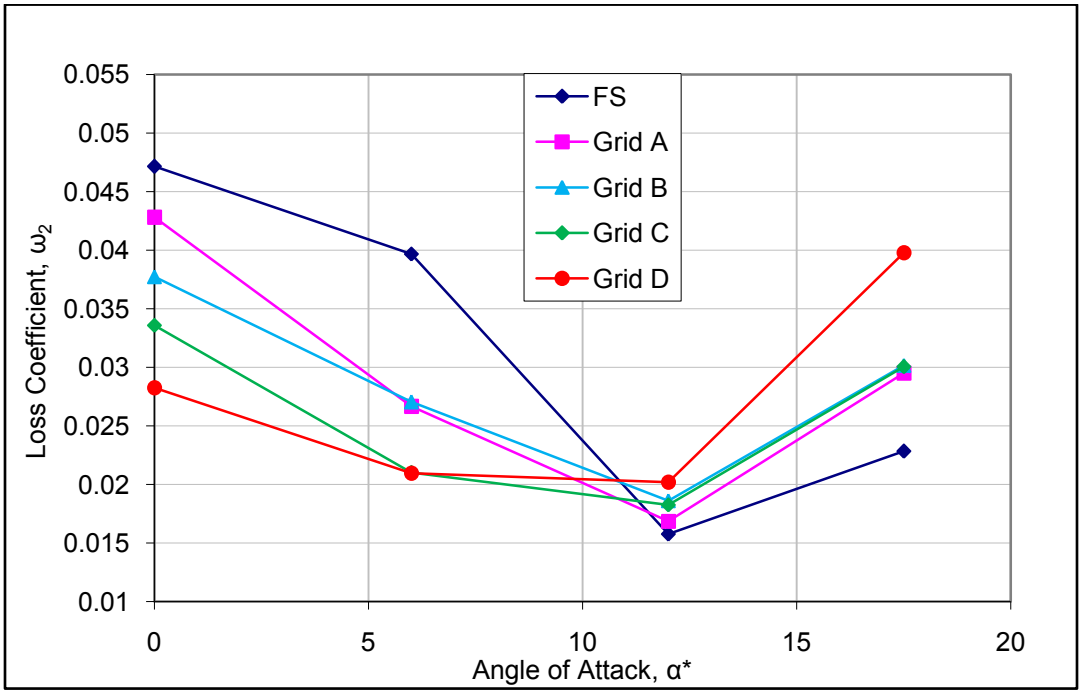

Figure 5.3.4F The loss coefficients at $\xi = 37.5^{o}$ and $Re = 12.5 \times 10^{4}$ plotted with angle of attack for the various turbulence levels.

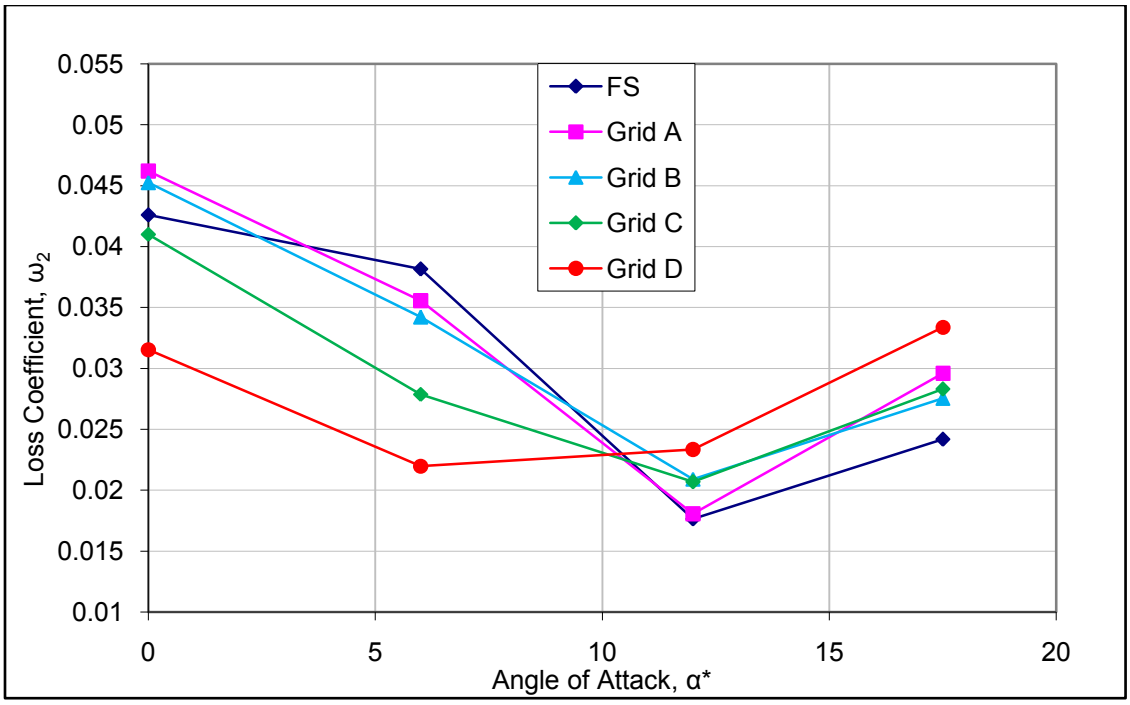

Figure 5.3.4G The loss coefficients at ξ = 37.5º and Re = 9 x 10^4 plotted with angle of attack for the various turbulence levels.

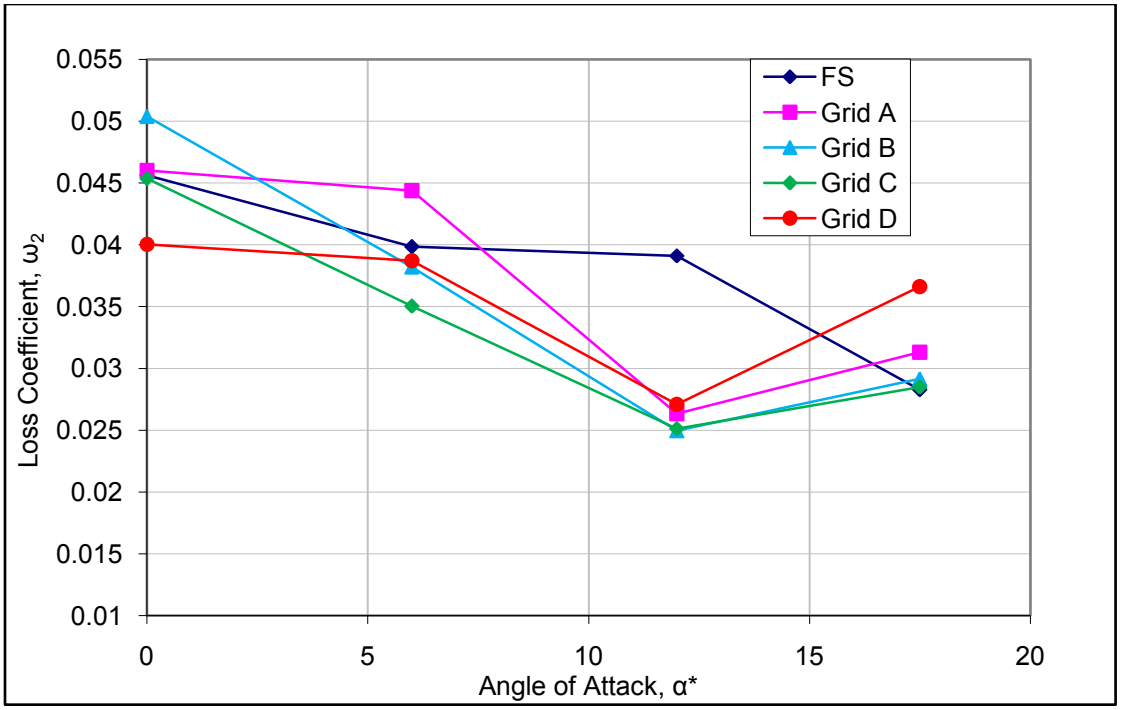

Figure 5.3.4H The loss coefficients at ξ = 37.5 and Re = 6 x 10^4 plotted with angle of attack for the various turbulence levels.

For the Reynolds number of 6 x 10^4, at both settings of stagger, no trends with turbulence variation were noted. The data will thus not be further analyzed in this section for further calculation. It is possible that the trends of turbulence effect on separation extend down to only a certain Reynolds number, where other unknown factors have an influence. For the two staggers and Reynolds numbers that do show a trend, Table 5.3.4 shows how strong the observed effects of turbulence on loss coefficient can be at the tested stagger, Reynolds number, and turbulence levels.

Table 5.3.4 The possible loss coefficient decrease percentages possible through the application of the correct turbulence intensity.

ξ	Re	α*	Min Loss	Max Loss	%
25	125k	0	0.0199	0.0346	42.5
		6	0.0153	0.0200	23.9
		12	0.0145	0.0188	23.1
		17.5	0.0228	0.0291	21.6
	90k	0	0.0247	0.0357	30.8
		6	0.0188	0.0217	13.4
		12	0.0136	0.0197	31.2
		17.5	0.0242	0.0297	18.5
37.5	125k	0	0.0282	0.0471	40.1
		6	0.0209	0.0397	47.2
		12	0.0158	0.0202	21.9
		17.5	0.0228	0.0398	42.6
	90k	0	0.0315	0.0462	31.7
		6	0.0220	0.0382	42.4
		12	0.0176	0.0233	24.4
		17.5	0.0242	0.0334	27.6

For both settings of stagger, Table 5.3.4 shows that at certain angles of attack a decrease in loss coefficient of over forty percent is possible at the low Reynolds numbers studied by actively controlling the correct level of turbulence intensity. For all angles of attack in this study, the possible increase in performance (decrease in overall loss) is over 13%.

Chapter 6

Summary, Conclusions and Recommendations

After reviewing the research done in the turbomachinery industry on the effect of turbulence and Reynolds number on performance of a compressor cascade, this study was performed to fill in gaps in current research both qualitatively and quantitatively. Mainly, it improved upon qualitative investigations of the effects of turbulence on separation at low Reynolds numbers with quantified improvements of loss coefficient. At the same time flow and boundary layer visualization techniques were employed to match the qualitative and quantitative observations.

At low Reynolds numbers, introducing high free stream turbulence can benefit the performance of a compressor cascade by a considerable percentage of reduction of total pressure loss coefficient. The relation between turbulence levels for loss reduction and angle of attack are complex, and explanation required extensive discussion and some speculation. Loss reduction would be ideal for efficiency in operation in the laminar separation regime, and for off design operation as well. But while beneficial relationships were found between different turbulence intensities and low loss coefficients, they did not manifest at the lowest Reynolds number tested. The reason for this result is unclear.

There are many possible avenues to use and expand on this research. The ideal application of this research would be to use controlled turbulence intensities to keep a low total pressure loss coefficient at a widened compressor operating range, and to improve efficiency at off design operation. The methods outlined for obtaining data can be used at any Reynolds number for which turbulence can be used to control separation.

Ideally, more test points are desired to empirically relate intensity to loss coefficient at set values of the other parameters. This would include additional settings of angle of attack and turbulence intensity, keeping in mind that any relations would be highly dependent on airfoil shape because of the highly variable boundary layer behaviors of different airfoils at different Reynolds numbers.

This research should be expanded into the areas of full stall to test the limits of what active control could achieve in the future. Through an expansive parametric investigation varying turbulence intensity, angle of attack, stagger, and Reynolds number, a complete map for active control of separation could possibly be deduced.

References

[1] Russ, Thomas., "A Surface Flow Visualization Study of Boundary Layer Behavior on the Blades of a Solid-Wall Compressor Cascade at High Angles of Attack," M.S. Thesis, Mechanical Engineering, VPI & SU, 1987.

[2] Yocum, Adam, II., "An Experimental and Numerical Investigation of the Performance of Compressor Cascades with Stalled Flow," P.h.D Dissertation, Mechanical Engineering, VPI & SU, 1987.

[3] Roach, P.E. (1987). The Generation of Nearly Isotropic Turbulence by Means of Grids. *International Journal of Heat and Fluid Flow*, *8(2)*, 82-92.

[4] Hinze, J.O. (1975). *Turbulence*. New York: McGraw-Hill.

[5] Carullo, Jeffrey S., "Effects of Free stream Turbulence, Turbulence Length Scale, and Reynolds Number on Turbine Blade Heat Transfer in a Transonic Cascade." M.S. Thesis, Mechanical Engineering, VPI & SU, 2006.

[6] Nix, Andrew Carl., "Effects of High Intensity Large-Scale Free stream Combustor Turbulences on Heat Transfer in Transonic Turbine Blades," P.h.D Dissertation, Mechanical Engineering, VPI & SU, 2003.

[7] Von Kármán, T. (1948). Progress in the Statistical Theory of Turbulence. *Proceedings of the National Academy of Sciences, 34,* 530-539.

[8] Sato, Hiroshi. (1952). Experimental Study of the Spectrum of Isotropic Turbulence, II. *Journal of the Physical Society of Japan, 7 (4)*, 392-396.

[9] Biroak, M., Brahim, S., Iskender, G. (2003) An Attempt to Realize Experimental Isotropic Turbulence at Low Reynolds Numbers. *Flow, Turbulence, and Combustion, 70,* 325-348.

[10] Gamard, S., George, W., (1999) Reynolds Number Dependence of Energy Spectra in the Overlap Region of Isotropic Turbulence. *Flow, Turbulence, and Combustion, 63,* 443-477.

[11] Treaster, A.L., Yocum, A.M., (1979) The Calibration and Application of Five-hole Probes. *ISA Transactions, 18(3),* 23-34.

[12] Bruun, H.H., Khan, M.A., Al-Kayiem, H.H., Fardad, A.A. (1988) Velocity Calibration Relationships for Hot-wire Anemometry. *Journal of Physics E: Scientific Instruments, 21*, 225-232.

[13] Carneal, James P., "Experimental Investigation of Reversed Flow in a Compressor Cascade," Masters Thesis, Mechanical Engineering, VPI & SU, 1990.

[14] Ainslie, Walter E., "The Effect of Solidity on the Pre- and Post-Stall Flow in a Linear Compressor Cascade," Masters Thesis, Mechanical Engineering, VPI & SU, 1988.

[15] Douglas, Justin W. "Effects of Free Stream Turbulence on Compressor Cascade Performance." Masters Thesis, Mechanical Engineering, VPI & SU, 2001.

[16] Evans, Bernard J. "Effects of Free-Stream Turbulence on Blade Performance in a Compressor Cascade." P.h.D Dissertation, Department of Engineering, University of Cambridge, 1971.

[17] Yocum, A.M., O'Brien, W.F. (1993) Separated Flow in a Low-Speed Two-Dimensional Cascade: Part I – Flow Visualization and Time-Mean Velocity Measurements. *Journal of Turbomachinery, 115*, 409-420.

[18] Hill, Philip, Peterson, Carl (1992). *Mechanics and Thermodynamics of Propulsion*. New York: Addison-Wesley.

[19] Rhoden, H.G (1952) Effects of Reynolds Number on Flow of Air through a Cascade of Compressor Blades. *Aeronautical Research Council Reports and Memoranda,*. No. 2919

[20] Roberts, W.B. (1975) The Effect of Reynolds Number and Laminar Separation on Axial Cascade Performance. *Transactions of the ASME: Journal of Engineering for Power, 97(A,2)*. 261-274.

[21] Evans, R.L. (1984) The Effect of Freestream Turbulence on the Profile Boundary Layer and Losses in a Compressor Cascade. *American Society of Mechanical Engineers Gas Turbine Power Division, 1984-GT-242.*

[22] Shaw, R. (1969) The Effect of Reynolds Number, Turbulence Intensity, and Axial Velocity Ration on Compressor Blade Performance. *Proceedings of the Institution of Mechanical Engineers, 184(Pt 3G II),* 93-100.

[23] Citavy, J. Norbury, J.F. (1977) The Effect of Reynolds Number and Turbulence Intensity on the Performance of a Compressor Cascade with Prescribed Velocity Distribution. *Journal of Mechanical Engineering Science, 19(3),* 93-100.

[24] Sullerey, R.K. Sayeed Khan, M.A. (1983) Freestream Turbulence Effects on Compressor Cascade Wake. *Journal of Aircraft, 20(8),* 733-734. (Figure 5.3.4.B reprinted by permission of the American Institute of Aeronautics and Astronautics, Inc.)

[25] Schreiber, H.A. Steinert, W. (2002) Effects of Reynolds Number and Free-Stream Turbulence on Boundary Layer Transition in a Compressor Cascade. *Transactions of the ASME - Journal of Turbomachinery,124,* 1-9.

[26] Gostelow, J.P. (1984). *Cascade Aerodynamics*. New York: Pergamon Press.

[27] Schlichting, H. (1979). *Boundary-Layer Theory*. New York: McGraw-Hill, Inc.

[28] Figliola, R.S. Beasley, D.E. (2006). *Theory and Design for Mechanical Measurements*. Hoboken: John Wiley & Sons, Inc.

[29] Jonas, P., Mazor, V. Uruba, V. (1996) On the Boundary Layer Transition Flows with Various Length Scales. *Advances in Turbulence VI, 36,* 345-346.

Appendix

A.1. Error Analysis

The following is an analysis in which estimates of the uncertainty of the major parameters and important measurements are made. The adjustable independent variables in this study were the angle of attack, α*, stagger, ξ, Reynolds number, Re, and Turbulence intensity, *Tu*. While the cascade angles could be determined directly, the Reynolds number and Turbulence intensity were subject to instrument uncertainty and error propagation, as was the total pressure loss coefficient $\overline{\omega_2}$. For these, the root sum squares (RSS) and sensitivity index methods outlined by Figliola and Beasley and used by Yocum and Ainslie will be utilized [2] [14] [28]. After an example shown in section A.4, only the results will be presented for brevity.

A.1 Angle of Attack, Stagger

The rotatable Plexiglas circular sides of the test section, with which the angles of attack and stagger could be set, were incremented to 0.5°. From the Figliola and Beasley determination of zero order uncertainty, these angular measurements can be accurately set to within half of the measurement resolution, or ± 0.25° [28].

A.2 DAQ Uncertainty

All measurements, except when using the point detector for calibration of the pressure transducers, were made electronically through a National Instruments DAQCard-6062E PCMCIA card. The analog inputs, according to the National Instruments specification sheet, have an absolute accuracy of ± 17.945 mV. This uncertainty factors into all measurements, and can be converted into an uncertainty in pressure with each transducer's calibration curve as shown in Table A.2.

Table A.2. Uncertainties in pressure measurements due to DAQ uncertainty.

Transducer	Accuracy
2.5"	±0.00886"
0.5"	±0.00180"
0.1"	±0.000377"

For the case of the voltages measured by the hotwire, the uncertainty of the DAQ card can be combined in terms of voltage.

A.3 Pressure Transducer Uncertainty

The accuracies of the pressure transducers were found from repeated testing to fall within the manufacturer's certified calibration specification, which was ±0.25% of full scale (FS). The three ranges used were 2.5" H_20, 0.5" H_20, and 0.1" H_20. These accuracies are shown from the specification sheets to account for errors due to non-linearity, hysteresis, non-repeatability, and thermal effects. Thus the accuracies (in the measurement units of inches of water) are listed in Table A.3 with the full scale range of each transducer, the accuracy of the transducer, and the combined uncertainty from both the DAQ and pressure transducer combined.

Table A.3. Uncertainties in pressure transducers, in inches of water.

Full Scale	Transducer Accuracy	Total Uncertainty
2.5"	±0.00625"	±0.0108"
0.5"	±0.00125"	±0.00219"
0.1"	±0.00025"	±0.00045"

A.4 Static Tap Measurement Uncertainty

The formula used to compute the blade static pressure coefficients in chapter 2 is

$$C_{p\,s,blade} = \frac{P_{s_1} - P_{s_b}}{P_{t_1} - P_{s_1}} \tag{2.4}$$

with all parameters previously defined. Thus, there are three pressure measurements affected by both the DAQ and pressure transducer uncertainties. The uncertainty of the result predicted by the equation is then determined by

$$U_{Cp\ s,blade} = \left[\left(\frac{\partial C_{p\ s,blade}}{\partial P_{s_1}} U_{P_{s_1}}\right)^2 + \left(\frac{\partial C_{p\ s,blade}}{\partial P_{s_b}} U_{P_{s_b}}\right)^2 + \left(\frac{\partial C_{p\ s,blade}}{\partial P_{t_1}} U_{P_{t_1}}\right)^2\right]^{\frac{1}{2}} \quad \text{(A.4.1)}$$

where

$$\frac{\partial C_{p\ s,blade}}{\partial P_{s_b}} = \frac{-1}{P_{t_1} - P_{s_1}} \quad \text{(A.4.2)}$$

$$\frac{\partial C_{p\ s,blade}}{\partial P_{s_1}} = \frac{P_{t_1} - P_{s_b}}{\left(P_{t_1} - P_{s_1}\right)^2} \quad \text{(A.4.3)}$$

$$\frac{\partial C_{p\ s,blade}}{\partial P_{t_1}} = \frac{-\left(P_{s_1} - P_{s_b}\right)}{\left(P_{t_1} - P_{s_1}\right)^2} \quad \text{(A.4.4)}$$

Depending on the Reynolds number of the specific test, either the 2.5" H_20 pressure transducer (Re = 125k, 90k) or 0.5" H_20 pressure transducer (Re = 60k) was used to find all upstream pressures and blade static pressure. While measurements for both Re = 125k and Re = 90k used a common transducer, their uncertainties are different because of their nominal operating points. Using Re = 125k as an example, the uncertainty is found by inserting nominal values such as

P_{t_1} = 2.309" H_20

P_{s_1}= 0.123" H_20

P_{s_b} = 0.968" H_20

into Equations A.4.2 through A.4.4 to solve the partial derivatives as

$$\frac{\partial C_{p\,s,blade}}{\partial P_{s_b}} = \frac{-1}{P_{t_1} - P_{s_1}} = \frac{-1}{2.309"\ H_20 - (0.123"\ H_20)} = -0.457"\ H_20^{-1}$$

$$\frac{\partial C_{p\,s,blade}}{\partial P_{s_1}} = \frac{P_{t_1} - P_{s_b}}{\left(P_{t_1} - P_{s_1}\right)^2} = \frac{2.309"\ H_20 - (0.968"\ H_20)}{(2.309"\ H_20 - (0.123"\ H_20))^2} = 0.281"\ H_20^{-1}$$

$$\frac{\partial C_{p\,s,blade}}{\partial P_{t_1}} = \frac{-\left(P_{s_1} - P_{s_b}\right)}{\left(P_{t_1} - P_{s_1}\right)^2} = \frac{-[(0.123"\ H_20) - (0.968"\ H_20)]}{(2.309"\ H_20 - (0.123"\ H_20))^2} = 0.177"\ H_20^{-1}$$

Then from A.4.1, the uncertainty is

$$U_{Cp\,s,blade} = [[(-0.457"\ H_2O^{-1})(.0108"\ H_2O)]^2 + [(.281"\ H_2O^{-1})(.0108"\ H_2O)]^2 + [(.177"\ H_2O^{-1})(.0108"\ H_2O)]^2]^{\frac{1}{2}} = \pm 0.00610$$

As mentioned, since the nominal values of upstream total, static, and blade static pressures vary, each Reynolds number will have a separate uncertainty, as listed in Table A.4

Table A.4. Uncertainties in blade static pressure coefficient by Reynolds number.

Reynolds number	$C_{p\,s,blade}$ Uncertainty
125k	± 0.00610
90k	± 0.0175
60k	± 0.00884

A.5 Velocity Uncertainty

The pressure transducers were differential units, thus when used with a pitot tube to transduce velocity, the errors were reduced by measuring the differential rather than measuring the total and static pressures individually and calculating the dynamic pressure. Still, the error propagates into the velocity measurements.

Using nominal values for the operating points at different Reynolds numbers as before, and with Bernoulli's equation rearranged to find velocity,

$$V = (\frac{2}{\rho} P_d)^{\frac{1}{2}} \tag{A.5.1}$$

this equation is used with the RSS method to find the uncertainty of the velocity by

$$U_V = \left[\left(\frac{\partial V}{\partial \rho} U_\rho \right)^2 + \left(\frac{\partial V}{\partial P_d} U_{P_d} \right)^2 \right]^{\frac{1}{2}} \tag{A.5.2}$$

The uncertainties of the velocities could be found for the different transducers, and are summarized in Table A.5

Table A.5. Uncertainties in velocity by Reynolds number.

Reynolds number	Velocity Uncertainty (m/s)
125k	± 0.075
90k	$\pm .1045$
60k	± 0.0325

A.6 Loss Coefficient Uncertainty

The total pressure coefficient was described in Chapter Two as

$$C_{p\,total}(s) = \frac{P_{t_1} - P_{t_2}}{P_{t_1} - P_{s_1}} \tag{2.2}$$

The uncertainty in the loss coefficient based on propagation of errors through the pressure measurements was also derived using the RSS method,

$$U_\omega = \left[\left(U_{P_{t_1}} \right)^2 + \left(U_{P_{t_2}} \right)^2 + \left(U_{P_{t_1} - P_{s_1}} \right)^2 \right]^{\frac{1}{2}} \tag{A.6.1}$$

and the results based on Reynolds number from the nominal operating points is summarized in Table A.6.

Table A.6. Uncertainties in loss coefficient by Reynolds number.

Reynolds number	Loss Coefficient Uncertainty
125k	± 0.00697
90k	$\pm .0127$
60k	± 0.00635

A.7 Turbulence Intensity Uncertainty

The turbulence intensity was found from velocity measurements, which were calculated from a calibration curve against pressure derived velocities. There is uncertainty in the pressure derived velocities composing one axis of the calibration curve due to uncertainties in the DAQ card and pressure transducers, calculated in Equation A.7.1 and previously tabulated in Table A.5.

$$U_{cal.velocity} = \left[\left(U_{DAQ}\right)^2 + \left(U_{P.Transducer}\right)^2\right]^{\frac{1}{2}} \tag{A.7.1}$$

There is also error associated with the data deviation from the curve fit converting voltage to velocity for the hotwire, found statistically from the fourth order curve fit to be no greater than $U_{cal.dev.} = \pm .072$ m/s. These uncertainties combine to become

$$U_{Turb\ Vel} = \left[\left(U_{cal.velocity}\right)^2 + \left(U_{cal.dev.}\right)^2\right]^{\frac{1}{2}} \tag{A.7.2}$$

and knowing that both the mean and fluctuating components of velocity from

$$Tu = 100 \cdot \frac{u'}{u_{mean}} \tag{3.6}$$

are within these uncertainties, the RSS method can again be used to propagate the velocity uncertainty through equation 3.6. The uncertainties of the turbulence were broken down by Reynolds number based on nominal operating conditions, shown in Table A.7.

Table A.7. Uncertainties in turbulence intensity by Reynolds number.

Reynolds number	Turbulence Intensity Uncertainty (%)
125k	± 0.48
90k	$\pm .591$
60k	± 0.88

B. Turbulent Effect on Separation Graphs

This appendix contains the blade static tap data for all cases of the investigation. Each graph shows the effect of turbulence at a specific setting of stagger, angle of attack, and Reynolds number. Table B.1. shows the organization of this appendix.

Table B.1 Figure references for static tap data.

Stagger	AOA	Re	Figure
25	0	125k	B.1
		90k	B.2
		60k	B.3
	6	125k	B.4
		90k	B.5
		60k	B.6
	12	125k	B.7
		90k	B.8
		60k	B.9
	17.5	125k	B.10
		90k	B.11
		60k	B.12
37.5	0	125k	B.13
		90k	B.14
		60k	B.15
	6	125k	B.16
		90k	B.17
		60k	B.18
	12	125k	B.19
		90k	B.20
		60k	B.21
	17.5	125k	B.22
		90k	B.23
		60k	B.24

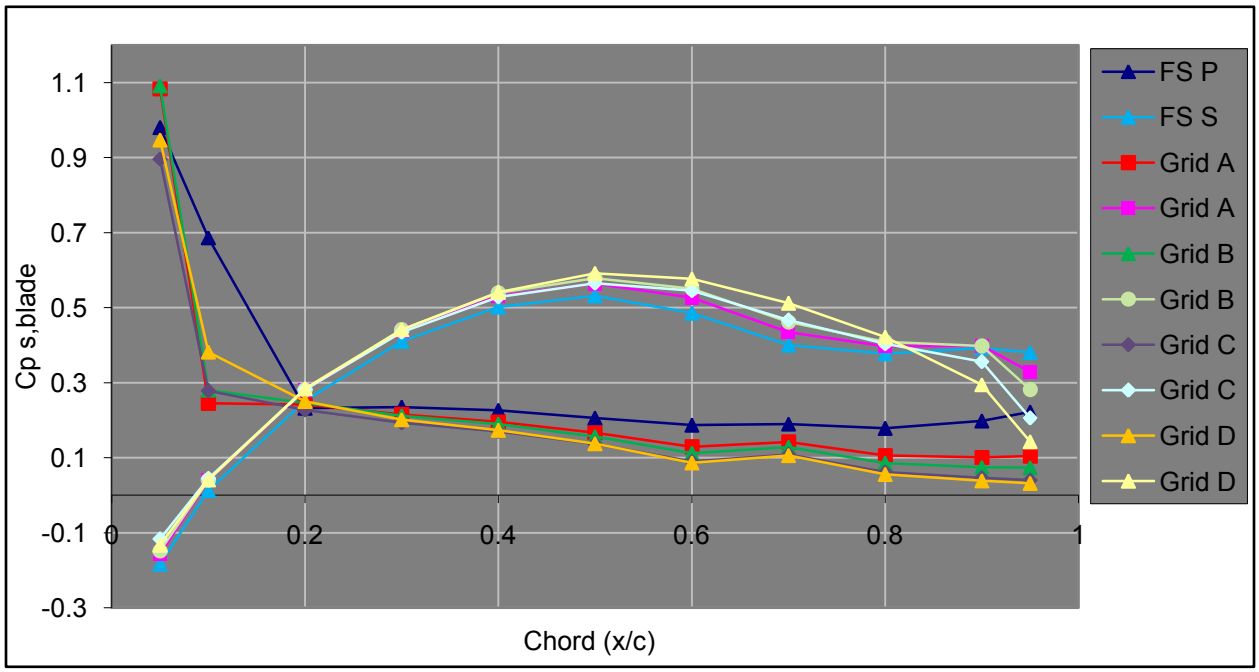

Figure B.1 Static tap graphs for $\xi = 25°$, $\alpha^* = 0°$, $Re = 12.5 \times 10^4$, for all turbulence levels.

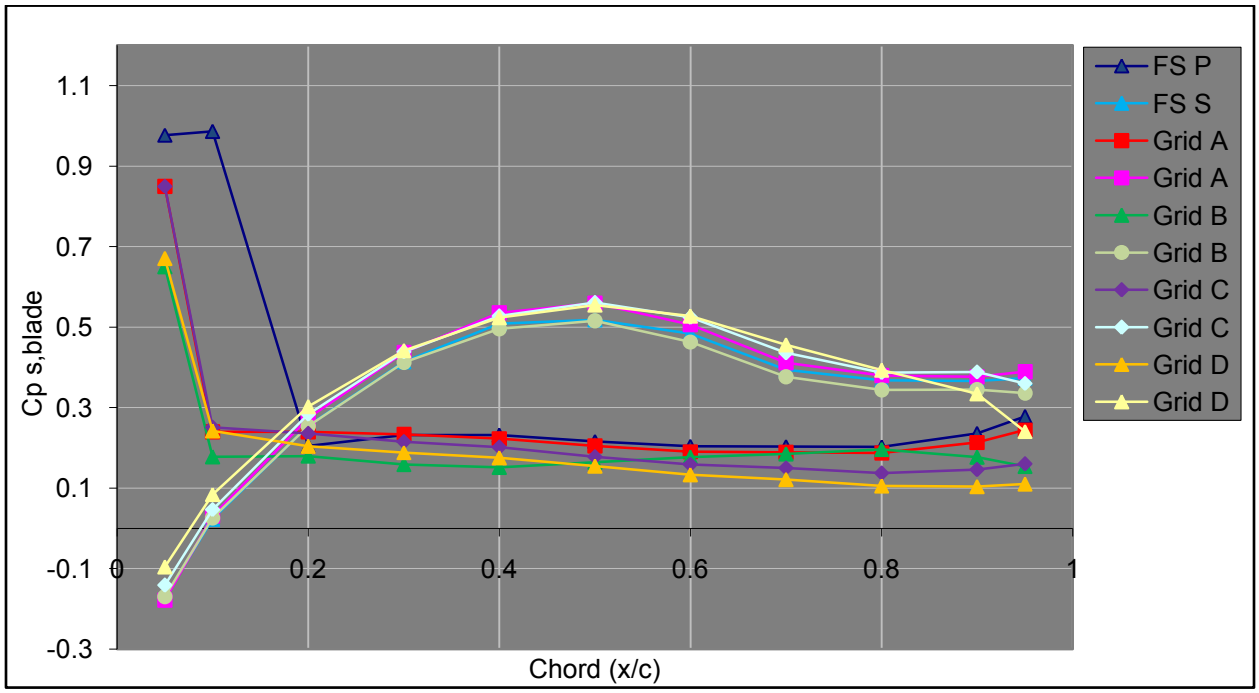

Figure B.2 Static tap graphs for $\xi = 25°$, $\alpha^* = 0°$, $Re = 9 \times 10^4$, for all turbulence levels.

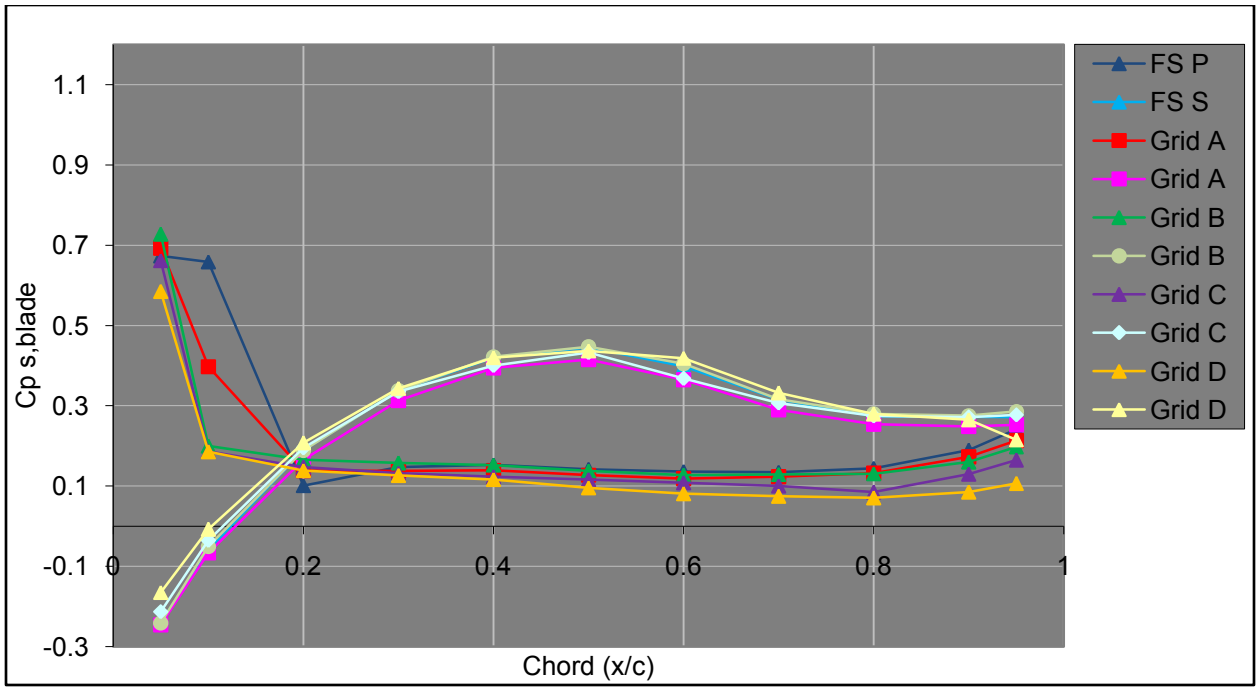

Figure B.3 Static tap graphs for $\xi = 25°$, $\alpha^* = 0°$, $Re = 6 \times 10^4$, for all turbulence levels.

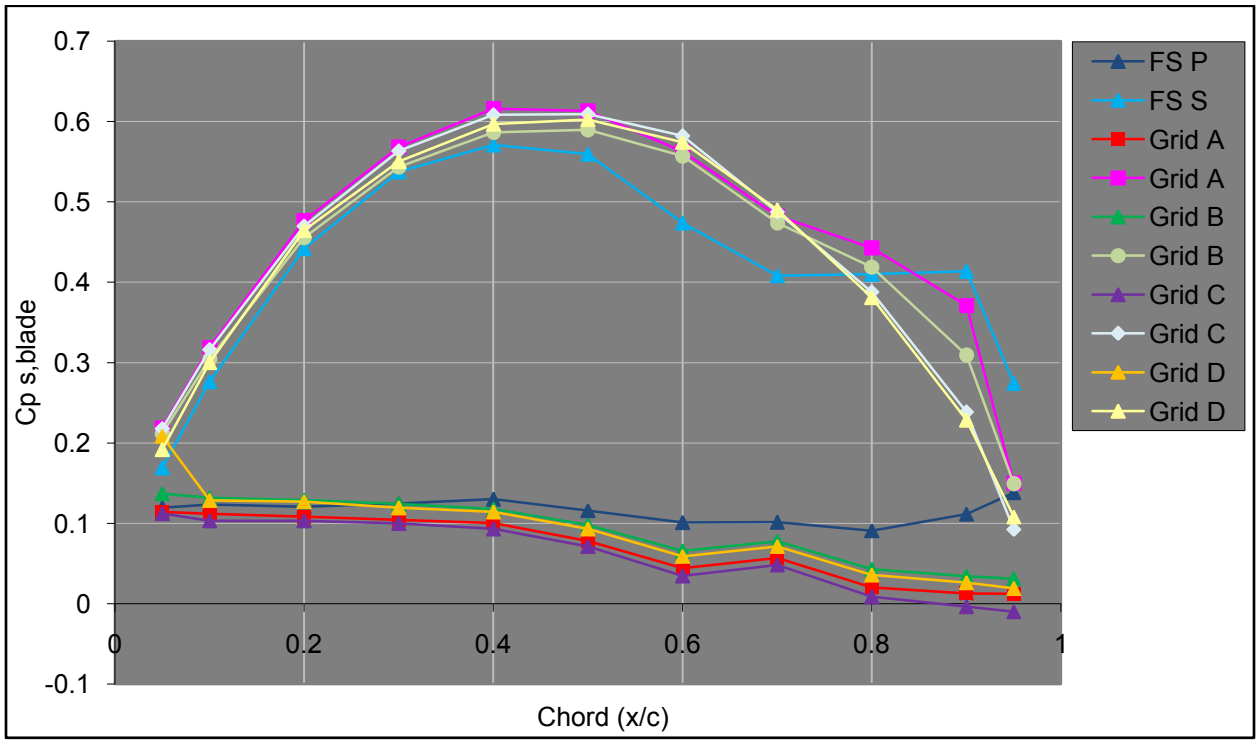

Figure B.4 Static tap graphs for $\xi = 25°$, $\alpha^* = 6°$, $Re = 12.5 \times 10^4$, for all turbulence levels.

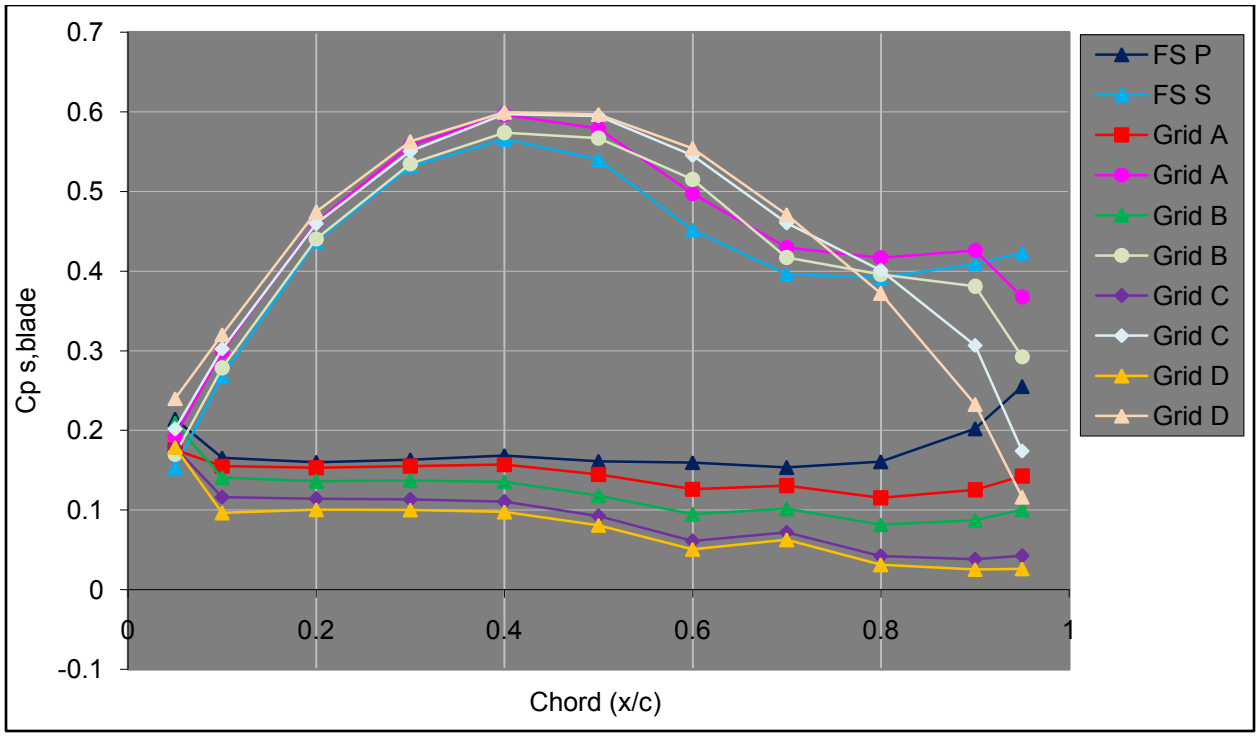

Figure B.5 Static tap graphs for $\xi = 25°$, $\alpha^* = 6°$, Re = 9 x 10^4, for all turbulence levels.

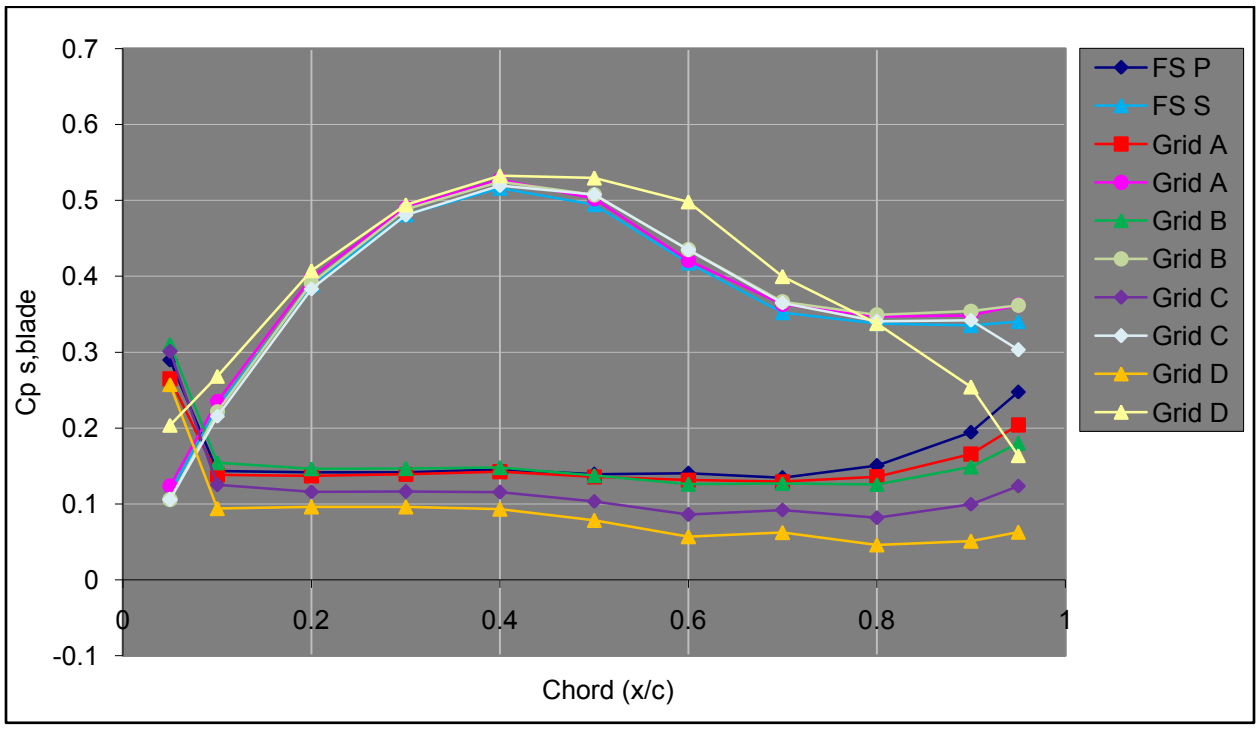

Figure B.6 Static tap graphs for $\xi = 25°$, $\alpha^* = 6°$, Re = 6 x 10^4, for all turbulence levels.

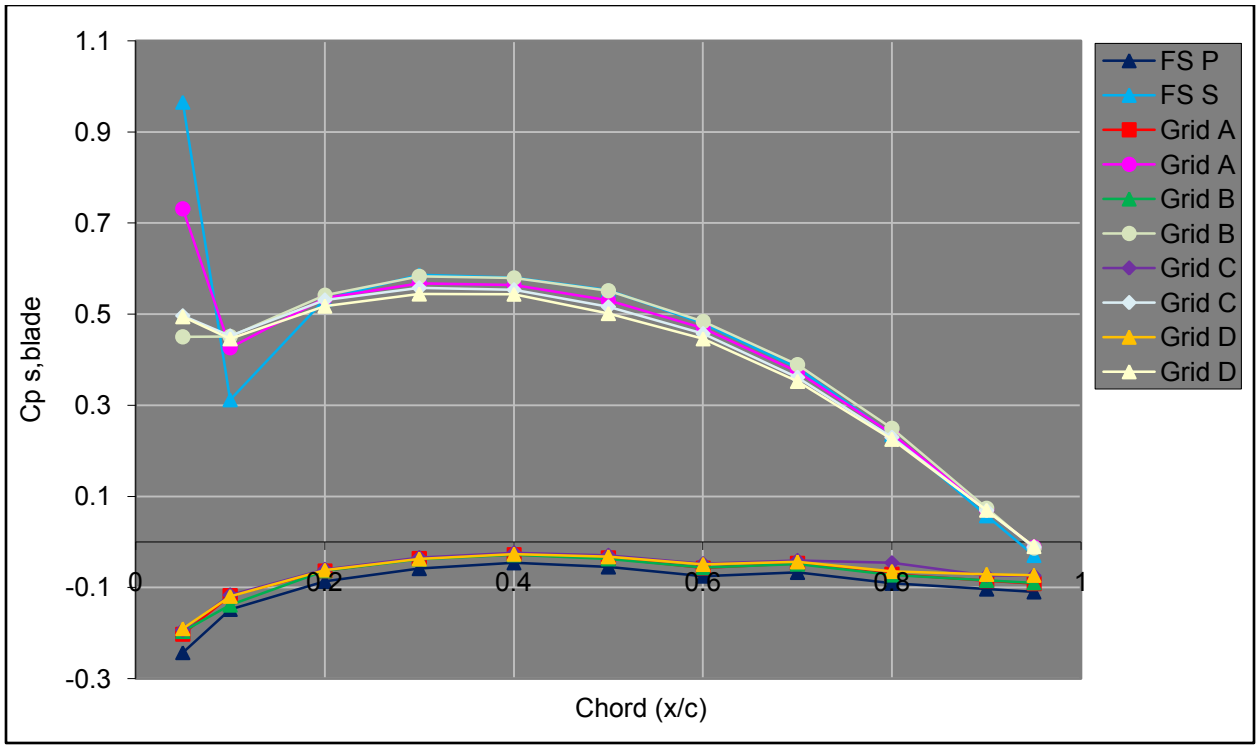

Figure B.7 Static tap graphs for $\xi = 25°$, $\alpha^* = 12°$, $Re = 12.5 \times 10^4$, for all turbulence levels.

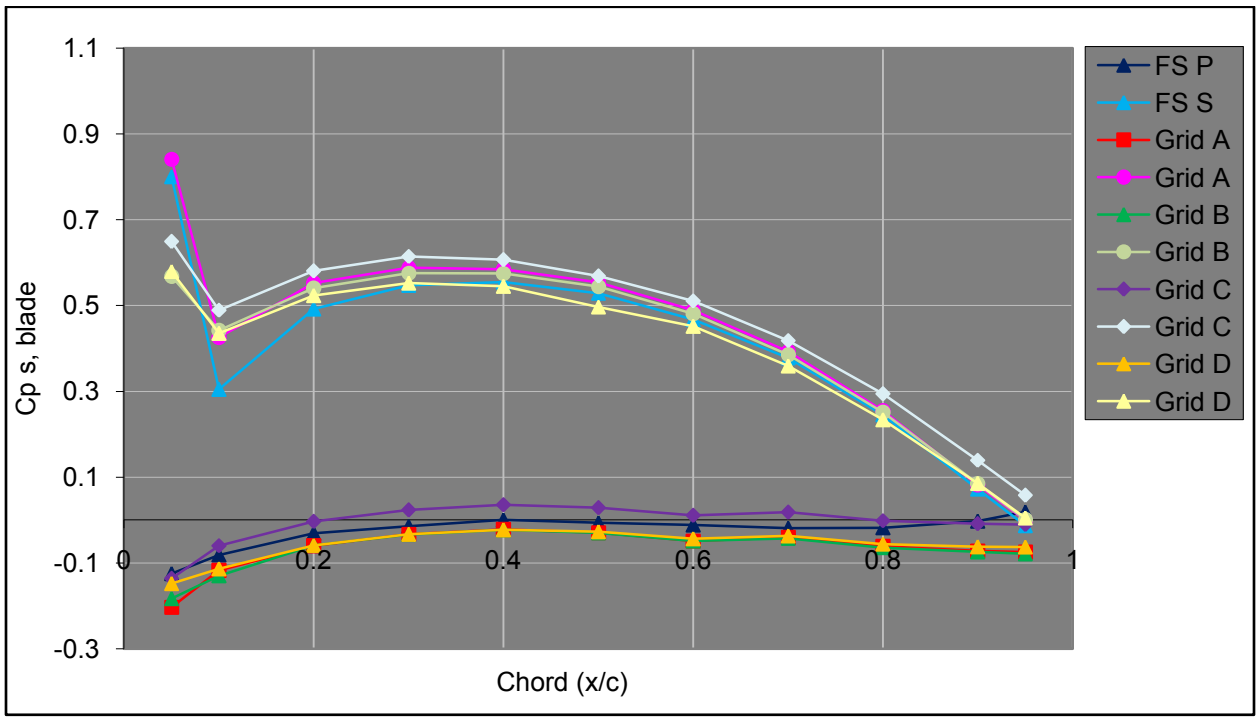

Figure B.8 Static tap graphs for $\xi = 25°$, $\alpha^* = 12°$, $Re = 9 \times 10^4$, for all turbulence levels.

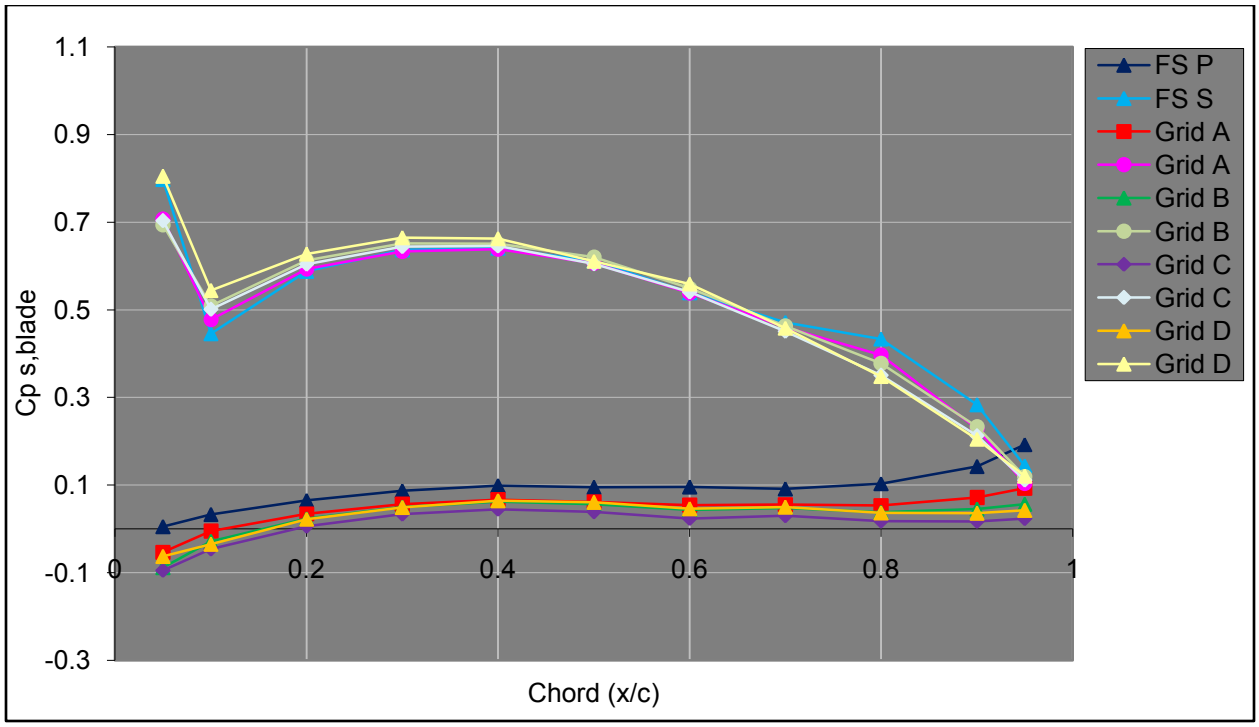

Figure B.9 Static tap graphs for $\xi = 25°$, $\alpha^* = 12°$, $Re = 6 \times 10^4$, for all turbulence levels.

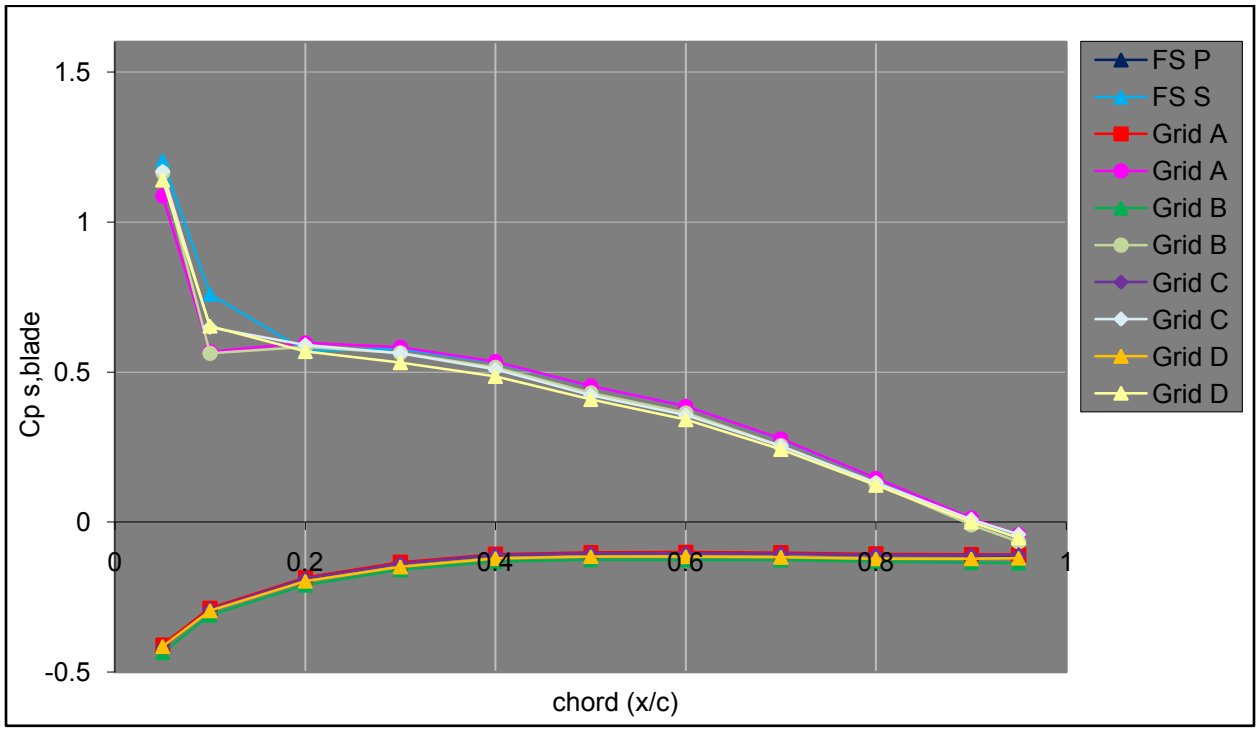

Figure B.10 Static tap graphs for $\xi = 25°$, $\alpha^* = 17.5°$, $Re = 12.5 \times 10^4$, for all turbulence levels.

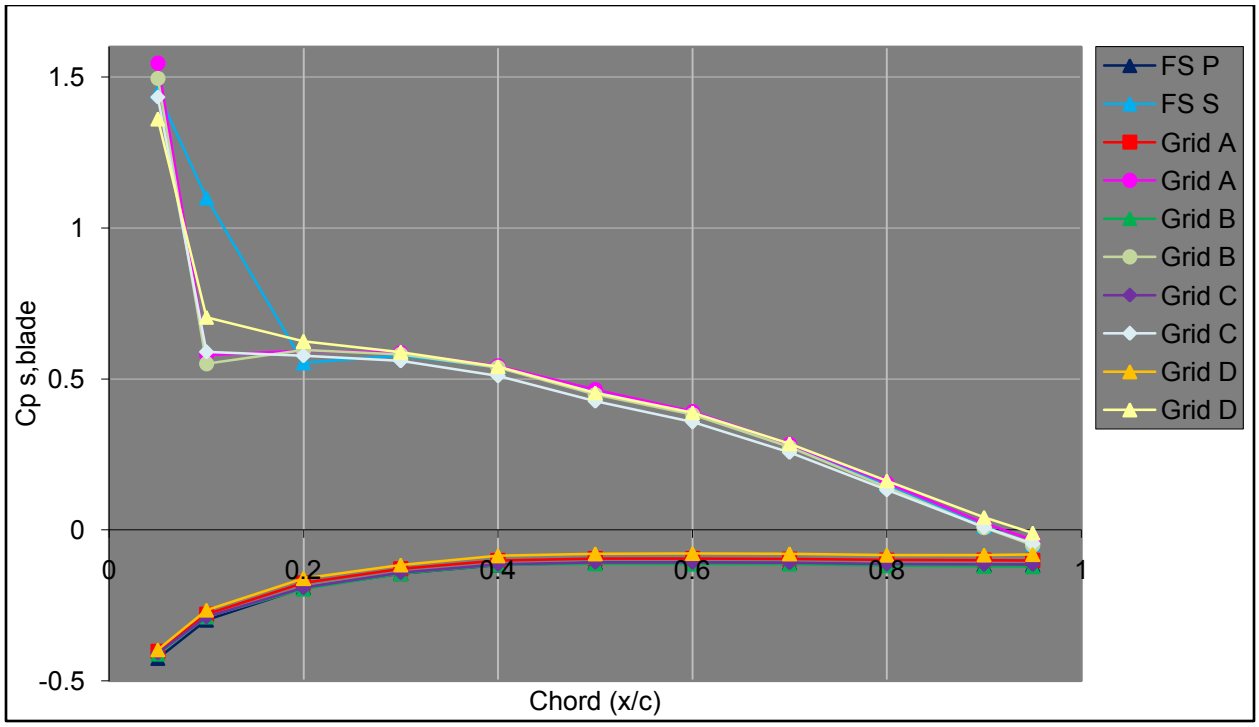

Figure B.11 Static tap graphs for $\xi = 25º$, $\alpha^* = 17.5°$, $Re = 9 \times 10^4$, for all turbulence levels.

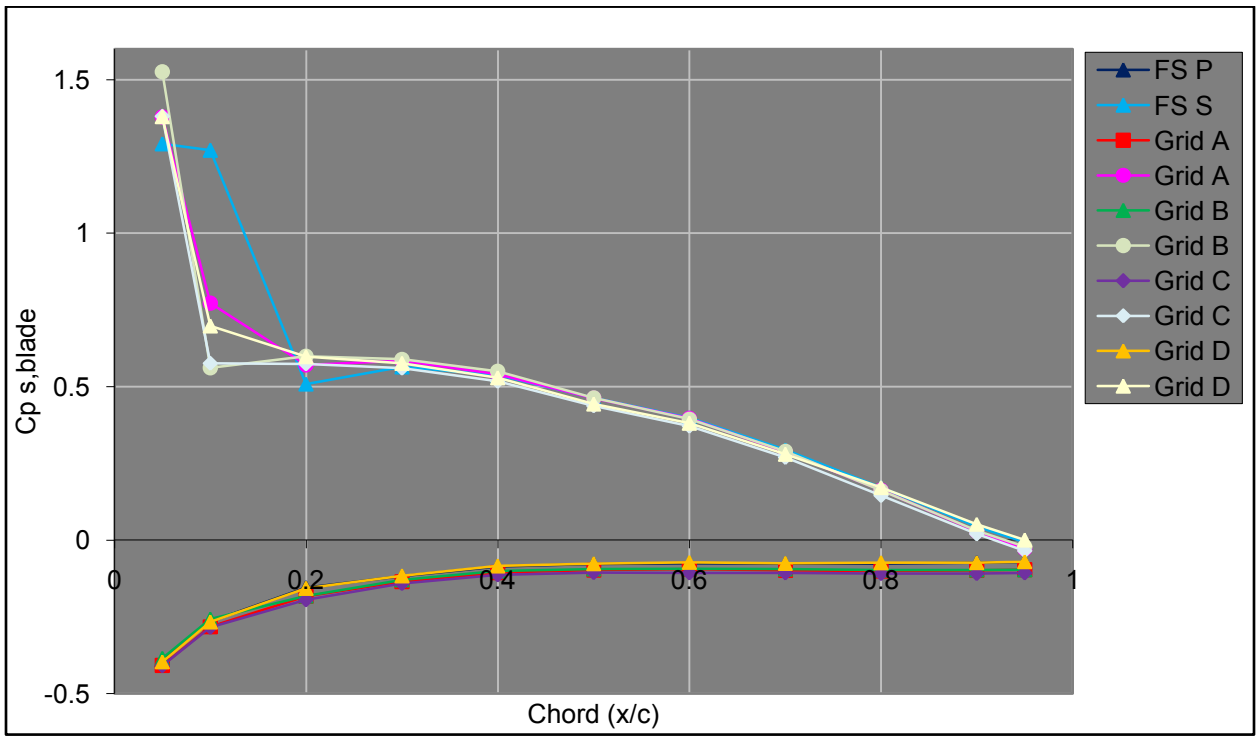

Figure B.12 Static tap graphs for $\xi = 25º$, $\alpha^* = 17.5°$, $Re = 6 \times 10^4$, for all turbulence levels.

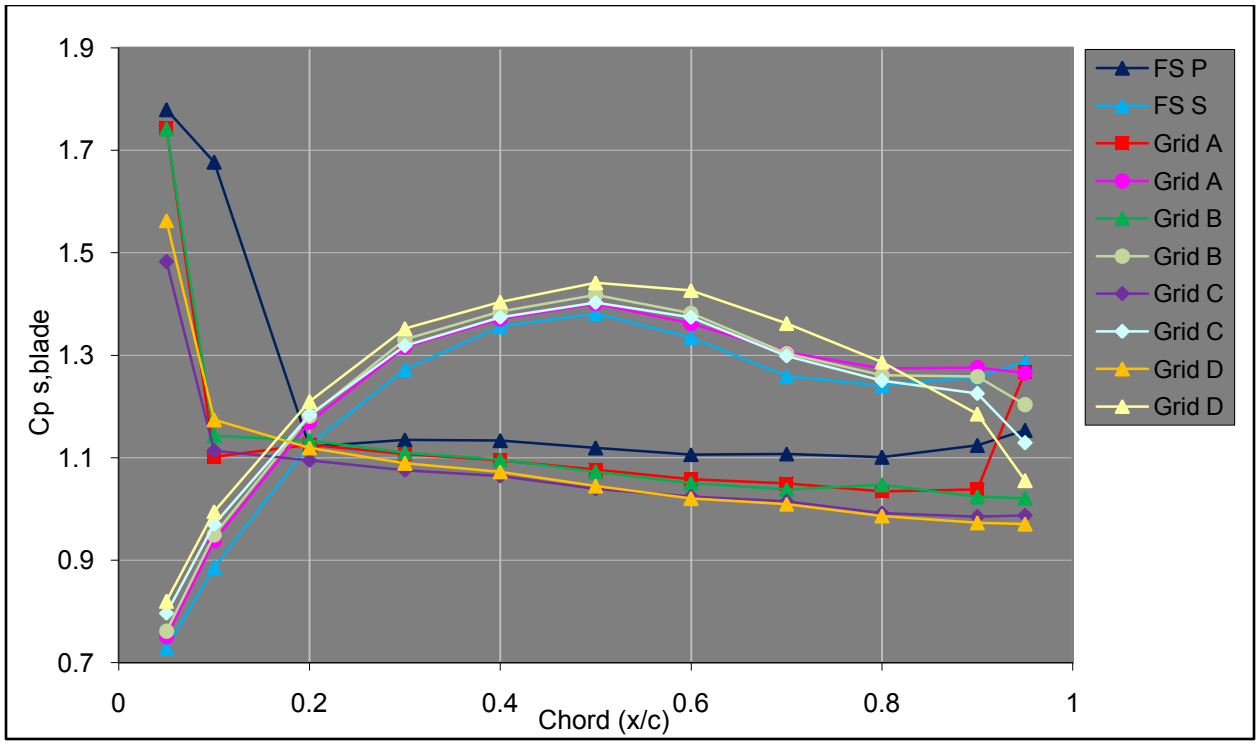

Figure B.13 Static tap graphs for $\xi = 37.5°$, $\alpha^* = 0°$, Re = 12.5 x 10^4, for all turbulence levels.

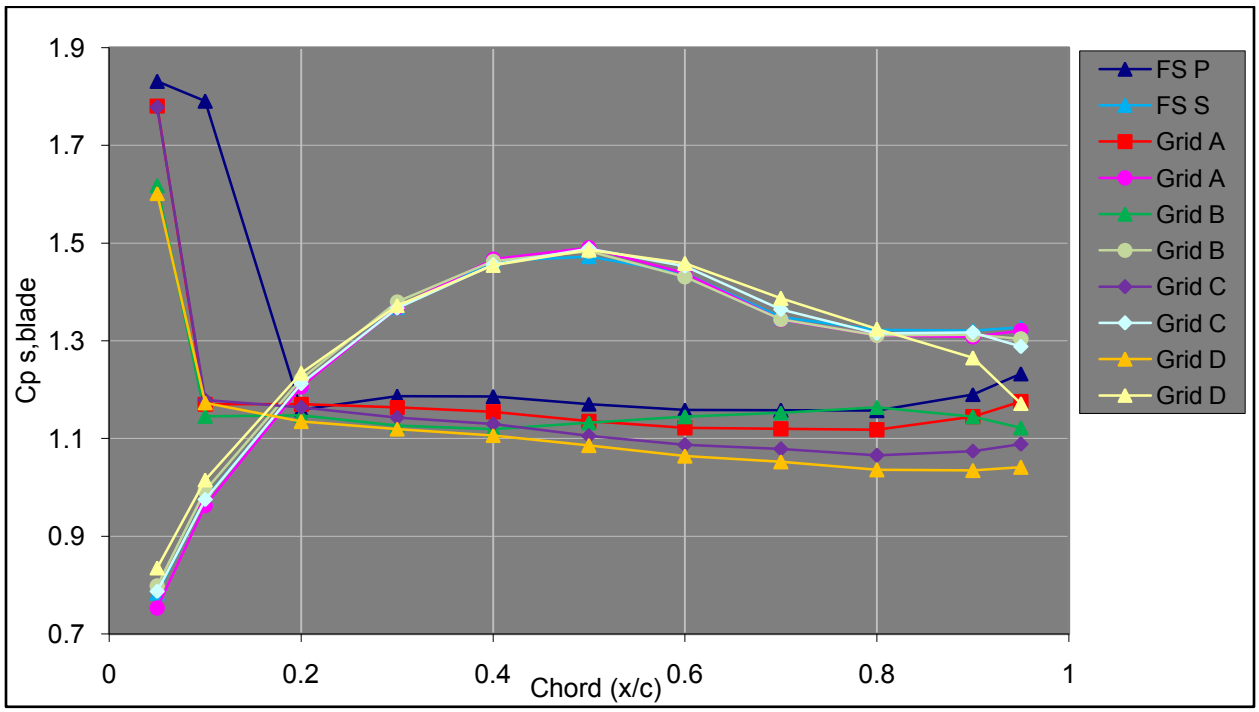

Figure B.14 Static tap graphs for $\xi = 37.5°$, $\alpha^* = 0°$, Re = 9 x 10^4, for all turbulence levels.

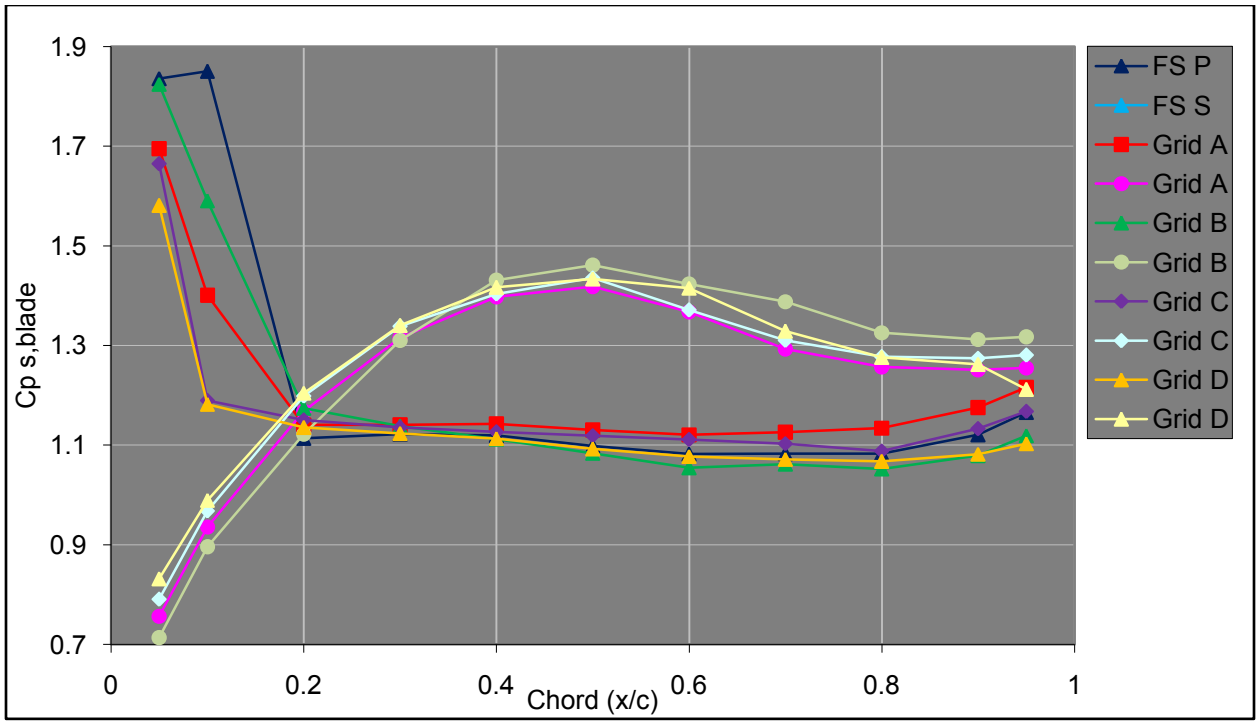

Figure B.15 Static tap graphs for $\xi = 37.5^{o}$, $\alpha^{*} = 0°$, $Re = 6 \times 10^{4}$, for all turbulence levels.

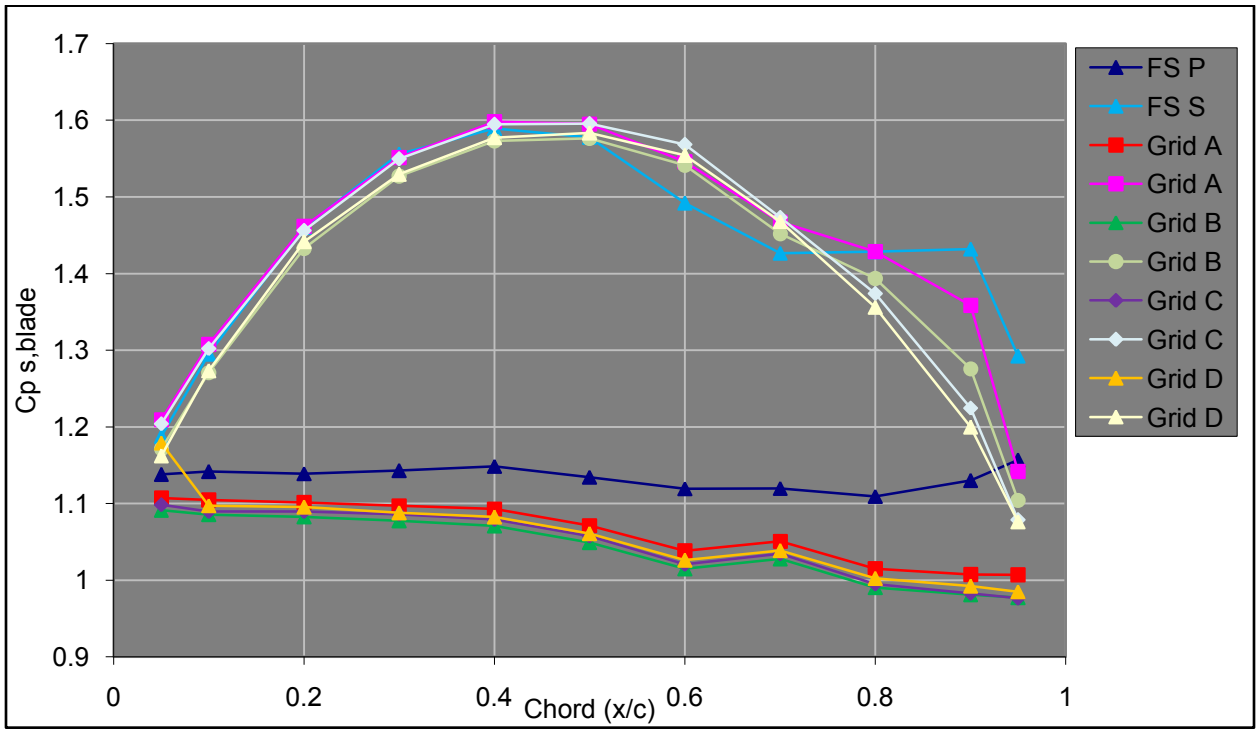

Figure B.16 Static tap graphs for $\xi = 37.5^{o}$, $\alpha^{*} = 6°$, $Re = 12.5 \times 10^{4}$, for all turbulence levels.

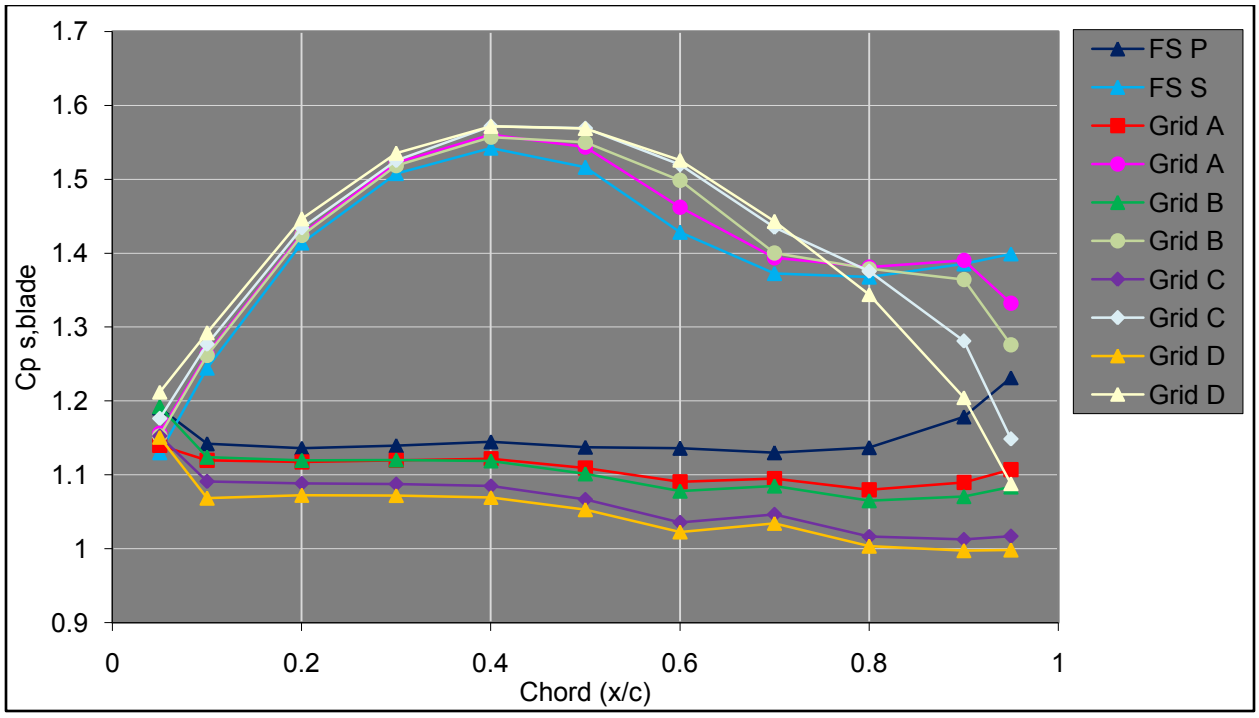

Figure B.17 Static tap graphs for $\xi = 37.5°$, $\alpha^* = 6°$, $Re = 9 \times 10^4$, for all turbulence levels.

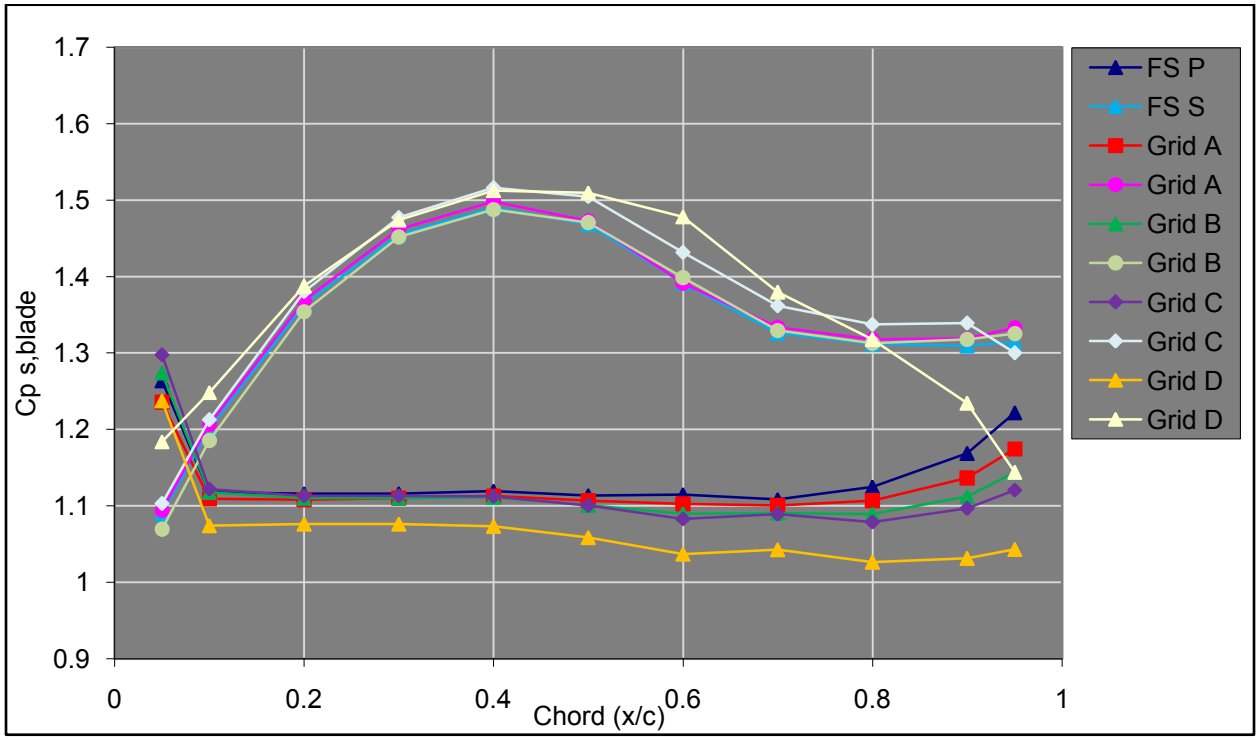

Figure B.18 Static tap graphs for $\xi = 37.5°$, $\alpha^* = 6°$, $Re = 6 \times 10^4$, for all turbulence levels.

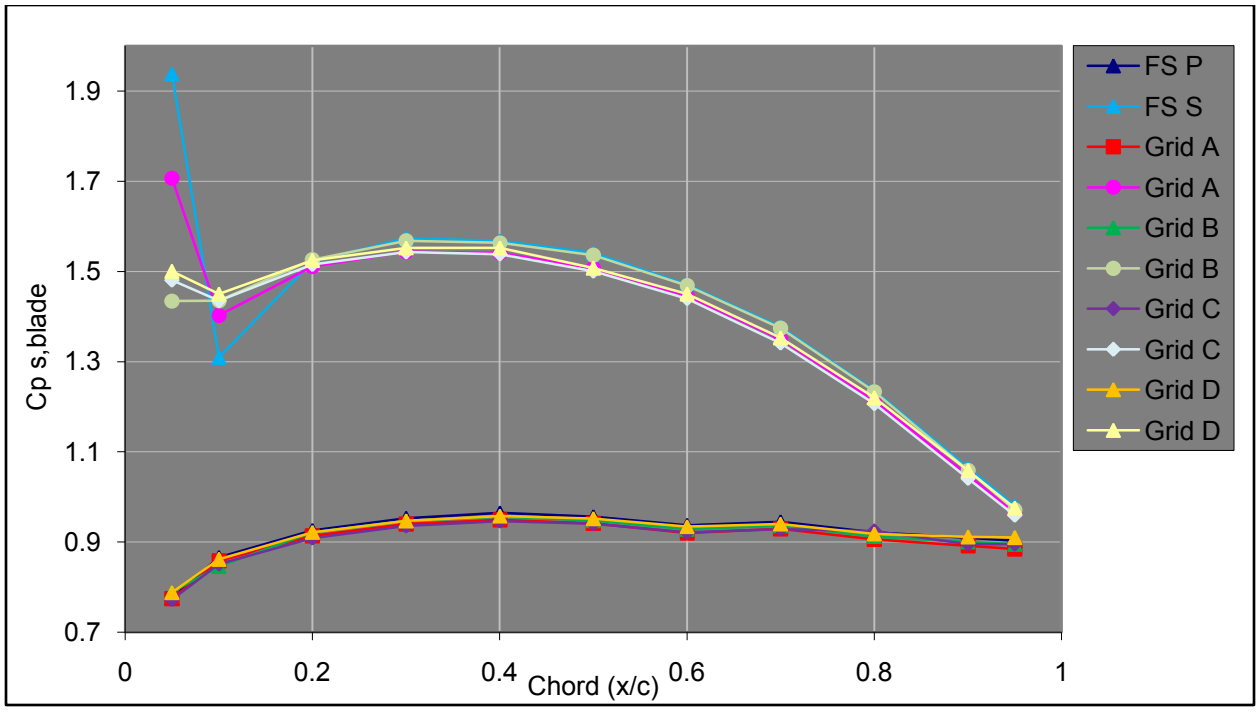

Figure B.19 Static tap graphs for $\xi = 37.5^{\circ}$, $\alpha^* = 12°$, Re = 12.5 x 10^4, for all turbulence levels.

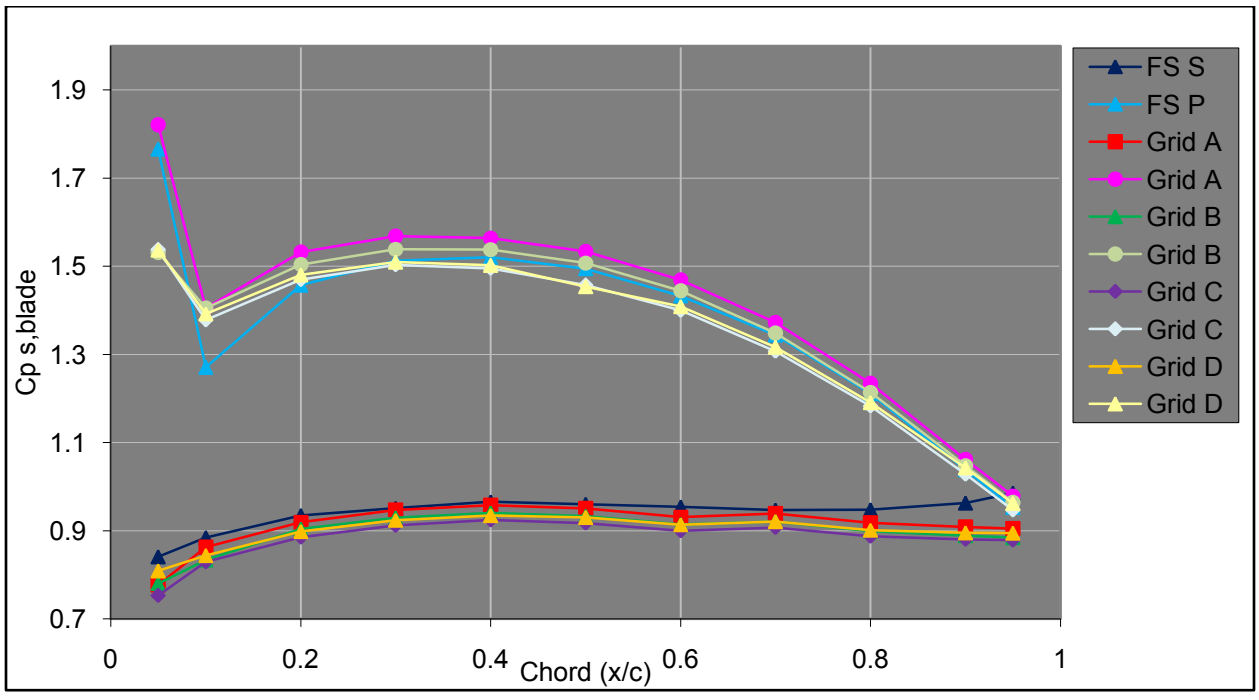

Figure B.20 Static tap graphs for $\xi = 37.5^{\circ}$, $\alpha^* = 12°$, Re = 9 x 10^4, for all turbulence levels.

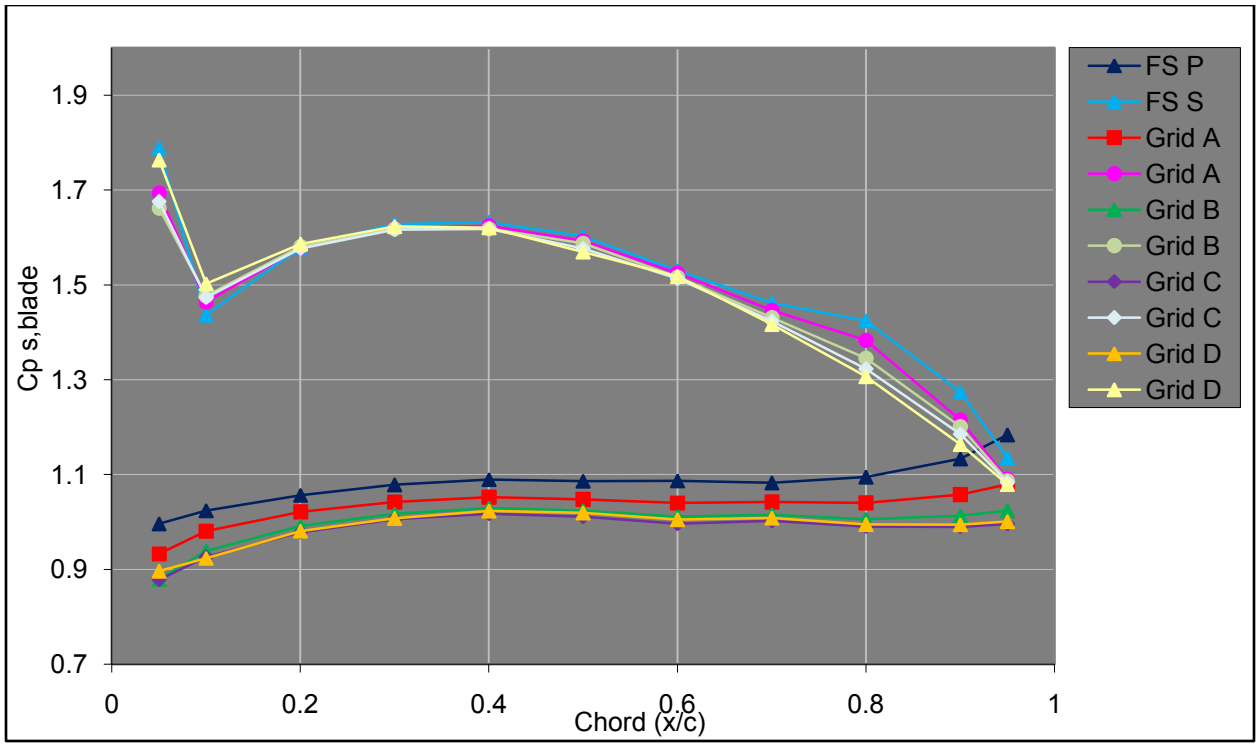

Figure B.21 Static tap graphs for $\xi = 37.5°$, $\alpha^* = 12°$, $Re = 6 \times 10^4$, for all turbulence levels.

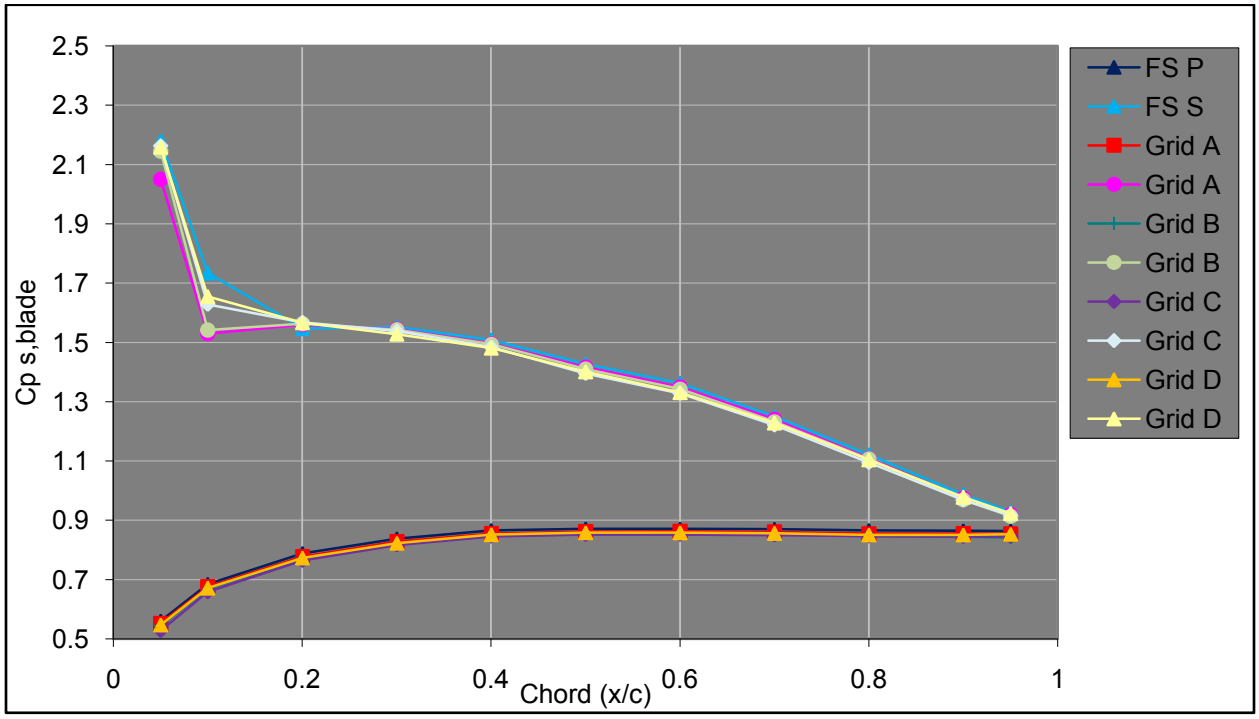

Figure B.22 Static tap graphs for $\xi = 37.5°$, $\alpha^* = 17.5°$, $Re = 12.5 \times 10^4$, for all turbulence levels.

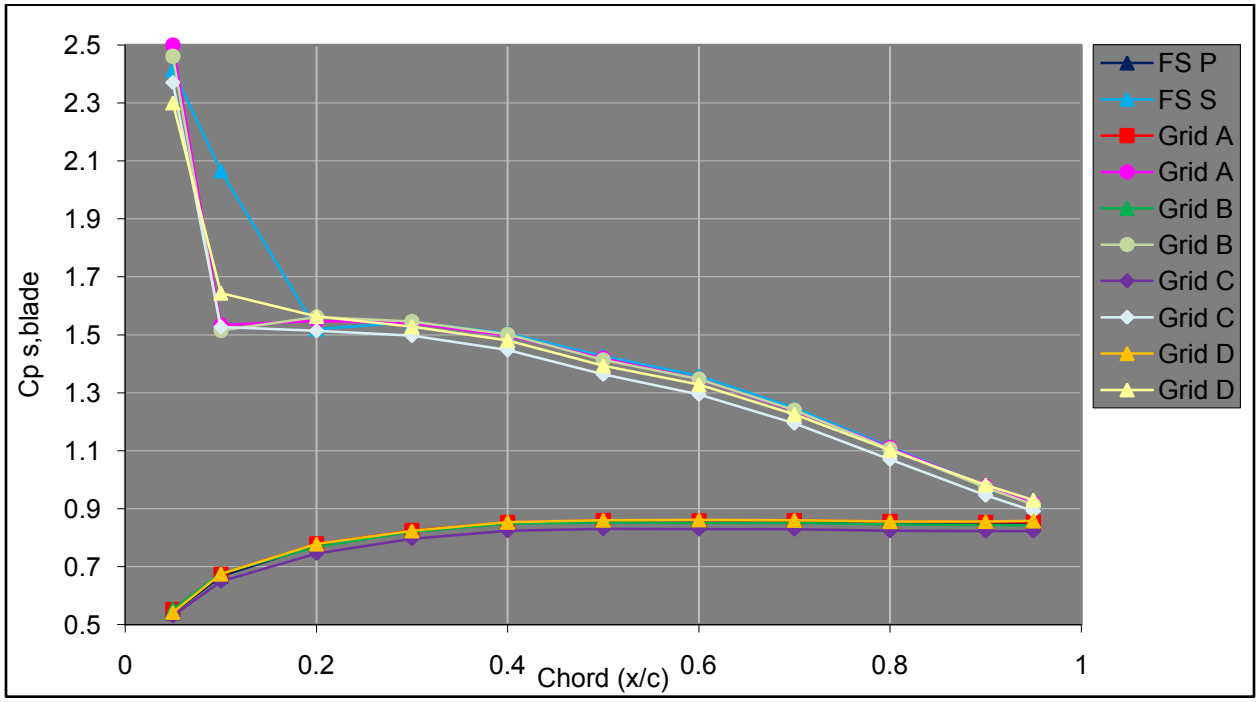

Figure B.23 Static tap graphs for $\xi = 37.5º$, $\alpha^* = 17.5°$, $Re = 9 \times 10^4$, for all turbulence levels.

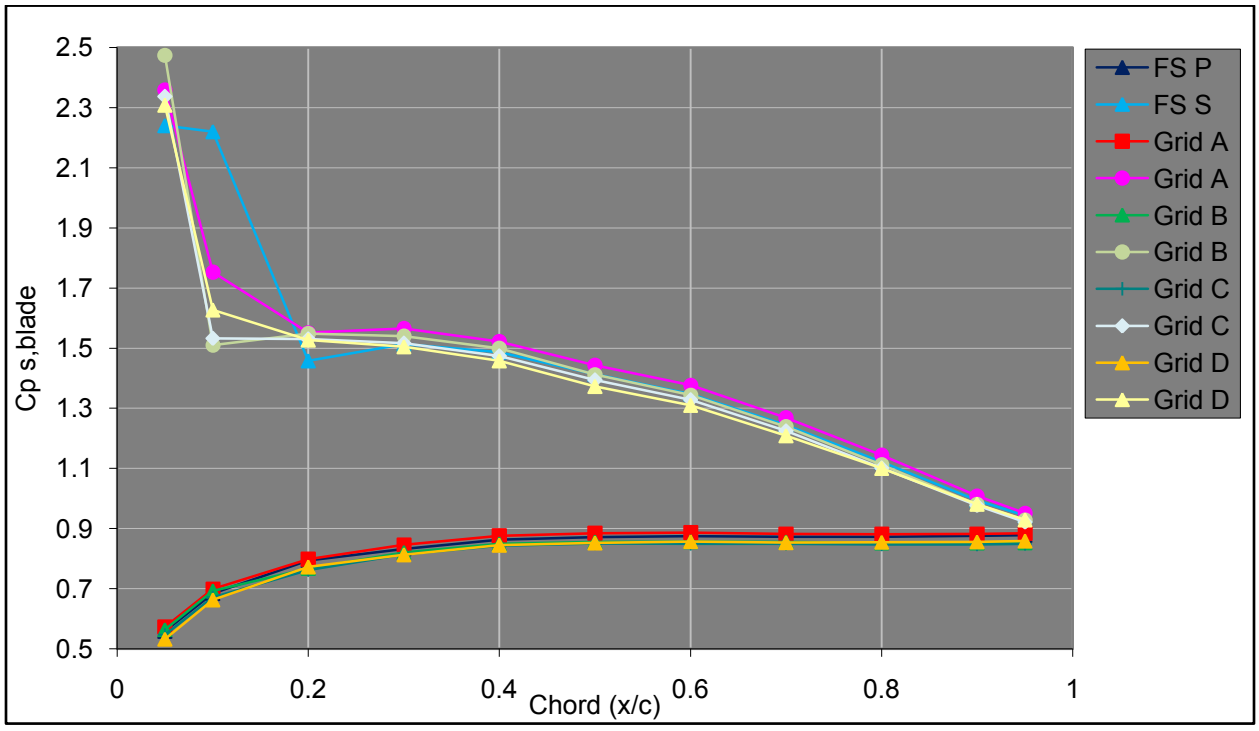

Figure B.24 Static tap graphs for $\xi = 37.5º$, $\alpha^* = 17.5°$, $Re = 6 \times 10^4$, for all turbulence levels.

Vita

Michael Perry was born and raised in Vienna, Virginia. Although accepted to Virginia Tech in 1997, he spent his initial post high school years at various schools in the West. In 2000 he was again admitted to Virginia Tech to begin a glorious seven year academic career in the Mechanical Engineering department. Although this may seem like an indirect path through academia, it provided the author enjoyable opportunities to teach students undergraduate courses and work on design projects with Dr. O'Brien.

This thesis is the proud culmination of Michael's many years of effort and diligence towards the completion of a Masters of Science in Mechanical Engineering. After its approval, he is excited to start working in the wind turbine industry for Viryd Technologies, Inc., a subsidiary of Fallbrook Technologies in Austin, Texas.

"…and I --
I took the one less traveled by,
And that has made all the difference."
-Robert Frost